Precipitation Measurements with Microwave Sensors

vorgelegt von
Andreas Leuenberger
May 2009

UNIVERSITÄT
BERN

Masterarbeit der Philosophisch-naturwissenschaftlichen Fakultät
der Universität Bern

Leiter der Arbeit:
Prof. Dr. Ch. Mätzler
Institut für Angewandte Physik

Contents

Chapter 1

Introduction

Water plays a prominent role in the atmosphere. It is important for the understanding of dynamic processes in the atmosphere, weather prediction, now-casting and climate research, just to name a few aspects of atmospheric water. Thus, there is great interest to measure atmospheric water in all its phases.

Water occurs in many different forms in the atmosphere. In its gas phase it occurs as water vapor, in the liquid phase as cloud liquid water, drizzle or rain and its solid phase water occurs as cloud ice, dry snow or hail. Furthermore there exist some mixed forms where liquid water and ice are combined e.g. wet snow or graupel. As many forms of appearance exist, as many properties have to be considered. This is a great challenge for the measurement technique.

Today, atmospheric water can be measured in many different ways: Directly in the atmosphere by balloon or aircraft soundings, from space by satellites and from the ground by rain sensors, rain radars or radiometers.

We focus on the measurement of atmospheric water as rain and wet snow by a radiometer. The radiometer is measuring the radiation at two frequencies in the microwave range. Originally, it was designed to measure water vapor and cloud liquid water. Now, it is enhanced to measure rain liquid.

Melting snow strongly interacts with microwave radiation, whereas the interaction with rain is weaker and the interaction with dry snow is negligible. To retrieve information about the region of melting snow, the so-called *melting layer*, we use an additional instrument, a vertical pointing Doppler radar. This radar is a commercial product called Micro Rain Radar (MRR). With help of the Doppler effect, the fall velocity of the precipitation can be determined.

A radiative model of the melting layer is developed. With this model the opacity of the melting layer can be calculated. To verify this model the modeled opacity is compared with measurements from the radiometer for selected special rain events when the melting layer was just above the altitude of the instruments.

It turned out that the opacity of the melting layer is proportional to the rain rate. With use of this information the algorithm estimating the rain can be improved.

Maybe the title of this work is a little bit too general, because we do not look at precipitation in general. We focus on rain and melting snow. And we consider stratiform weather situations only. This limitation is caused by a property of the MRR. At non-stratiform, convective weather situations, strong up- and downdrafts can lead to incorrect interpretations of the measured fall velocity.

To summarize, we hope that this work contributes to a better understanding of the radiative processes of rain and wet snow.

1.1 Outline of this Document

This document can be divided into three parts.

The first part is a concise summary of all necessary theories. It is divided into four chapters. The first one summarizes general aspects of radiation: Planck's law, emission, absorption, transmission, scattering, the Rayleigh and Mie approach. In the second chapter we briefly discuss the radar principles. The third chapter deals with the dielectric properties of the components of the atmosphere (water, water vapor, snow and ice). Relevant principles of clouds and precipitation are given in the fourth and last chapter of the theory part.

The second part describes the used instruments and their properties, i.e. one chapter about the radiometer TROWARA and one about the Micro Rain Radar (MRR). Some measurements are shown and the data are interpreted.

Part three is the most important one in this work. Its first chapter deals with the characteristics of stratiform rain measured by our instruments. Then we take a closer look at the melting layer spending two chapters on it. We present the measured vertical profiles and point out the characteristics of the melting layer. Then, we describe an algorithm to estimate the 0°C temperature height. At last, a model of the radiative properties of the melting layer is presented and discussed. The model is validated with use of the measurements of special rain events.

In the appendix, the engineering work of this project is described. This part must not be underestimated. A lot of time was used to set up the MRR and to automate the processes storing and visualizing the data. Thus, an overview of the setup and the data storage processes is given. A list with a short description of the most important MATLAB functions is given. A last chapter in the appendix gives additional information and statistics about the rain of the analyzed time series.

Chapter 2

Principles of Radiometry

This chapter is a concise summary of all necessary theories on electromagnetic radiation. For more details, we refer to books and scripts listed in the bibliography ([13, 6, 22, 25]).

2.1 Radiance and Radiative Flux

2.1.1 Spectral Radiance I_f

We define the radiance I_f by the radiative power dP passing through an area dA, within a solid angle $d\Omega$ and a frequency interval df in a certain direction (characterized by the angle θ representing the tilt to the normal of the area dA). Thus, radiance can be expressed in $\mathrm{W/m^2/Hz/sr}$.

$$dP = I_f \cdot df \cdot dA \cdot \cos\theta \cdot d\Omega \tag{2.1}$$

2.1.2 Radiative Flux F

The radiative flux is a measure for the power transported through an area independent of the direction. Thus, integrating the radiance over all directions ($\Omega = 4\pi$), leads to the spectral flux. The spectral flux is expressed in $\mathrm{W/m^2/Hz}$.

$$F_f = \int_{4\pi} I_f \, \cos\theta \, d\Omega \tag{2.2}$$

If the integration is limited to the forward hemisphere, we call the result F_{f+} and for the backward hemisphere F_{f-}:

$$F_{f\pm} = \pm \int_{2\pi} I_f \, \cos\theta \, d\Omega \tag{2.3}$$

The sign is such as to provide positive values, and we can write: $F_f = F_{f+} - F_{f-}$.

If we sum over all possible frequencies, we get the flux F (expressed in $\mathrm{W/m^2}$) from the spectral flux.

$$F = \int_0^\infty F_f \, df \tag{2.4}$$

2.2 Thermal Radiation

2.2.1 Planck Function

If a medium behaves like a blackbody and is in thermal equilibrium, then it emits unpolarized and isotropic spectral radiance according to its frequency f and temperature T.

The spectral radiance I_f is given by the Planck function as

$$I_f(T) = \frac{2\,h\,f^3}{c^2\,(e^{\frac{h\,f}{k_b\,T}} - 1)} \quad . \tag{2.5}$$

where T is the temperature, f the frequency, $h = 6.6256 \cdot 10^{-34}\,\mathrm{Js}$ the Planck constant, c the speed of light and $k_b = 1.3805 \cdot 10^{-23}\,\mathrm{J/K}$ the Boltzmann constant.

We can replace the frequency f by the wavelength λ using $f = c/\lambda$, $I_f\,df = -I_\lambda\,d\lambda$ and $df = -c/\lambda^2\,d\lambda$ and can write the spectral radiance I_λ as function of the wavelength λ as

$$I_\lambda(T) = \frac{2\,h\,c^2}{\lambda^5\,(e^{\frac{h\,c}{k_b\,\lambda\,T}} - 1)} \quad . \tag{2.6}$$

Figure 2.1 shows the spectral radiance I_f as a function of the frequency f for three different temperatures.

2.2.2 Rayleigh-Jeans Approximation

At low frequencies ($h\,f \ll k_b\,T$) the Planck function can be simplified to the following form. This form is called Rayleigh-Jeans approximation.

$$I_f(T) = \frac{2\,k_b\,T\,f^2}{c^2} \quad ; \quad I_\lambda(T) = \frac{2\,k_b\,c\,T}{\lambda^4} \tag{2.7}$$

This approximation is valid in the microwave range (wavelengths ranging from 1 mm to 1 m or frequencies between 0.3 GHz and 300 GHz) for usual temperatures in the atmosphere. An important property is that the radiance I_f increases linearly with temperature T.

2.2.3 Stefan-Boltzmann Law

If we integrate the spectral radiance I_f of a blackbody (2.5) over a hemisphere (using Equation (2.2)) and over all frequencies (using Equation (2.4)), we get the emitted power per area of a blackbody.

$$F = \sigma \cdot T^4 \tag{2.8}$$

where $\sigma = 5.67 \cdot 10^{-8}\,\mathrm{Wm^{-2}K^{-4}}$ is the Stefan-Boltzmann constant.

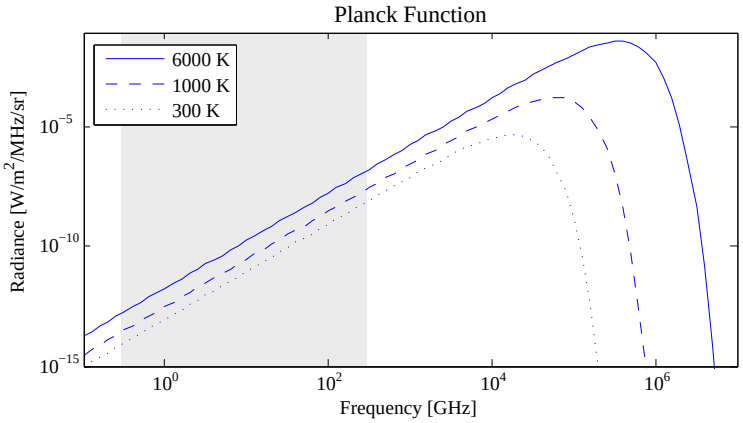

Figure 2.1: The spectral radiance of a blackbody as function of the frequency. The solid line shows the spectral radiance for a blackbody with 6000 K, the dashed with 1000 and the doted with 300 K. The region with grey background indicates the frequencies in the microwave range.

2.2.4 Brightness Temperature T_b

If we know the radiance I_f, we can calculate the temperature of a blackbody emitting this radiance. This temperature is called brightness temperature T_b. If the frequency is small, we can use the Rayleigh-Jeans approximation (2.7) and find

$$T_b = \frac{c^2\, I_f}{2\, k_b\, f^2} = \frac{\lambda^4\, I_\lambda}{2\, k_b\, c} \quad . \tag{2.9}$$

Antenna Temperature T_A

The antenna temperature T_A is equal to the brightness temperature representing the mean radiance received by the antenna.

2.3 Radiation and Interactions

Radiation propagates through a medium (e.g. air) and interacts with particles (e.g. rain drops) consisting of different dielectrical material. A collection of such interactions is shown in Figure 2.2.

If the direction of the radiation is changed by a particle, we say that the radiation is *scattered*. More about scattering is described in the next section. If the radiation is absorbed by the particle, this is called *absorption*. Absorption leads to a higher energy state of the particle. Its temperature increases.

The outgoing radiation from a particle is called *emission* and is described by the Planck's and Kirchhoff's law.

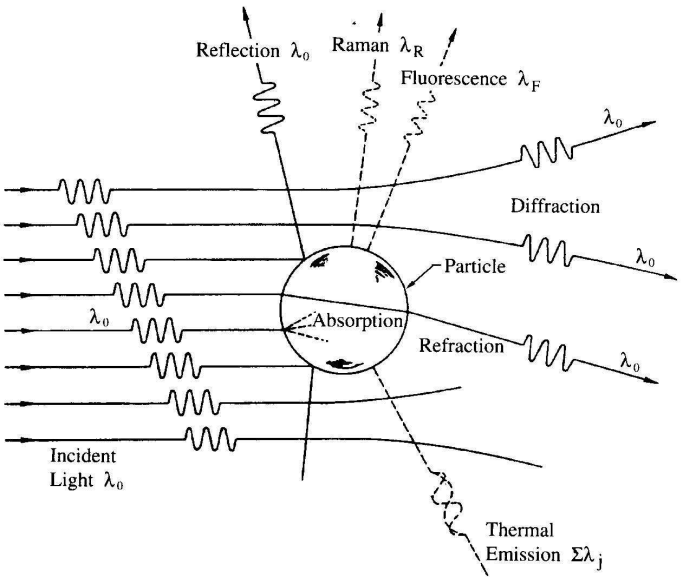

Figure 2.2: Different types of interaction between radiation and small particles (figure from [25]). For small particles, reflection, diffraction and refraction are denoted as scattering. Raman radiation and fluorescence are not discussed.

Together scattering and absorption are named *extinction* because both processes extract energy from the incident radiation. The amount of the radiation propagating through a medium, not affected by extinction is called *transmission*.

2.3.1 Kirchhoff's Law

Kirchhoff's law relates emission and absorption of radiation in Local Thermodynamic Equilibrium (LTE), meaning that emission is governed by thermal conditions as defined by a unique temperature at any given location.

If we assume that space is divided into N volumes at constant temperature T_i, $i = 1 \ldots N$, then the received power at an antenna is a linear combination of the blackbody radiance of the N volumes corresponding to the different temperatures. With use of the Rayleigh-Jeans assumption, the antenna temperature T_A can be expressed as

$$T_A = \sum_{i=1}^{N} \hat{e}_i \, T_i \tag{2.10}$$

where $\hat{e}_i$ is the scene emissivity of the volume V_i and T_i is its temperature.

Considering the reciprocal situation where the receiving antenna is replaced by a transmitter with the same antenna properties, the transmitted power must be absorbed by the N volumes. We denote $\hat{a}_i$ as the fraction of the transmitted power absorbed

in volume V_i. $\hat{a}_i$ is denoted as the scene absorptivity of the volume V_i. Due to the conservation of energy, we can write

$$\sum_{i=1}^{N} \hat{a}_i = 1 \quad . \tag{2.11}$$

Now, Kirchhoff's law states that the scene emissivity $\hat{e}_i$ of a body is equal to its scene absorptivity $\hat{a}_i$ for all frequencies, directions and polarizations.

$$\hat{e}_i = \hat{a}_i \tag{2.12}$$

And thus,

$$\sum_{i=1}^{N} \hat{e}_i = 1 \tag{2.13}$$

A special case is the situation of a so-called grey body seen from a transparent medium. In this situation the space is divided into 2 volumes ($N = 2$). T_1 is the temperature of the grey body and T_2 the temperature of the surrounding background volume. According to Equation 2.10 and 2.13, we can write

$$T_A = \hat{e}_1 \, T_1 + (1 - \hat{e}_1) \, T_2 \quad . \tag{2.14}$$

In this situation $\hat{e}_1$ is the *emissivity* of the grey body.

2.3.2 Cross Sections σ_i

The concept of cross sections describes the effective area of a particle to absorb, to scatter or to extinct radiation. The product of the incoming radiative flux F_0 with the cross section σ_i gives the scattered, absorbed or extincted power.

$$P_i = \sigma_i \, F_0 \quad ; \quad [W] = [m^2] \cdot [W/m^2] \tag{2.15}$$

where F_0 is the incoming flux, σ_i the cross section, P_i is the absorbed, scattered or extincted power and i stands either for absorption (abs), scattering (scat) or extinction (ext).

As already defined above, extinction is the effect of absorption and scattering together.

$$\sigma_{ext} = \sigma_{scat} + \sigma_{abs} \tag{2.16}$$

Differential Cross Section σ_d

The amount of the scattered radiation depends on the angle ϑ between incoming and outgoing radiation, and if the particle is not symmetric, the scattered radiation depends

on the orientation angle ϕ to the particle. Thus, we define the differential cross section σ_d as the ratio between scattered power per solid angle to the incoming flux F_0.

$$\sigma_d(\vartheta, \phi) = \frac{F(\vartheta, \phi)}{F_0} \quad ; \quad \left[\frac{m^2}{sr}\right] = \frac{[W/sr]}{[W/m^2]} \tag{2.17}$$

The relation between the differential cross section and the scattering cross section is given as

$$\sigma_{scat} = \int_0^{2\pi} \int_0^{\pi} \sigma_d(\vartheta, \phi) \, \sin\vartheta \, d\vartheta \, d\phi \quad . \tag{2.18}$$

Backscattering Cross Section σ_b

The backscattering cross section is defined as $4\,\pi$ times the differential cross section in opposite direction of the incoming flux.

$$\sigma_b = 4\pi \, \sigma_{180} \tag{2.19}$$

2.3.3 Efficiencies Q_i

The efficiencies of absorption Q_{abs}, scattering Q_{scat}, backscattering Q_b or extinction Q_{ext} are defined as the corresponding cross sections normalized to the geometrical cross section of the particle.

$$Q_i = \frac{\sigma_i}{\sigma_g} \tag{2.20}$$

where σ_g is the geometrical cross section of the particle. For spheres, $\sigma_g = \pi D^2/4$, where D is the diameter of the particle.

2.4 Scattering

2.4.1 Scattering Regimes

Scattering depends strongly on the ratio between the wavelength λ of the radiation and the size of the particles, expressed by the particle diameter D_p. As a measure for this ratio we use x as size parameter, where $x = \pi D_p/\lambda$. We distinguish between different types of scattering. If the particle is very small compared to the wavelength ($D_p \ll \lambda$) the scattering is negligible. If the particles are still small compared to the wavelength ($x < 1$), we are in the Rayleigh scattering regime and if $x \geq 1$ we have to use the Mie theory. The Mie theory considers spheres only. If the wavelength is small compared to the particle size ($x \gg 1$), the scattering approaches the laws of geometric optics.

Figure 2.3 gives an overview of the scattering regimes. We use microwaves with wavelength in order of about 1 cm and the particles of interest are snowflakes, rain drops and drizzle. As we see in Figure 2.3, the dimensions of the particles exceed the limits of Rayleigh scattering, and we have to consider Mie scattering.

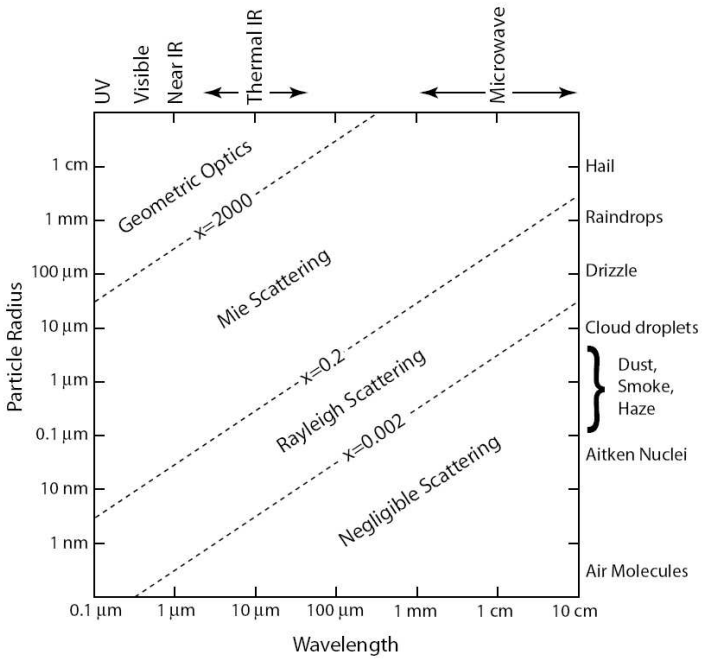

Figure 2.3: Scattering regimes as relation of wavelength (x-axis) and sphere radius (y-axis). x denotes the sphere size normalized to the wavelength $x = \pi D_p/\lambda$, where D_p is the sphere diameter (figure from [6]).

2.4.2 Rayleigh Scattering

If the sphere is small compared to the wavelength (size parameter $x < 1$), the scattering can be analyzed with the Rayleigh theory. If we assume that the dielectric constant of the ambient medium is one, we find for the scattering efficiency

$$Q_{scat} = \frac{8}{3} x^4 \left| \frac{\varepsilon - 1}{\varepsilon + 2} \right|^2 \qquad \sim \frac{1}{\lambda^4} \quad . \tag{2.21}$$

ε is the dielectric constant of the material of the sphere. We assume that the particle consists of a non-magnetic material ($\mu \approx 1$) and that the surrounding material is air ($\varepsilon_{air} \approx 1$, $\mu_{air} \approx 1$).

The absorption efficiency is given by

$$Q_{abs} = 12\, x \frac{\varepsilon''}{|\varepsilon + 2|^2} \qquad \sim \frac{1}{\lambda} \tag{2.22}$$

and the backscattering efficiency by

$$Q_b = 4\, x^4 \left| \frac{\varepsilon - 1}{\varepsilon + 2} \right|^2 \qquad \sim \frac{1}{\lambda^4} \quad . \tag{2.23}$$

We see that the intensity of the scattered radiation is proportional to λ^{-4}. Thus, shortwave radiation is scattered much more than long-wave radiation. The effect of the wavelength is not that strong for the absorption efficiency. It is just proportional to λ^{-1}.

Polarization: Unpolarized incoming radiation is scattered depending on the angle ϑ between incoming and scattered radiation. In forward and backward direction, the scattered radiation is not polarized. But the polarization is maximal for directions perpendicular to the incoming radiation. The scattered intensity is proportional to $1 + \cos^2 \vartheta$. Figure 2.4 visualizes this context.

2.4.3 Mie Theory

The interaction between radiation and spheres, in the same order as the wavelength, is calculated using the Mie theory. The Mie theory applies the boundary conditions of the electric and magnetic field to the surface of a homogeneous sphere (see [9, 10, 13]).

The Mie efficiencies for scattering, extinction, absorption and backscattering are given as

Mie Efficiencies

$$Q_{scat} = \frac{2}{x^2} \sum_{n=1}^{\infty} (2n+1) \left(|a_n|^2 + |b_n|^2 \right) \tag{2.24}$$

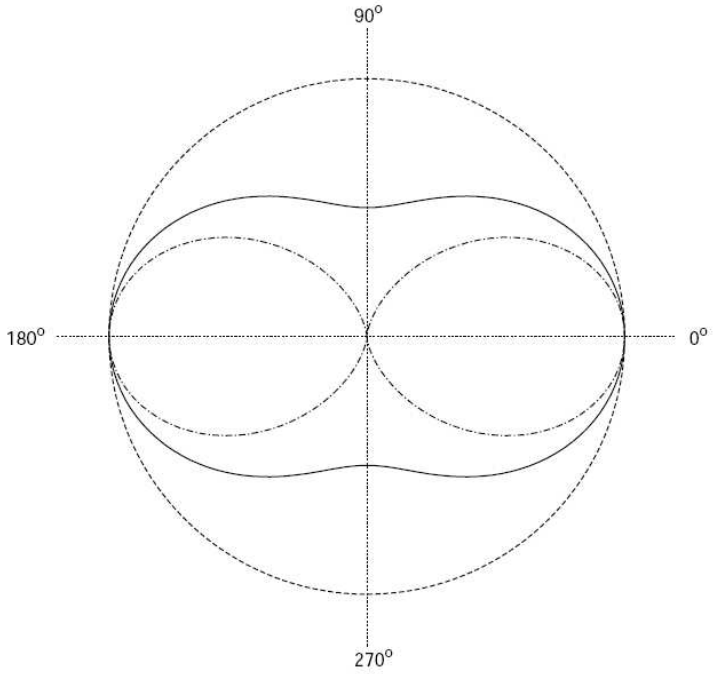

Figure 2.4: The solid line shows the intensity of unpolarized radiation as function of the angle to the incoming direction. The other lines show the intensity if the incoming radiation is polarized (figure from [6]).

$$Q_{ext} = \frac{2}{x^2} \sum_{n=1}^{\infty} (2n+1)\, Re[a_n + b_n] \tag{2.25}$$

$$Q_{abs} = Q_{ext} - Q_{scat} \tag{2.26}$$

$$Q_b = \frac{1}{x^2} \left| \sum_{n=1}^{\infty} (2n+1)\,(-1)^n\,(a_n - b_n) \right|^2 \tag{2.27}$$

where a_n, b_n, c_n and d_n are the Mie coefficients and x is the size parameter.

The Mie coefficients a_n, b_n compute the amplitude of the scattered field, c_n, d_n the amplitude of the internal field. These coefficients are calculated using spheric Bessel and Hankel functions. For details see [13, 9, 10].

Figure 2.5 shows the Mie efficiencies of spheres of water as function of the radius. We see that the backscattering efficiency is most sensitive to the particle radius.

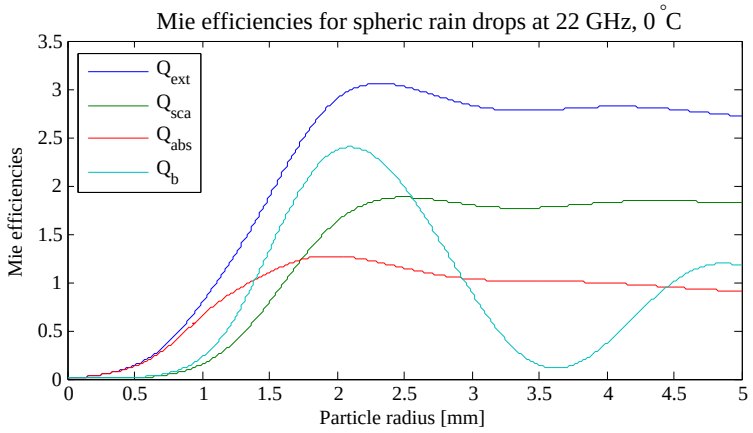

Figure 2.5: Mie efficiencies for spherical water droplets at 22 GHz and at a temperature of 0°C.

2.5 Radiative Transfer

2.5.1 Opacity and the Law of Beer-Lambert

We consider the radiance I_λ propagating through a medium without emission and scattering. The medium absorbs radiation. Thus, after a propagating path with length ds, the radiance decreased by the amount dI_λ. If the path length ds is small, we can assume that the loss of radiance is proportional to the radiance and we can write

$$dI_\lambda = -\gamma_{abs}\, I_\lambda\, ds \tag{2.28}$$

where γ_{abs} is the absorption coefficient.

To calculate the radiance as a function of the path, we can solve Equation (2.28) for $I_\lambda(s)$ and get

$$I_\lambda(s) = I_{\lambda,s_0}\, e^{-\int_{s_0}^{s} \gamma_{abs}(s')\, ds'} \quad . \tag{2.29}$$

I_{λ,s_0} is the radiance at the reference location s_0.

With the definition of the opacity (or optical depth) τ

$$\tau(s) = \int_{s_0}^{s} \gamma_{abs}(s')\, ds' \quad , \tag{2.30}$$

we can rewrite Equation (2.29) and get the law of Beer-Lambert.

$$I_\lambda(s) = I_{\lambda,s_0}\, e^{-\tau(s)} \tag{2.31}$$

The term $T = e^{-\tau(s)}$ lies in a range between 0 and 1 and represents the amount of radiance transmitting through the medium (from s_0 to s). This term T is called *transmittance* or *transmissivity*.

2.5.2 Propagation Coefficients (γ_{ext}, γ_{abs}, γ_{scat}, γ_b)

The proportionality factor γ_{abs} already mentioned in Equation (2.28) is a called propagation coefficient, or for the absorption, absorption coefficient. In the same manner, propagation coefficients for scattering, backscattering and extinction can be defined.

The value of the propagation coefficient depends on the medium. If we consider air containing small particles, the propagation coefficients depend on the material and the sizes of the particles. The influence of the air is neglected. In the previous section, we defined the cross section and efficiency of a particle. If the size distribution $N(D)$ of the particles as a function of the particle diameter is known, we can calculate the propagation coefficients as

$$\gamma_j = \int_0^\infty \sigma_j(D)\, N(D)\, dD = \frac{\pi}{4} \int_0^\infty D^2\, Q_j(D)\, N(D)\, dD \tag{2.32}$$

where the index j represents either extinction (ext), absorption (abs), scattering ($scat$) or backscattering (b). $\sigma_j(D)$ and $Q_j(D)$ are the cross section and efficiency, respectively and $N(D)$ is the size distribution. The propagation coefficients have the unit [1/length].

Knowing the dielectric properties of the medium, we can also express the absorption coefficient as

$$\gamma_{abs} = 2\, k'' = 2\, n''\, k_0 = 2\, n''\, \frac{\omega}{c_0} = \frac{4\pi\, n''}{\lambda} \tag{2.33}$$

where k'' is the imaginary part of the wave number, n'' the imaginary part of the refractive index, k_0 the wave number in vacuum, c_0 the speed of light in vacuum, ω the angular frequency and λ the wavelength.

2.5.3 Propagation Through an Emitting Medium

In the previous section, we considered the absorption/extinction of the radiation by the medium. What if the medium itself is emitting radiation?

In the following we use the Rayleigh-Jeans approximation (Equation (2.7)) and replace the radiance by the brightness temperature.

Figure 2.6 shows the situation of incident radiation through an emitting medium. At level s_1, the brightness temperature is $T_b(s_1)$. The temperature of the medium is a function of s or τ, respectively. Note, that the opacity is zero at s_0 and is increasing towards s_1.

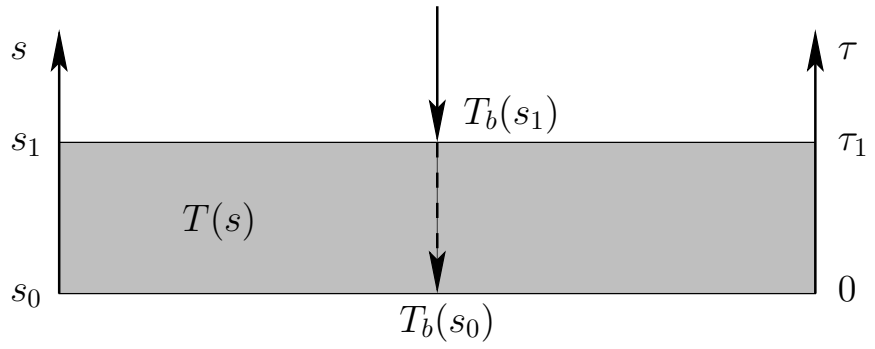

Figure 2.6: Radiation propagating through a layer of an emitting medium. At level s_1 the brightness temperature is $T_b(s_1)$.

Equation (2.34) shows how the measured brightness temperature at the surface $T_b(s_0)$ can be calculated knowing the brightness temperature above the emitting layer $T_b(s_1)$ and the opacity $\tau(s)$ on every height.

$$T_b(s_0) = T_b(s_1)\, e^{-\tau(s_1)} + \int_0^{\tau(s_1)} T(\tau)\, e^{-\tau}\, d\tau \tag{2.34}$$

Integrating over the path length s instead over the opacity τ ($d\tau$ is replaced by $\gamma_{abs}(s)\, ds$) leads to

$$T_b(s_0) = T_b(s_1)\, e^{-\tau(s_1)} + \int_{s_0}^{s_1} T(s')\, e^{-\tau(s')}\, \gamma_{abs}(s')\, ds' \quad . \tag{2.35}$$

If the temperature $T(s)$ of the emitting layer is constant, the expression for $T_b(s_0)$ simplifies to

$$T_b(s_0) = T_b(s_1)\, e^{-\tau_1} + T_m\, (1 - e^{-\tau_1}) \tag{2.36}$$

where T_m is the constant temperature of the layer and τ_1 is the opacity at s_1.

Effective mean temperature: Usually the temperature of the layer is not constant. But we can define the effective mean temperature according to the following equation

$$T_m = \frac{\int_0^{\tau_1} T(\tau)\, e^{-\tau}\, d\tau}{1 - e^{-\tau_1}} \tag{2.37}$$

and this expression can be used as constant temperature as in Equation (2.36).

If we assume that the temperature decreases/increases linearly with increasing opacity τ, we set for the temperature $T(\tau) = T_c + T_d\,\tau$ and the previous calculation for the effective mean temperature gives

$$T_m = T_c + T_d \left[1 - \frac{\tau_1\, e^{-\tau_1}}{1 - e^{-\tau_1}}\right] \quad . \tag{2.38}$$

Setting T_m into Equation (2.36) leads to

$$T_b(s_0) = T_b(s_1)\, e^{-\tau_1} + (T_c + T_d)\,(1 - e^{-\tau_1}) - T_d\,\tau_1\, e^{-\tau_1} \quad . \tag{2.39}$$

In an optically thin layer $\tau_1 \ll 1$, T_m can be approximated by $T_m \approx T_c + 0.5\, T_d\, \tau_1$. And in an optical thick layer $\tau_1 \gg 1$, T_m can be approximated by $T_m \approx T(\tau = 1) = T_c + T_d$.

Chapter 3

Radar

Measuring electromagnetic radiation emitted and scattered from objects is called radiometry. A passive method. Now, we shortly introduce radar, an active method, where the instrument itself transmits radiation and receives the backscattered radiation. Additionally to the information about the backscattering objects, we get information on their positions.

Most of the content described in this chapter is taken from [24] and [11]. The radar instrument used in this work is described later. Here we describe only the basic radar principle.

3.1 The Radar Principle

Radar was invented at the end of the 19^{th} century and is an abbreviation for RAdio Detection And Ranging. The principle can be divided into three main processes. First, the transmitting of the radiation by the radar antenna. Second, the backscattering by the objects or particles and third, the receiving of the signal by the antenna. The information about the scatterer is extracted from the time delay (or frequency shift) of the received signal to the transmitted signal. The intensity of the received signal gives information about the size and number of the backscattering objects.

There exist many different types of radar operation. We distinguish between *pulsed* and *continuous wave* radar. The pulsed radar transmits a burst of radiation and waits for the backscattered signal. After a time delay it transmits the next burst. Then a radar system can be *coherent* or *non-coherent*. In the first case, there exists a phase relation between the transmitted and the received signal. Here, we just consider *mono-static* radar, where the transmitter and the receiver are located at the same place, in contrast to the *bi- or multi-static* radar. Usually radar systems work in a frequency range from 10 MHz up to 100 GHz.

Figure 3.1 shows a schematic picture of the radar principle. On the left side the transmitter and receiver are shown, and on the right side a scattering particle is drawn.

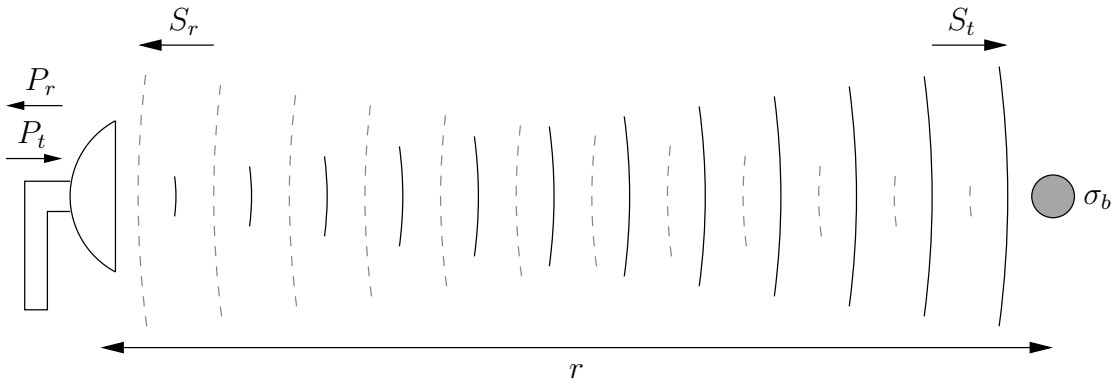

Figure 3.1: Radar principle. On the left side the transmitting and receiving antenna is shown and on the right side the backscattering object is drawn, characterized by the backscattering cross section σ_b.

3.2 Range Resolution

The distance between two scattering objects can only be resolved within a range. This limitation originates from the bandwidth B of the system. The range resolution Δr depends on the bandwidth B, and the speed of the radiation c. Δr is given by

$$\Delta r \geq \frac{c}{2\,B} \quad . \tag{3.1}$$

3.3 The Radar Equation

To derive the radar equation we consider the situation drawn in Figure 3.1. First we derive the radar equation for a single backscatterer and then for a volume filled with backscattering objects.

3.3.1 Single Scatterer

The radar antenna transmits radiation with the power P_t. At a distance r of the antenna, the intensity S_t is given as

$$S_t = g\,\frac{P_t}{4\pi\,r^2} \tag{3.2}$$

where g is the antenna gain. The antenna gain describes the directional characteristic, and it is defined as the ratio of the actual intensity from the antenna and from an isotropic antenna. Thus, g is a function of the angle, but we consider only the transmission and reception by the antenna beam, and we assume that g is constant within the beam.

The scattering object is characterized by the backscattering cross section σ_b. The scattered power is the product of the incoming intensity S_t and the cross section σ_b. At the receiver the intensity S_r of the scattered object is given as

$$S_r = \frac{\sigma_b \, S_t}{4\pi \, r^2} \quad . \tag{3.3}$$

From antenna theory we know that the ratio of received power to the intensity S_r depends on the wavelength λ, and the antenna gain is given as

$$g = 4\pi \, \frac{P_r}{\lambda^2 \, S_r} \quad . \tag{3.4}$$

Summarizing the previous three equations and solving for the received power P_r, we get the radar equation for a single scatterer.

$$P_r = \frac{1}{(4\pi)^3} \, g^2 \, \lambda^2 P_t \, \frac{\sigma_b}{r^4} \tag{3.5}$$

3.3.2 Many Scatterers

As we are interested in the backscattered radiation of rain drops, we must consider the backscattering within a volume, the scattering volume. Figure 3.2 shows a sketch of the scattering volume at distance r from the radar antenna. The range resolution is Δr and the solid angle of the radar beam is Ω_0.

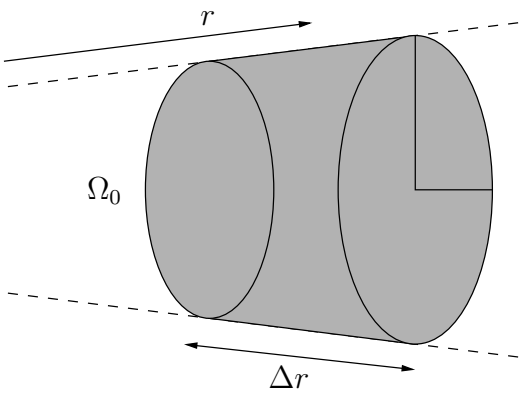

Figure 3.2: Scattering volume

The scattering volume ΔV is calculated as

$$\Delta V = \Delta r \, \Omega_0 \, r^2 \quad . \tag{3.6}$$

If the distances between the scatterers are large enough, the cross section of a scattering volume is equal to the sum of the cross sections of all objects within the

scattering volume. This total cross section divided by volume ΔV is described as volume backscatter coefficient η and can be calculated from

$$\eta = \frac{\sum_i \sigma_{b,i}}{\Delta V} \tag{3.7}$$

where i is an index for every scattering object.

With the total backscattering cross section $\sum_i \sigma_{b,i} = \eta\, \Delta V$, described by the volume backscatter coefficient η, the radar equation for a cloud of many backscatterer leads to

$$P_r = \frac{1}{(4\pi)^3}\, g^2\, \lambda^2 P_t\, \frac{\eta}{r^2}\, \Delta r\, \Omega_0 \tag{3.8}$$

If we measure the received power by the antenna and know the antenna characteristics, we can solve the equation for the volume backscatter coefficient η.

3.3.3 The Radar Reflectivity Factor

The classical radar reflectivity is based on Rayleigh theory.

The backscattering cross section according to Rayleigh theory is given using Equation (2.23) by

$$\sigma_{b,Rayleigh}(D) = \frac{\pi^5}{\lambda^4} \left|\frac{\varepsilon - 1}{\varepsilon + 2}\right|^2 D^6 = \frac{\pi^5}{\lambda^4}\, |K|^2\, D^6 \tag{3.9}$$

where $K = |(\varepsilon - 1)/(\varepsilon + 2)|$, λ is the wavelength, ε the dielectric constant of the scattering object at wavelength λ and D is the diameter of the object.

Using the Rayleigh formula for the Rayleigh backscattering cross section, we can formulate the volume backscatter coefficient according to Equation (3.7) as

$$\eta_{Rayleigh} = \frac{\pi^5}{\lambda^4}\, |K|^2\, \frac{\sum_i D_i^6}{\Delta V} = \frac{\pi^5}{\lambda^4}\, |K|^2\, Z \quad . \tag{3.10}$$

where Z is called the radar reflectivity factor.

The radar reflectivity factor Z is defined as

$$Z = \int_0^\infty N(D)\, D^6\, dD \tag{3.11}$$

and is expressed in $\mathrm{mm}^6/\mathrm{m}^3$. The advantage of this measure is, that it does not depend on the wavelength of the radar frequency. Thus, measurements of different radars with different frequencies can be compared.

Often a logarithmic scale makes more sense, and thus the reflectivity factor is expressed as

$$dBZ = 10\, \log_{10} \frac{Z}{Z_{ref}} \tag{3.12}$$

where $Z_{ref} = 1\, \mathrm{mm}^6/\mathrm{m}^3$.

3.3.4 The Equivalent Radar Reflectivity

When the observed scattering volume does not satisfy the conditions of the Rayleigh approximation, it is convenient to characterize the radar reflectivity factor Z by the equivalent radar reflectivity Z_e. Z_e is equal to the reflectivity factor of a population of liquid and spherical particles satisfying the Rayleigh approximation and producing a signal of the same power. Thus,

$$Z_e = \frac{\lambda^4}{\pi^5 |K_w|^2} \eta \tag{3.13}$$

where K_w is the dielectric factor of water.

In the following text, when we write reflectivity or radar reflectivity, we mean the equivalent radar reflectivity Z_e.

3.4 Doppler Frequency Shift

If an electromagnetic signal is reflected at a moving object, the frequency of the reflected signal is shifted. An object moving towards the antenna increases the frequency, moving away from the antenna decreases the frequency. This effect is called Doppler effect and is used to determine the speed of the scattering objects.

The frequency shift is given as

$$\Delta f_D = \frac{2}{\lambda} v \tag{3.14}$$

where Δf_D is the frequency shift by the Doppler effect, λ is the wavelength and v is the speed of the object in direction towards/away from the radar antenna.

Chapter 4

Dielectric Properties

We have seen that the properties to emit, to absorb, to transmit and to scatter depend on the size of the particles, and the influence of the particle size was discussed in Chapter 2 (Rayleigh and Mie theory).

The influence of the matter itself is also very important. Thus, we are discussing the dielectric properties of the material. As we are interested in rain and snow, we summarize the dielectric properties of the dry atmosphere, of water vapor, of liquid water, of cloud water, of ice, of rain, of dry and wet snow.

Most of the information in this chapter is taken from [13], [26] and [12].

4.1 The Dielectric Constant

If an electric field $\mathbf{E}$ acts on a medium, the medium is polarized and influences the displacement field $\mathbf{D}$. The strength of the polarization depends on the material. The influence of the material can be expressed by the dielectic constant ε' (in vacuum $\varepsilon' = 1$).

$$\mathbf{D} = \varepsilon_0 \, \mathbf{E} + \mathbf{P} = \varepsilon' \, \varepsilon_0 \, \mathbf{E} \tag{4.1}$$

$\mathbf{D}$ is the displacement field, $\mathbf{E}$ the electric field, $\mathbf{P}$ the polarization, ε_0 the vacuum permittivity and ε' the relative dielectric constant.

The complex relative dielectric constant ε is defined as

$$\varepsilon = \varepsilon' + i \, \varepsilon'' \quad , \tag{4.2}$$

where ε' is the relative dielectric constant from Equation (4.1). The imaginary part ε'' origins from Ohm's law and is defined as

$$\mathbf{j} = \sigma \mathbf{E} = \varepsilon'' \, \varepsilon_0 \, \omega \, \mathbf{E} \tag{4.3}$$

where $\mathbf{j}$ is the current density, σ the conductivity and ω the angular frequency.

As the behavior of the material depends on the frequency, ε is a function of frequency.

The complex refractive index n is given as

$$n = n' + i\,n'' = \sqrt{\varepsilon\,\mu} \approx \sqrt{\varepsilon} \tag{4.4}$$

where μ is the relative magnetic permeability. In the following, we consider non-magnetic materials only ($\mu = 1$) and use the approximation on the right side of Equation (4.4).

The imaginary part n'' of the refractive index n is a measure of the loss in the material. Thus, the following relation between the n'' and the absorption coefficient γ_{abs} is valid (as already expressed in Equation (2.33)).

$$\gamma_{abs} = \frac{4\pi\,n''}{\lambda} \tag{4.5}$$

λ is the wavelength.

4.1.1 Dielectric Mixing Formula

If we have a heterogeneous medium with structures much smaller than the wavelength, we can use the Maxwell-Garnett formula to calculate the effective dielectric constant ε of the heterogeneous medium. We consider a host medium with the relative dielectric constant ε_e with inserted particles with ε_i. Then the Maxwell-Garnett formula is given as

$$\varepsilon = \frac{(1 - f_v)\,\varepsilon_e + f_v\,\varepsilon_i\,K}{1 - f_v + f_v\,K} \tag{4.6}$$

where f_v is the volume fraction and K is a parameter depending on the shape of the particles. But K depends also on the orientation of the particles and generally we have to consider K as diagonal tensor, where K_i is the element for the i-th principal axis.

If we assume that the inserted particles are ellipsoids and that they are oriented isotropically, we can use the average K factor defined as

$$K = \frac{1}{3}\sum_{k=1}^{3} K_i \;\; ; \quad with \quad K_i = \frac{\varepsilon_e}{\varepsilon_e + A_i\,(\varepsilon_i - \varepsilon_e)} \quad . \tag{4.7}$$

The K_i represent the shape factor in the principal axes and A_i is called depolarization factor of the ellipsoid along the i-axis. Note, that $A_1 + A_2 + A_3 = 1$. If the ellipsoid is flat like a disk, it is called oblate and $A_1 = A_2 < 1/3$, $A_3 > 1/3$. If it looks like a needle, it is called prolate and $A_1 = A_2 > 1/3$, $A_3 < 1/3$.

For hydrometeors, the Maxwell-Garnett formula (4.6) can be simplified using K from Equation (4.7) and assuming that the volume fraction f_v is very small. This leads to

$$\varepsilon = \varepsilon_e + \frac{f_v(\varepsilon_i - \varepsilon_e)}{3}\sum_{k=1}^{3} \frac{\varepsilon_e}{\varepsilon_e + A_k\,(\varepsilon_i - \varepsilon_e)} \quad . \tag{4.8}$$

4.2 Polarization

Polarization is the displacement of charges in atoms and molecules due to the influence of the electromagnetic field. It depends on the frequency and on the atomic and molecular structure. Certain frequencies stimulate electrons, atoms or molecules to move and sometimes a state of resonance is reached. We distinguish between four different mechanisms of polarization as shown in Figure 4.1.

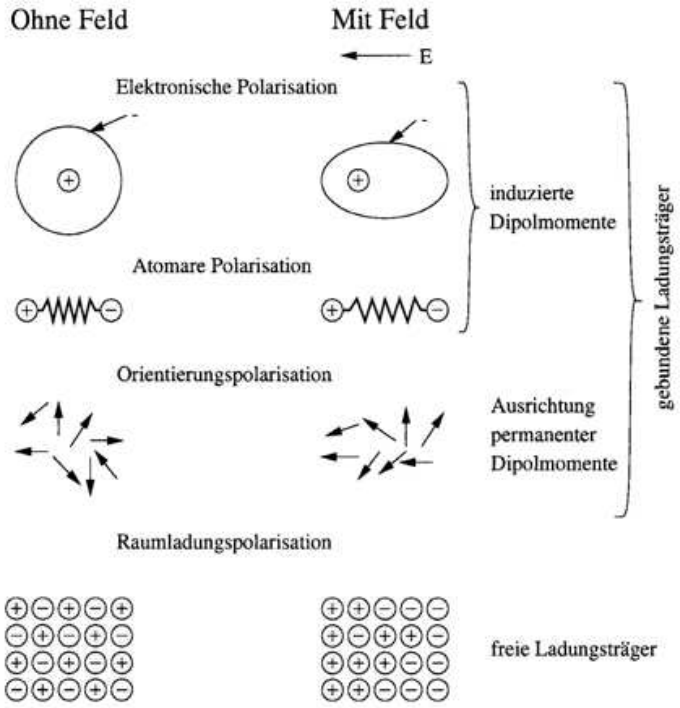

Figure 4.1: Mechanisms of polarization. This figure gives a schematic overview over four types of polarization. From top to bottom are shown the electronic, atomic, orientation and space charge polarization. On the left side, the situation is shown without electric field and on the right side with electric field, respectively (figure from [13]).

Each of these mechanisms is triggered in a certain frequency range. Figure 4.2 gives an overview in which frequency range each polarization phenomenon occurs.

4.2.1 Electronic Polarization

The electronic field displaces the electron cloud of the atoms causing small dipoles. This phenomenon occurs at frequency ranges from static up to UV radiation.

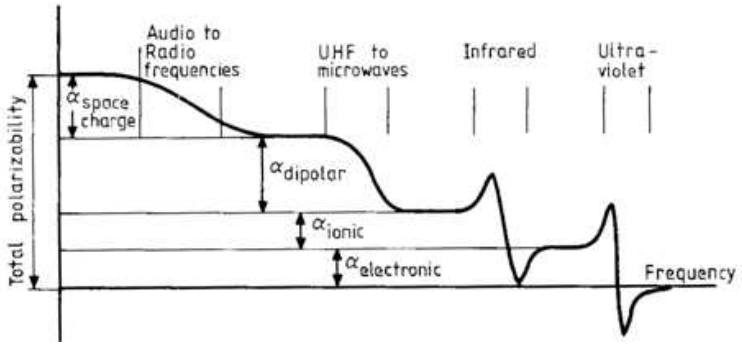

Figure 4.2: Frequency ranges, where the polarization phenomena occur. From the lowest to the highest frequency are shown the space charge, orientation, atomic and electronic polarization. The polarization effect is accumulated at low frequencies (figure from [13]).

4.2.2 Atomic Polarization

The molecules are deformed by the electronic field. Due to the deformation the molecules are vibrating or rotating. The effect of vibrations occurs at wavelengths from about 1 to 100 μm. The effect of rotations occurs at longer wavelengths, from mm to cm wavelength range.

4.2.3 Orientation Polarization

In liquids, vibrations and rotations are hindered. Thus, there are no sharp resonances. In polar liquids like water, the polarization is due to orientational forces on the dipoles. Thermal motion and friction forces counteract the electric field. This relaxation phenomenon is called after Debye. It occurs from the microwave to the radio-frequency range.

4.2.4 Space Charge Polarization

Freely moving charges influence the polarization. The displacement of charges results in dipoles. Geometric limits and the dynamic behavior determine the effect.

4.3 Dry Atmosphere

The Earth's atmosphere contains 78.08% nitrogen, 20.95% oxygen, 0.93% argon, 0.038% carbon dioxide, traces of hydrogen, helium and other noble gases (measured by molar content/volume). Additionally, a variable amount water vapor is available. We say that the atmosphere is dry, if the amount of water vapor is zero or can be neglected. As we are interest in the lower levels of the troposphere only, we assume that the atmosphere is well mixed in this region.

The polarisable molecules of the atmosphere absorb (and emit) radiation due to energy state transitions. The radiation leads to rotation or vibrations of the molecules depending on the frequency. Thus, the gas molecules are "atomic polarized". The wavelength where the radiation is absorbed depends on the structure of the molecule. Each gas shows characteristic absorption lines. They are broadened due to natural (uncertainty principle), thermal and pressure broadening.

Figure 4.3 shows the absorption coefficient of the dry atmosphere as function of the frequency. The enhanced absorption at about 60 GHz origins from a band of absorption lines of the oxygen molecule.

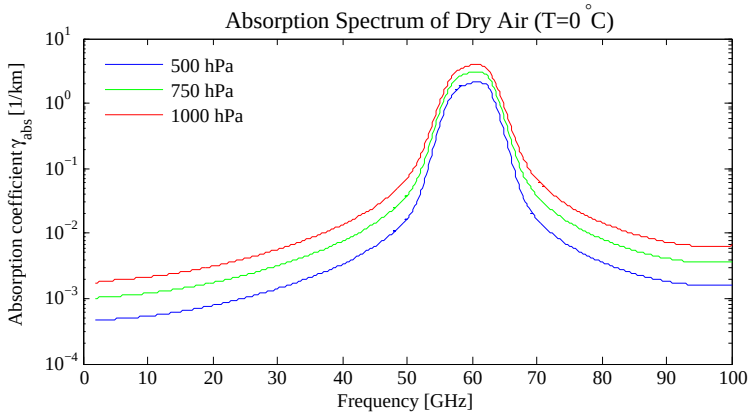

Figure 4.3: Absorption coefficient of dry air for 500 (blue), 750 (green) and 1000 hPa (red) as function of the frequency. Figure plotted with use of the Microwave Propagation Model from Hans Liebe (MATLAB module *mpm93*, see [13]).

As we are mainly interested in water vapor and water, we are interested in wavelengths where the absorption of the dry atmosphere is small. We find such frequencies below 40 GHz and above 80 GHz.

4.4 Water Vapor

Figure 4.4 shows the absorption spectrum of water vapor for different pressure levels. We clearly see the absorption line at 22.235 GHz. The absorption line is broadened at high pressure. At the right edge of the graph, the absorption coefficients already increase due to the next significant absorption line of water vapor at 183 GHz.

The absorption of the dry atmosphere is small in the frequency range of this absorption line. It can be estimated by a statistical approach using the surface temperature, pressure and relative humidity.

As we are interested in water vapor as integrated quantity, we reduce the influence of the pressure broadening by measuring not directly at the absorption frequency but slightly next to it (in the frequency region where the different, pressure dependent lines

of the absorption coefficients cross).

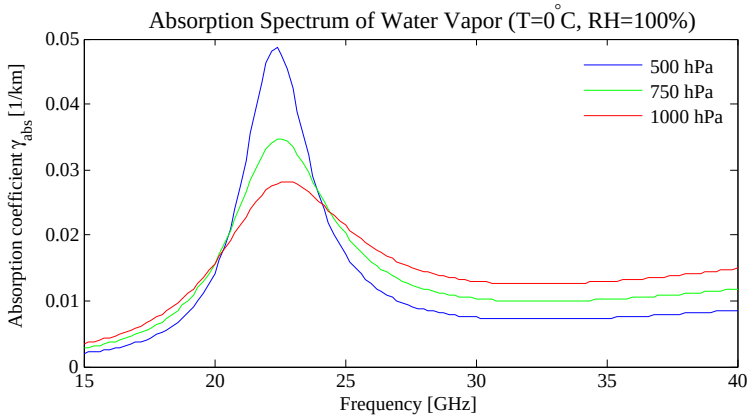

Figure 4.4: Absorption coefficient of water vapor for 500 (blue), 750 (green) and 1000 hPa (red) as function of the frequency.

4.5 Liquid Water

The dipolar water molecules cannot freely rotate or vibrate in liquid water as they do as gas molecules. But they underlie an orientational polarization. This effect is called Debye relaxation.

Figure 4.5 shows the characteristics of the complex relative dielectric constant ε for two different temperatures. We see that the real part of ε is constant at low and high frequencies and decreases in the range of the Debye relaxation frequency (about 10 GHz). At this frequency the imaginary part of ε is maximal.

The relaxation frequency is shifted towards higher frequencies at higher temperatures . Figure 4.6 shows the temperature dependency of the complex relative dielectric constant ε. If the temperature is about 20°C the relaxation frequency occurs at about 21 GHz. But as we are interested in atmospheric processes, the temperature is mostly below 20°C or even below 0°C and the relaxation frequency is below 20 GHz.

4.6 Ice

The molecules in ice are fixed at their location and are strongly hindered to rotate or to vibrate. But nevertheless, a relaxation phenomenon is observed at low frequencies (at about 10 KHz). This relaxation is not important for our purpose and we can conclude that the relative dielectric constant of ice is very small and therefore the absorption coefficient is small. In most of the cases, we can neglect the impact of ice on our measurements. Ice is almost transparent. Figure 4.7 shows the ε for ice as a function of the frequency. The real part is constant and the imaginary part is very small.

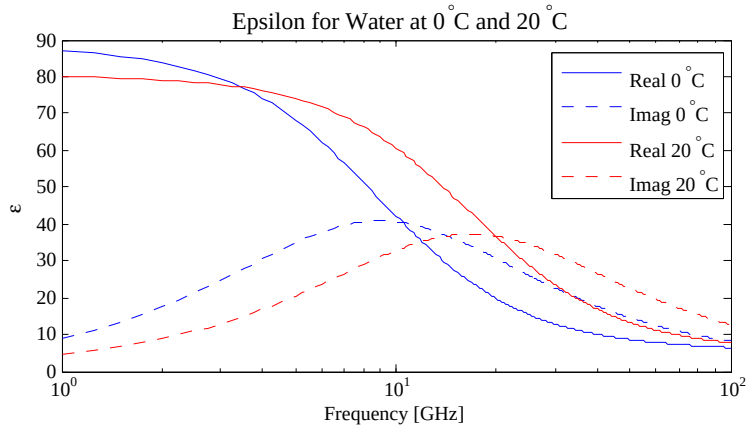

Figure 4.5: Complex relative dielectric constant ε for water as function of frequency at two different temperatures. The blue curve shows ε for 0°C and the red curve for 20°C, respectively. The real part of ε is printed solid, the imaginary part is dashed. (Graph is based on the model from Ellison (2006) (see [12]), use *epsalwater0* MATLAB script.)

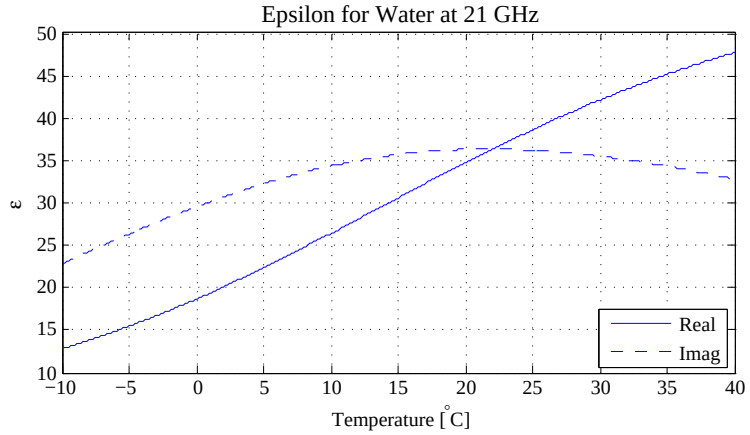

Figure 4.6: The complex relative dielectric constant ε of water as function of temperature. The real part is drawn solid, the imaginary part dashed.

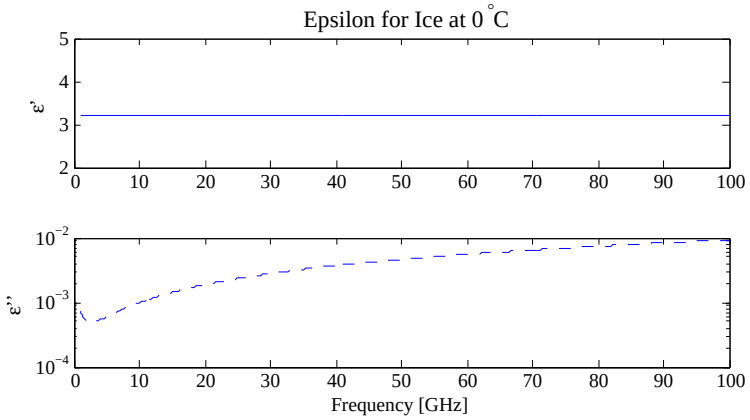

Figure 4.7: Complex relative dielectric constant ε for solid ice as function of frequency. The solid line shows the real part of ε and the dashed the imaginary part, respectively. Graph plotted using *epsice* using model from Mätzler (2006).

4.7 Cloud Water

Small cloud droplets can be modeled as small spheres of liquid water surrounded by air. Using the simplified Maxwell-Garnett formula (4.8) we set the dielectric constant of the environmental air to unity ($\varepsilon_e = 1$) and we use the dielectric constant of liquid water ε_w as the dielectric constant of the insertions ε_i. The volume fraction is small and usually in the order of 10^{-6}. Thus, the complex relative dielectric constant of a cloud or of fog is calculated as

$$\varepsilon = 1 + 3\, f_v \, \frac{\varepsilon_w - 1}{\varepsilon_w + 2} \quad . \tag{4.9}$$

The real part is close to unity ($\varepsilon' \approx 1$) and the imaginary part is given by

$$\varepsilon'' = \frac{9\, f_v \, \varepsilon''_w}{|\varepsilon_w + 2|^2} \quad . \tag{4.10}$$

Figure 4.8 shows the absorption coefficient of a cloud with different amounts of liquid water content. The absorption is increasing with frequency. A cloud underlies a relaxation process as well. But compared to liquid water the relaxation frequency is shifted towards higher frequencies and is observed at about 120 GHz.

4.8 Rain

A different approach to determine the absorption of a rain layer was already presented in Chapter 2. It is based on the cross sections of the rain drops determined by Mie theory (see Equation (2.32)). This approach is described in detail in [8]. It assumes

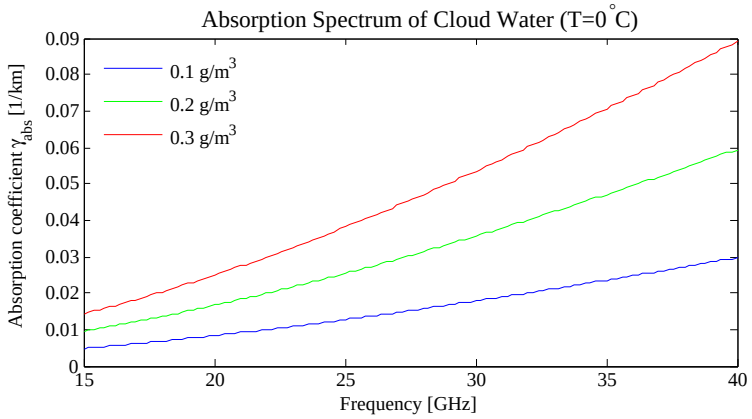

Figure 4.8: Absorption coefficient of a cloud with liquid water. The amount of liquid water is 0.1 (blue), 0.2 (green) and 0.3 (red curve) g/m^3.

that the rain drops are spheres and that the drop size distribution is known. Using this method, we get the propagation coefficients.

It can be shown that the absorption coefficient of a rain layer is proportional to the rain rate (see [14]).

$$g_R = \frac{\gamma_{R,abs}}{R} \tag{4.11}$$

where g_R is the proportionality factor depending on the frequency. R is the rain rate and $\gamma_{R,abs}$ is the absorption coefficient of the rain layer.

Figure 4.9 shows the extinction coefficient of rain at three different rain rates. The characteristics are similar to the absorption coefficient of cloud liquid water. Note, that this figure is based on the following empirically formula of Olsen.

$$\gamma_{ext} = \alpha\, R^{\beta} \tag{4.12}$$

R is the rain rate given in mm/h, α and β are empirical coefficients depending on the frequency.

4.9 Dry Snow

As already mentioned, the dielectric properties of ice are close to the dielectric properties of air and so are the properties of dry snow. In this section, we look at the dielectric constant of a snow pack at the ground and not at a layer of falling snow.

Here we present the result of an empirical fit of dry snow found by Mätzler (see [12]).

$$\varepsilon' = \begin{cases} 1 + 1.4667\, f_v + 1.435\, f_v^3 & 0 \le f_v < 0.45 \\ ((1 - f_v) + 1.4759\, f_v)^3 & f_v \ge 0.45 \end{cases} \tag{4.13}$$

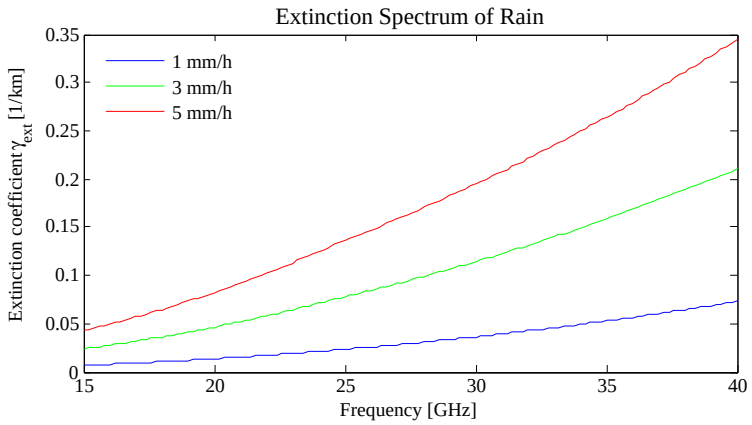

Figure 4.9: Extinction coefficient of rain at 1 (blue), 3 (green) and 5 (red) mm/h.

where f_v is the volume fraction of ice. The volume fraction is equal to the density of the snow pack divided by the density of ice ($f_v = \rho/\rho_{ice}$).

The imaginary part of dry snow can be computed from the mixing formula and an approximation is given as

$$\varepsilon'' = (0.48\, f_v + 0.52\, f_v^2)\, \varepsilon_i'' \tag{4.14}$$

where f_v is the volume fraction of ice and ε_i'' the imaginary part of the dielectric constant of ice.

Figure 4.10 shows the real and imaginary parts of the dielectric constant of dry snow at 21 GHz and 0°C as function of the density of the snow pack. The real part increases from the ε' of air to the ε' of ice with increasing density. The imaginary part is generally small and decreases towards zero at small densities.

4.10 Wet Snow

If we look at a pack of wet snow, we have a mixture of air, ice and liquid water. If the amount of the liquid water is small, we can assume that we have an environment of dry snow with water inclusions. Additionally, we assume that the liquid water inclusions are ellipsoid. Thus, if the amount of liquid water is small, we can use the simplified Maxwell-Garnett formula (equation (4.8)) where the environmental medium is dry snow (ε_d) and the inclusions are water (ε_w).

$$\varepsilon = \varepsilon_d + \frac{w_v\,(\varepsilon_w - \varepsilon_d)}{3} \sum_{k=1}^{3} \frac{\varepsilon_d}{\varepsilon_d + A_k\,(\varepsilon_w - \varepsilon_d)} \quad ; \quad w_v \leq 0.05 \tag{4.15}$$

where ε_d is the complex dielectric constant for dry snow, ε_w the dielectric constant of water, w_v is the volumetric liquid water content and the A_k's are the form factors of the included water ellipsoids in the ice.

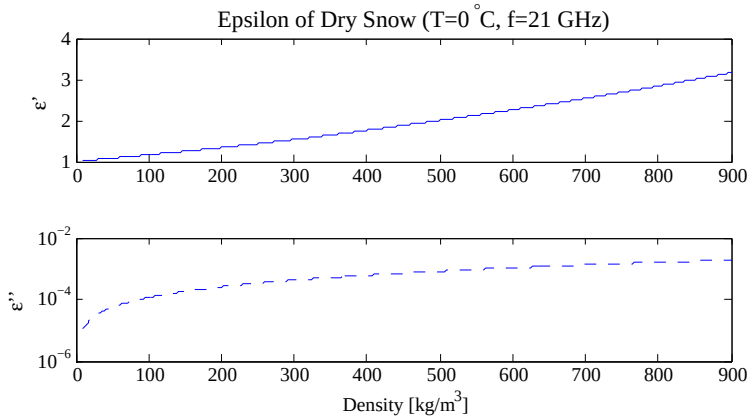

Figure 4.10: Complex relative dielectric constant ε for compact dry snow as function of density. The upper plot shows the real part of ε and the lower plot the imaginary part, respectively.

Mätzler shows in [12] and [1] that we get best results if we assume that the water inclusions are prolate ellipsoids with an axial ratio of about 1:25. Thus, we set for the depolarization factors: $A_1 = A_2 = 0.4975$, $A_3 = 0.005$.

If the volumetric liquid water content exceeds 0.05, the linear approximation is no longer valid. There exists a formula for ε' by Denoth:

$$\varepsilon' = 1 + 1.92\,\rho + 0.44\,\rho^2 + 18.7\,w_v + 45\,w_v^2 \quad ; \quad w_v > 0.05 \tag{4.16}$$

where w_v is the volumetric liquid water fraction and ρ is the density of the snow expressed in g/cm^3.

Figure 4.11 shows the real and imaginary parts of the dielectric constant of wet snow as a function of the liquid water content. Wet snow absorbs strongly in the microwave range as can be seen by the large imaginary part ε''.

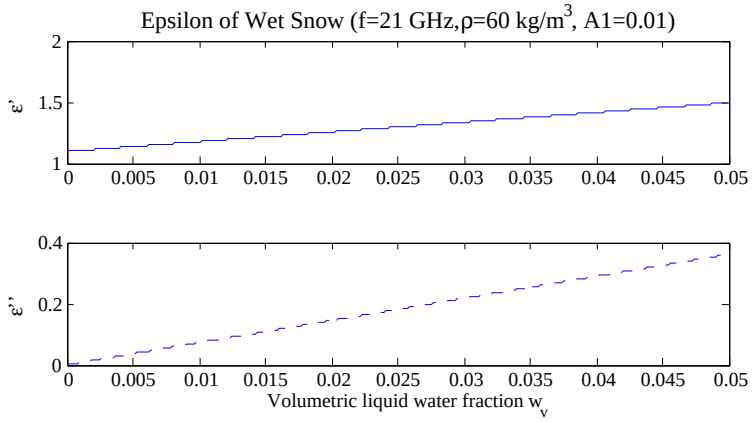

Figure 4.11: Complex dielectric constant at 21 GHz of wet snow as function of the volumetric liquid water content. The upper graph shows the real the lower graph the imaginary part, respectively.

Chapter 5

Physics of Precipitation

The physics of clouds and precipitation is a very widespread topic and we summarize here just some selected properties relevant to our study. For more general information about this topic read [23], detailed information about the microphysics is given in [20] and some aspects about stratiform precipitation and about the melting layer are taken from [21] and [2].

5.1 Stratiform Precipitation

Clouds and precipitation develop due to cooling of moist air. When the cooling air gets saturated small water and cloud droplets form. When the amount of liquid water within a cloud reaches a certain level, it starts to rain. The cooling of the air is mostly caused by lifting of the air masses. We distinguish between convective and stratiform precipitation.

The process causing convective precipitation uses the latent heat of the condensing water vapor to enforce the upward vertical motion. The vertical motion intensifies the condensing process leading to even more latent heat release. This positive feedback loop can cause heavy thunderstorms. Convective precipitation can occur within small regions with updrafts on the order of m/s (on the order of tens of m/s for thunderstorms).

If the upward motion is caused by the large-scale weather situation (e.g. by a baroclinic cylone), air masses are lifted in a large region. This process is much slower than convective rain, and a clear horizontal structure is observed (hence the name stratiform). The precipitation is more continuous, falling from nimbostratus clouds. The vertical motion is in the order of a few tens of centimeters per second.

Figure 5.1 shows a schematic picture of a stratiform precipitation situation. At the top of the cloud the water vapor condenses to cloud droplets (This is even possible if the temperature is below zero degrees leading to supercooled cloud drops.) or deposits on tiny ice crystals. The condensation and deposition processes are very slow and can explain the formation of very small droplets and crystals only.

If we have a cloud with tiny droplets consisting of supercooled water and some

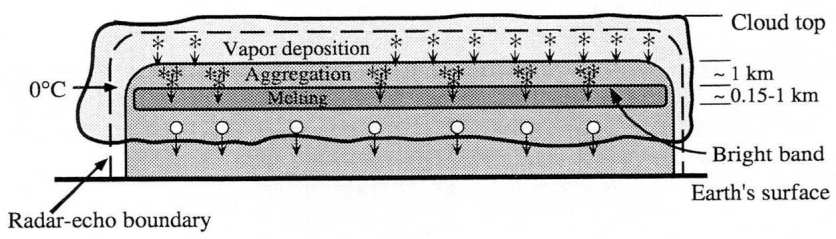

Figure 5.1: Characteristics of stratiform precipitation (Figure from [2])

consisting of ice, then the saturation water vapor pressure over the ice is smaller than over the supercooled liquid droplets. Thus, the water droplets evaporate water vapor, that is deposited at the surface of the ice crystals. The ice crystals can grow very fast while the water droplets diminish and finally disappear. This process is called Bergeron-Findeisen process and thought to be the most efficient process building precipitation.

Other processes responsible for the growing of rain droplets and ice crystals are aggregation and riming. If ice particles collect other ice particles, the process is called aggregation. If ice particles collect liquid drops, which freeze up on contact, the process is called riming. Aggregation depends on temperature. It starts when the temperature is above -16°C and intensifies at temperatures at about -5°C. At this temperature large snowflakes can develop.

5.2 The Melting Layer

When falling snowflakes reach the 0°C isotherm they start to melt. The layer below the 0°C temperature height down to the height where the falling particles have the shape of rain drops is called *melting layer*. The melting layer has a vertical extent between 400 and 600 m, depending on the rain rate, the lapserate and the humidity.

In the upper part of the melting layer aggregation is still dominant, however breakup of the wet flakes occurs in the lower part. The aggregation in the upper and the breakup in the lower part are of the same efficiency and neutralizing each other. Looking at the top and the bottom of the melting layer, it seems that one snowflake yields one rain drop as observed by Barthazy ([2]).

An important characteristic of the melting layer is the increasing fall velocity due to the changing shape of the falling particles. It is obvious that a snowflake falls more slowly than a rain drop with the same mass.

Unfortunately there is little known about how the amount of liquid water evolves within the melting layer.

Considering the melting layer with a rain radar, we see an enhanced radar reflectivity. Due to this enhanced reflectivity, the level of the melting snow appears very bright on radar screens. Therefore the layer is also called bright band. A melting snowflake is

covered by a thin film of melt water, leading to a large surface of liquid water scattering the incident radiation. Thus, a melting snowflake has the same backscattering cross section as a large rain drop. Dry snowflakes are less visible for the rain radar due to the small reflectance of ice.

Houze ([21]) points out that the enhanced reflectivity cannot be explained by the increasing amount of liquid water alone. He states that the aggregation process gets more efficient in the upper layer of the bright band and thus the radar reflectivity increases due to the larger particles.

Pruppacher and Klett ([20]) explain that the melt water does not form a coating around the flakes, but flows from the flake periphery to the linkage of the snowflake branches where it accumulates, leaving the ice skeleton of the flake uncovered with water. But the melt water must form first, before it can accumulate at the branches.

It is shown that the size distribution of snowflakes is exponential and similar to the drop size distribution of rain drops (see [2]), independent whether the diameter of the resulting melted drop or the real diameter was observed.

5.3 Classification

Precipitation occurs in various forms. As liquid it can be classified according to the drop diameter. Then we say it is drizzle or rain. If the precipitation is frozen, we speak of graupel, hail or snow.

Table 5.1 gives an overview over some precipitation types according to their radar reflectivity. Note, that some frozen precipitation types, like snow or graupel, are not within this list.

Table 5.1: Typical radar reflectivities for precipitation (from [21]).

Type of Precipitation	**Radar Reflectivity**
Drizzle	0 to 10 dBZ
Rain	10 to 30 dBZ
Heavy rain	30 to 60 dBZ
Hail	60 to 70 dBZ

If we classify the types of the hydrometeors not only by the reflectivity of a rain radar but also by the fall velocity, we can distinguish between several regimes of hydrometeors (see Figure 5.2). We see that some regimes are overlapping and within these regimes no clear classification is possible.

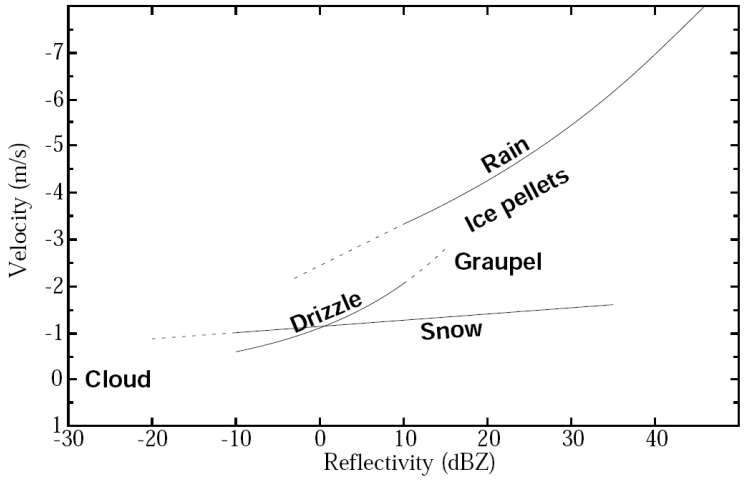

Figure 5.2: Regimes of reflectivity and fall velocity associated to different types of hydrometeors (Figure from Fabry [5]).

5.4 Drop Size Distribution

An interesting characteristic of rain is the drop size distribution. There exists an empirical formula (see [7]) given as

$$N(D,R) = N_0\, D^a\, e^{-\Lambda D} \tag{5.1}$$

where D is the diameter of the rain drops, N_0, a and Λ are empirically determined coefficients whereby N_0 and Λ depend on the rain rate R.

Table 5.2 summarizes the coefficients according to the drop size distribution of Marshall-Palmer (ML), Laws- Parson (LP), Joss-Dizzle (JD) and Joss-Thunderstorm (JT). The rain rate has to be inserted in mm/h. The distribution $N(D,R)$ is expressed as number of drops per mm^3 and per mm diameter.

Table 5.2: Parameters for drop size distribution according to Laws-Parsons (LP), Marshall and Palmer (MP), Joss-Dizzle (JD) and Joss-Thunderstorm (JT).

Distribution Function	$\mathbf{N_0(R)}$ $\mathbf{[\#/mm^4]}$	$\mathbf{\Lambda(R)}$ **[1/mm]**	**a**
LP	$1.98 \cdot 10^{-5} R^{-0.384}$	$5.38 \cdot R^{-0.186}$	2.93
MP	$0.80 \cdot 10^{-5}$	$4.1 \cdot R^{-0.21}$	0
JD	$3.00 \cdot 10^{-5}$	$5.7 \cdot R^{-0.21}$	0
JT	$0.14 \cdot 10^{-5}$	$3.0 \cdot R^{-0.21}$	0

Figure 5.3 shows the characteristic of the Marshall-Palmer drop size distribution for 1, 5 and 10 mm/h rain (see [7]).

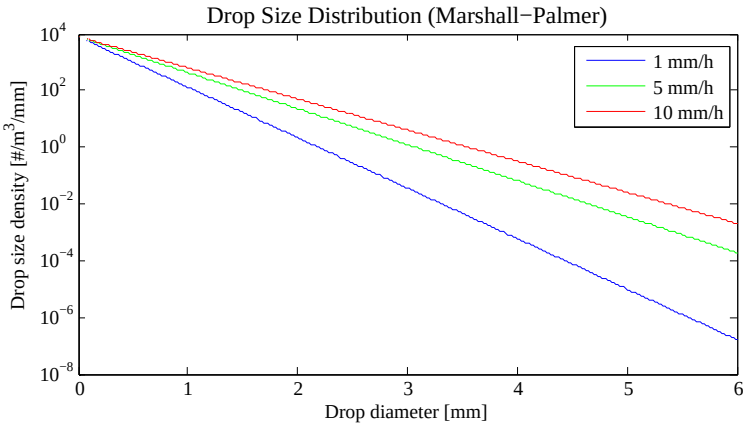

Figure 5.3: Drop size distribution according to Marshall and Palmer for the rain rate of 1 mm/h (blue), 5 mm/h (green) and 10 mm/h (red).

5.5 Terminal Fall Velocity

The fall speed of a rain drop depends on its diameter D and the environmental pressure. An empirical formula according to [7] is given as

$$V_\infty(D, p_0) = \begin{cases} 0 & D \leq 0.03\,\text{mm} \\ 4.323\,(D - 0.03\,[\text{mm}]) & 0.03\,\text{mm} < D \leq 0.6\,\text{mm} \\ 9.65 - 10.3\,e^{-0.6\,D} & D > 0.6\,\text{mm} \end{cases} \tag{5.2}$$

where the drop size diameter D is inserted in mm. The formula is only valid for the standard environmental pressure p_0 of 1013 hPa.

A correction factor according for the environmental pressure is given by

$$V_\infty(D, p) = V_\infty(D, p_0) \left(\frac{p_0}{p}\right)^{0.291 + 0.0256\,D} \tag{5.3}$$

with $p_0 = 1013\text{hPa}$ and D in mm.

Figure 5.4 shows the fall velocities at pressure levels of 500, 750 and 1000 hPa as a function of the drop size diameter. We see that the influence of the diameter is large for small drop diameters and weak if the drops are large.

5.5.1 Characteristic Fall Velocity of Rain

The fall velocity depends on the drop size. Thus, it is individual for each drop. To describe an effective fall velocity of the rain, we have to define the characteristic fall velocity.

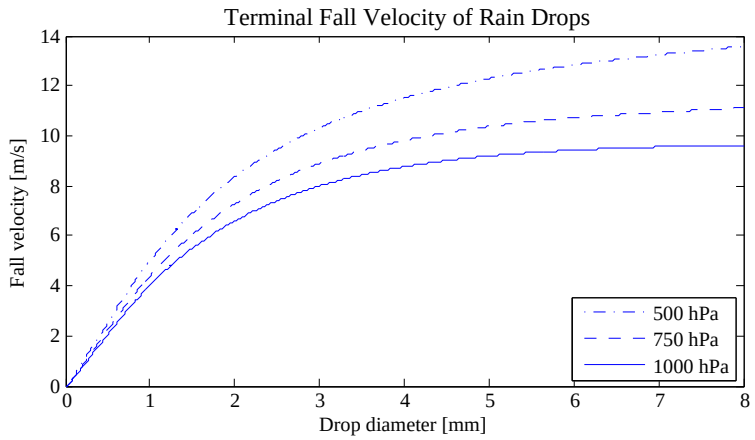

Figure 5.4: Terminal fall velocity as a function of drop diameter. Curves shown for 1000 hPa (solid), 750 hPa (dashed) and 500 hPa (dash-dotted).

There are various definitions possible. For example, it can be defined as first moment of the drop size distribution weighted by D^6.

$$V_m = \frac{\int_0^\infty N(D)\, D^6\, V_\infty(D)\, dD}{\int_0^\infty N(D)\, D^6\, dD} \tag{5.4}$$

V_m is the characteristic fall velocity and $N(D)$ is the drop size distribution.

When we talk about the fall velocity of precipitation or of a drop size distribution, we mean the characteristic fall velocity according Equation (5.4).

Figure 5.5 shows the characteristic fall velocity as function of the rain rate. From the rain rate we calculated the drop size distribution according to Marshall-Palmer.

5.6 Rain Rate

Knowing the drop size distribution and the fall velocity we can calculate the rain rate as

$$R = \frac{\pi}{6} \int_0^\infty D^3\, N(D, R)\, V_\infty(D, p) dD \tag{5.5}$$

where R is the rain rate, $N(D, R)$ the drop size distribution and $V_\infty(D, p)$ the fall velocity as function of drop size D and pressure p.

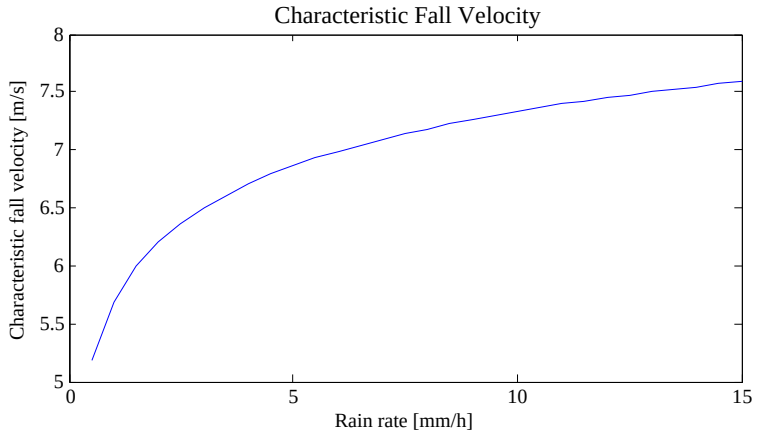

Figure 5.5: Characteristic fall velocity as a function of the rain rate using the Marshall-Palmer drop size distribution and an environmental pressure of 1013 hPa.

Chapter 6

TROWARA (Tropospheric Water Vapor Radiometer)

6.1 Overview

The TRopospheric WAter vapor RAdiometer (TROWARA) has operated since 1994 on the roof of the ExWi building. It was designed to measure integrated water vapor (IWV) and integrated liquid water (ILW). And now, we try to expand its functionality to estimate rain and snow as well. A very short description about its functionality is given in the STARTWAVE atmospheric database ([17]), for more detailed information see Peter and Kämpfer, 1992 [19] and Morland, 2002 ([18]).

TROWARA observes the sky at the fixed zenith angle of 50°. It contains three microwave sensors. One operates at 21.3 GHz (BW = 100 MHz) which is sensitive to the water vapor absorption line at 22.235 GHz, another sensor measures at 31.5 GHz (BW = 200 MHz) which is more sensitive to liquid water, and since November 2007 a third sensor at 22.2 GHz (BW = 400 MHz) was added which is even more sensitive to water vapor as the 21.3 GHz sensor. Additionally, a thermal IR sensor ($\lambda = 9.5 - 11.5\ \mu$m) measures radiation from the same direction.

The original method to retrieve water vapor and liquid water uses a model of Wu (see Peter and Kämpfer, 1992 [19]). It is based on the linearization of brightness temperatures in analogy to opacities. But it was pointed out by Mätzler and Morland, 2008 [14] that Wu's assumption that the absorption of cloud liquid water is proportional to the square of the frequency was erroneous, especially at low temperatures. Therefore a new algorithm based on statistical analysis was built and later this algorithm was refined with physical considerations.

6.2 Statistical Algorithm

A short summary about the statistical algorithm is given, for further information see Mätzler and Morland, 2008 ([14]).

Figure 6.1: TROWARA on the roof of the ExWi building.

The idea behind this algorithm is that the parameters of interest can be estimated by linear combinations of measured data. The measured data are the brightness temperatures by TROWARA and surface temperature, pressure, relative humidity and other parameters measured by the weather station on the roof of the ExWi building. The coefficients weighting the measured parameters are determined by statistical methods in comparison with radiosonde data.

Thus, the effective mean temperature T_{mi} of the atmosphere at microwave frequency f_i can be estimated by ground-based data as

$$T_{mi} = A_{0i} + A_{1i}\,T_S + A_{2i}\,U_S + A_{2i}\,P_S \quad . \tag{6.1}$$

T_S denotes the temperature, U_S the relative humidity and P_S the pressure at the surface. The index i stands for the frequency f_i. The coefficients A_{ji} are determined by radiosonde data using the radiative model of Rosenkranz.

Knowing the effective mean temperature T_{mi}, we can use Equation (2.36) to calculate the opacities τ_i for each frequency.

$$\tau_i = -\mu \ln\left(\frac{T_{mi} - T_{bi}}{T_{mi} - T_c}\right) \tag{6.2}$$

T_{bi} denotes the measured brightness temperature, T_{mi} the effective mean temperature and T_c is the cosmic background temperature. μ is the cosine of the zenith angle.

The integrated water vapor (IWV) and the integrated liquid water (ILW) can be fitted by a linear combination of the opacities τ_{21} and τ_{31} considering temperature, dry-air density and water vapor density measurements at the surface.

$$IWV = B_0 + B_1\,\tau_{21} + B_2\,\tau_{31} + B_3\,T_S + B_4\,D_S + B_5\,V_S \tag{6.3}$$

$$ILW = C_0 + C_1\,\tau_{21} + C_2\,\tau_{31} \tag{6.4}$$

T_S is the temperature, D_S the dry-air density and V_S the water vapor density at the surface.

We can use the third TROWARA sensor at 22.2 GHz and find a statistical retrieval in the same manner as described above.

In general the statistical algorithms have high accuracy. But due to enhanced microwave sensitivity to large water drops, the presence of precipitation leads to large systematic errors.

6.3 Refined Algorithm

The zenith opacities during rainless periods can be found in the same manner as described by Equation (6.1) and (6.2). An useful property of the opacity is that it can be divided into the opacities of different matter. Thus, the opacity of the entire atmosphere can be interpreted as sum of the opacities of the clear sky, the water vapor and the liquid water, as done in the following equation.

$$\tau_{21} = a_{21} + b_{21}\,IWV + c_{21}\,ILW \tag{6.5}$$

$$\tau_{31} = a_{31} + b_{31}\,IWV + c_{31}\,ILW \tag{6.6}$$

where τ_{21} and τ_{31} are the zenith opacities according to Equation (6.2) for 21 and 31 GHz, respectively. a_{21} and a_{31} represent the dry atmosphere opacities. They depend on the temperature and pressure. They are rather constant, when divided by the dry air density D_S . The parameters b_{21} and b_{31} are the coefficients weighting the amount of water vapor in the atmosphere. It turns out that b_{21} is rather constant and can be determined by statistical methods using radiosonde data (see Equation (6.7)). The parameters c_{21} and c_{31} are the Rayleigh mass absorption coefficients of cloud water, which can be calculated using the dielectric model of water by Ellison (2006).

The parameter b_{21} can be estimated by

$$b_{21} = D_0 + D_1\,\tau_{21} + D_2\,\tau_{31} + D_3\,T_S + D_4\,V_S \tag{6.7}$$

where τ_{21} and τ_{31} are the zenith opacities, T_S is the temperature and V_S is the water vapor density at the surface. And D_0 to D_4 are the statistically determined parameters.

We define the ratios of the corresponding coefficients as follows

$$\alpha = \frac{a_{21}}{a_{31}} \qquad \beta = \frac{b_{31}}{b_{21}} \qquad \gamma = \frac{c_{21}}{c_{31}} \tag{6.8}$$

where $\alpha \approx 0.5$, $\beta < 0.5$ and $\gamma \approx 0.5$. The ratio β is more variable, it depends on the mean air pressure of the humid air, and thus on the water vapor profile. For example, if the humidity is located near the surface, the humid air pressure is high. This broadens the water vapor absorption line. Thus, the absorption coefficient (b_{21}) near the absorption line gets a bit smaller but the absorption coefficient (b_{31}) at higher frequencies gets large (see Figure 6.2). Thus, β is large when the humidity is located in the lower atmosphere and small when the water vapor is aloft, respectively.

Assuming that we know all the coefficients and the opacities in the Equation (6.5) and (6.6), we can solve the mentioned equations for IWV and ILW. We get

$$IWV = \frac{\tau_{21} - a_{21} - \gamma\,(\tau_{31} - a_{31})}{b_{21}\,(1 - \beta\,\gamma)} \tag{6.9}$$

$$ILW = \frac{\tau_{31} - a_{31} - \beta\,(\tau_{21} - a_{21})}{c_{31}\,(1 - \beta\,\gamma)} \quad . \tag{6.10}$$

6.3.1 Cloud-free Periods

If the sky is cloud-free, the integrated liquid water drops out ($ILW = 0$) in (6.9) and (6.10). And we get for IWV:

$$IWV = \frac{\tau_{21} - a_{21}}{b_{21}} \tag{6.11}$$

And β is determined by

$$\beta = \frac{\tau_{31} - a_{31}}{\tau_{21} - a_{21}} \tag{6.12}$$

Criteria for Cloud-free Periods

We define two criteria to detect cloud-free periods. The first criterion considers the infrared temperature, the second one the standard deviation of the ILW.

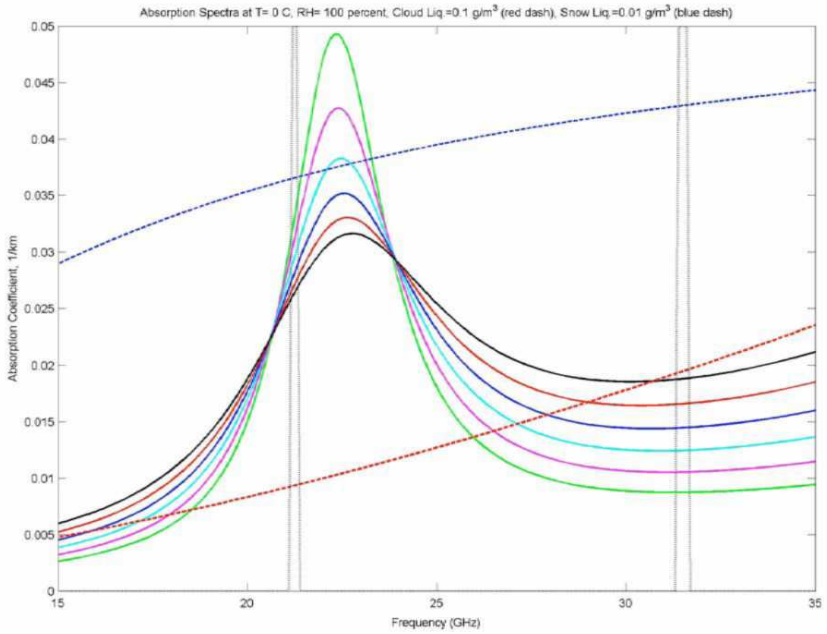

Figure 6.2: Absorption spectra of water vapor, rain and wet snow. The absorption coefficients of water vapor are the solid lines shown for pressure from 500 to 1000 hPa. The red dashed line shows the Rayleigh absorption for rain and the blue dashed line for wet snow. The grey vertical lines indicate where the measuring frequencies of TROWARA are located.

Infrared temperature: Knowing the integrated water vapor (IWV), an empirical fit for the maximal possible cloud-free infra-red brightness temperature $T_{B,IR,nocloud}$ (claimed by Emmanuel) is given by

$$T_{B,IR,nocloud} = 192 + 3 \cdot IWV - 0.032 \cdot IWV^2 \qquad [\mathrm{K}] \quad . \tag{6.13}$$

IWV has to be inserted in mm.

Thus, if the measured IR temperature ($T_{B,IR}$) is below this empirical limit, we assume that we have a no cloud situation.

$$T_{B,IR} < T_{B,IR,nocloud} \tag{6.14}$$

Standard deviation of ILW: During a cloud-free period, the ILW value is very small ($ILW \approx 0$) and additionally it is very stable. Thus, we can define our second criterion for cloud-free situation:

$$\sigma_{ILW} < 0.0011 + 0.000012 \cdot \overline{T_S} \qquad [\mathrm{mm}] \tag{6.15}$$

The mean surface temperature $\overline{T_S}$ must be inserted in °C. If the standard deviation of ILW (σ_{ILW}) is smaller than 0.0011 mm (plus a temperature depend term), we have a cloud-free situation. Note that the term on the right side of the inequation is only valid if the TROWARA ILW samples are averaged over 12 seconds. For unaveraged ILW values, σ_{ILW} is higher. Additionally to this criterion, the IR temperature must be below 265 K, because small σ_{ILW} values are also possible during stable fog situations.

If at least one of the two criteria is fulfilled, we assume that we have a cloud-free situation, and we can use Equation (6.12) to calculate β.

6.3.2 Example of TROWARA Measurements on a Rainless Day

Figure 6.3 shows measurements from April 7, 2009. This day was a rainless day with blue sky in the morning and clouds in the afternoon. The temperature was at about 10°C during the night and increased up to almost 20°C shortly after midday.

Figure (a) shows the infrared temperature during this day. In the first half of the day, the IR temperature was between 210 and 220 K (corresponding to ≈ -60°C). After 12:00 the temperature changed rapidly between about 220 and 270 K. The infrared sensor measures the temperature of the clouds. If no clouds are present, the temperature is very low and if cloud exists the temperature of the lowest cloud layer is measured. Thus, the first half of April 7, 2009 was cloud-free while the sky was covered with clouds in the afternoon (interrupted by some holes in the cloud cover).

Figure (b) shows the brightness temperature for 21 (blue) and 31 GHz (red). In the morning the curves are stable, and in the afternoon we clearly see the influence of the clouds.

Figure (c) shows the zenith opacities calculated with Equation (6.2). We see the influence of the clouds in the afternoon again. Especially the 31 GHz opacity (red line) is sensitive to the liquid water.

Figure (d) shows the characteristic of the β parameter defined by Equation (6.8). The red circles show the β values when the algorithm detected a cloud-free period according to the defined criteria. The black line is the estimation of the β parameter during cloud periods or when no data were available. We see that β decreased during the morning. Thus, the water vapor was lifted up in the morning. Lifting of air masses leads to cooling and condensing of the water vapor leading to clouds in the afternoon.

Figure (e) shows the calculations of IWV and ILW according to the refined algorithm (Equation (6.9) and (6.10)). The amount of liquid water (ILW) is zero at cloud-free periods and increases when clouds are present. The IWV was stable during the morning and increased in the afternoon. The amount of water vapor can increase, when moister air masses reach the observed region by advection or when water is evaporated and lifted from the ground. Looking at the β parameter, we see that β is still decreasing while the IWV is increasing. Thus, the amount of water vapor was accumulating in the upper atmosphere, probably lifted up by convection and accumulated by advection. In the later afternoon, β increased. This corresponds to a higher amount of water vapor at lower altitudes, confirming the assumption that the increase of the IWV is generated by evaporation of surface water.

6.3.3 Rain

The same approach as done for situations without precipitation (Equation (6.5) and (6.6)) can be used to describe the zenith opacities τ_{21} and τ_{31} for situations with rain and snow. But we have to include two additional terms. The first represents the absorption of rain, the second the absorption of wet snow. Due to the small absorption of ice, the contribution of ice and dry snow can be neglected.

The zenith opacities can be calculated as

$$\tau_{21} = a_{21} + b_{21}\,IWV + c_{21}\,(ILW + G_{M,21}\,IRL) + d_{21}\,ISL \quad (6.16)$$

$$\tau_{31} = a_{31} + b_{31}\,IWV + c_{31}\,(ILW + G_{M,31}\,IRL) + d_{31}\,ISL \quad (6.17)$$

where IRL is the integrated rain liquid and ISL integrated snow liquid. The term $G_{M,i}$ represents the Mie gain of rain. The Mie gain of rain is increasing rapidly for drop diameters larger than 0.3 mm. The Mie gain at 21 GHz $G_{M,21}$ can reach values up to 10 and at 31 GHz $G_{M,31}$ up to 7 (see Figure 6.4).

The coefficients d_{21} and d_{31} represent the emission of wet snow at 21 GHz and 31 GHz, respectively. The emission of wet snow is larger than the emission of rain ($d_i >> c_i$).

The ratio of the wet snow coefficients (d_{21} to d_{31}) is defined as δ and it is larger as the ratio of the rain coefficients (γ).

$$\delta = \frac{d_{21}}{d_{31}} > \gamma = \frac{c_{21}}{c_{31}} \quad (6.18)$$

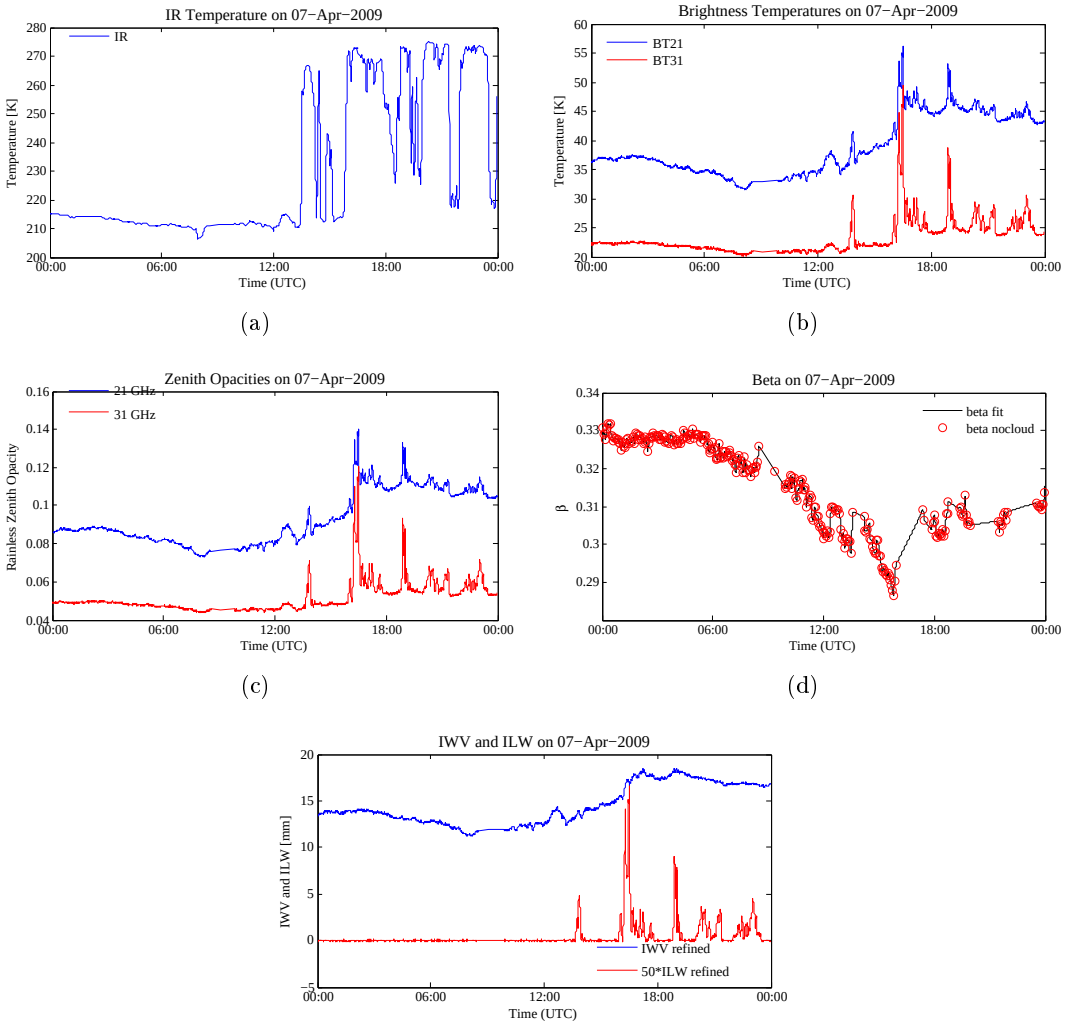

Figure 6.3: TROWARA measurements on April 7, 2009. Figure (a) shows the infrared temperature, (b) the measured brightness temperature for 21 (blue) and 31 GHz (red), (c) the zenith opacities for 21 (blue) and 31 GHz (red), (d) the β-parameter and (e) IWV (blue) and ILW (red) calculated with the refined algorithm.

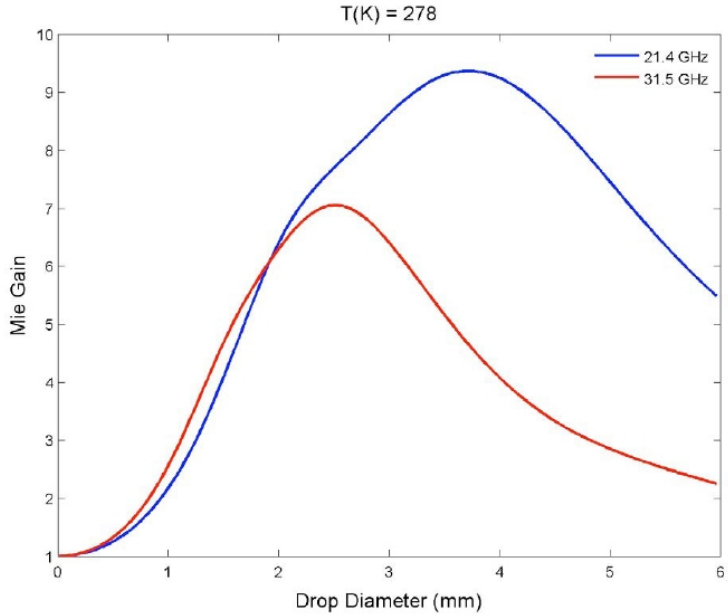

Figure 6.4: The Mie gain for 21 (blue) and 31 GHz (red) as function of the drop diameter (Figure from [14]).

Criteria for Rain Periods

At the beginning of a rain period the ILW value increases fast due to the increase of the Mie gain. Thus, we can define an ILW threshold value ILW_R and assuming that it is raining if

$$ILW > ILW_R \quad . \tag{6.19}$$

ILW is calculated with either the statistical or the refined algorithm. The threshold value ILW_R has usually a value in the range from 0.1 to 0.4 mm.

Even an inaccurate threshold value ILW_R is sufficient to determine the beginning of a rain period.

Estimation of the Rain Rate

During rain periods the total opacity can be interpreted as sum of the opacity of the rain and the opacity without rain. We assume that the opacity without rain is relatively constant during rain periods. Thus, the opacity of rain is the difference between the measured opacity τ_i and the opacity value at the beginning of the rain period (denoted as $\tau_{R,i}(ILW_R)$). $\tau_{R,i}(ILW_R)$ is the opacity when ILW satisfies the criterion for a rain period (Equation (6.19)). The index i stands for the frequency.

$$\Delta\tau_i = \tau_i - \tau_{R,i}(ILW_R) \tag{6.20}$$

Here $\Delta\tau_i$ represents a first estimation of the rain opacity. Unfortunately, τ_i is based on an estimation of the effective mean temperature T_{mi} which is not very accurate during rain periods. Therefore the opacity of rain $\Delta\tau_i$ is not accurate as well. We have to find another method to improve the expression for the rain opacity. Such a method is described in the next subsection. In the following we use the term $\tau_{rain,i}$ for the improved rain opacity.

It can be shown that the absorption coefficient of rain $\gamma_{a,R,i}$ in the frequency range from 21 to 31 GHz is proportional to the rain rate R.

$$\gamma_{a,R,i} = R \cdot g_{R,i} \tag{6.21}$$

where $\gamma_{a,R,i}$ is the absorption coefficient of rain, R is the rain rate and $g_{R,i}$ is the proportionality factor.

Knowing the absorption coefficient $\gamma_{a,R,i}$ and the depth of the rain layer H_R, we can calculate the rain opacity $\tau_{rain,i}$. We assume that the rain rate is constant within the whole rain layer.

$$\tau_{rain,i} = H_R \cdot \gamma_{a,R,i} \tag{6.22}$$

The depth of the rain layer H_R is equal to the distance from ground up to the height where the ambient air temperature is 1°C. Above this height it is snowing and at the moment we do not consider the contribution of the wet snow to the opacity. H_R is calculated from the surface temperature T_S assuming a constant moist-adiabatic lapse rate Γ .

$$H_R = \frac{T_S - 274.15}{\Gamma} \tag{6.23}$$

where the surface temperature T_S must be inserted in K. The lapserate Γ depends on the weather situation and is between 4 and 8 K/km.

Using Equation (6.21) and (6.22) we get for the rain rate R

$$R = \frac{\tau_{rain,i}}{H_R\, g_{R,i}} \quad . \tag{6.24}$$

Rain Opacity

As mentioned above, the estimation of the effective mean temperature T_{mi} is not very accurate during rain periods. And thus, the values of the total opacity τ_i and the rain opacity $\Delta\tau_i$ are not accurate in a first estimation. In the following we describe a method to get a better estimation of the rain opacity $\tau_{rain,i}$.

We assume that the rain is constant within a layer with depth H_R. Thus, the measured brightness temperatures at the ground can be expressed using Equation (2.36).

$$T_{b,i} = T_{b,norain,i}\, e^{-\tau_{rain,i}/\mu} + T_{m,rain,i}\,(1 - e^{-\tau_{rain,i}/\mu}) \tag{6.25}$$

where $T_{b,i}$ is the measured brightness temperature at frequency i, $T_{b,norain,i}$ is the brightness temperature of the atmosphere including water vapor and cloud liquid water above the rain layer. $\tau_{rain,i}$ is the rain opacity and $T_{m,rain,i}$ is the effective mean temperature of the rain layer.

The brightness temperature without rain ($T_{b,norain,i}$) is given by

$$T_{b,norain,i} = T_c\, e^{-\tau_{R,i}/\mu} + T_{mi}\,(1 - e^{-\tau_{R,i}/\mu}) \tag{6.26}$$

where T_c denotes the cosmic background temperature. $\tau_{R,i}$ is the opacity just at that moment when the rain started (and it is assumed to be constant during rain periods). T_{mi} is the effective mean temperature of the atmosphere calculated with Equation (6.1).

The effective mean temperature $T_{m,rain,i}$ of the rain layer is determined by Equation (2.37) as

$$T_{m,rain,i} = \frac{\int_0^{\tau_{rain,i}/\mu} T(\tau)\, e^{-\tau}\, d\tau}{1 - e^{-\tau_{rain,i}/\mu}} \tag{6.27}$$

Assuming that the temperature decreases linearly within the rain layer, we can write for the temperature within the rain layer:

$$T(\tau) = T_S - \Gamma\, h(\tau) = T_S - \Gamma\, \frac{\tau\ \mu}{\gamma_{a,R,i}} \tag{6.28}$$

where T_S is the surface temperature, $h(\tau)$ the depth of the layer with opacity τ, Γ the lapse rate and $\gamma_{a,R,i}$ is the absorption coefficient of rain.

Inserting (6.28) in (6.27) we can simplify the expression for $T_{m,rain,i}$ to (for more details see [14]):

$$T_{m,rain,i} = T_S - \frac{1}{2}\,(T_S - T_{ml})\, e^{-0.19\,\tau_{rain,i}/\mu} \tag{6.29}$$

where T_{ml} is the temperature in the melting layer. T_{ml} is about 1°C.

Now, we would like to know the rain opacity $\tau_{rain,i}$. Thus, we solve Equation (6.25) for $\tau_{rain,i}$ and we get

$$\tau_{rain,i} = -\mu \ln\left(\frac{T_{m,rain,i} - T_{b,i}}{T_{m,rain,i} - T_{b,norain,i}}\right) \quad . \tag{6.30}$$

In this equation we know $T_{b,i}$, $T_{b,norain,i}$ is calculated with Equation (6.26) and $T_{m,rain,i}$ can be calculated using Equation (6.29). But Equation (6.29) uses the unknown rain opacity $\tau_{rain,i}$.

We proceed iteratively to calculate $\tau_{rain,i}$. First, we use $\Delta\tau_i$ from (6.20) as first estimation of $\tau_{rain,i}$ in (6.29). We get the effective mean temperature $T_{m,rain,i}$ of the rain layer as result. We insert this result in Equation (6.30) and get a second estimation of $\tau_{rain,i}$.

Then, we do the same procedure again to get a third estimation of $\tau_{rain,i}$. It is shown that two iteration steps are sufficient to get an accurate estimation of the rain opacity.

6.3.4 Limitations of the Refined Algorithm

Wet snow

We considered the contribution of rain to the total opacity τ and neglected the contribution of wet snow. Although the layer of wet snow is just a few hundred meters thick, its contribution cannot be neglected.

Later, we will describe a method to estimate the influence of snow to improve this algorithm.

Depth of the rain layer

The depth of the rain layer is estimated by the surface temperature assuming a constant lapse rate. The exact value of the lapse rate is not known. For example, if we assume that the depth H_R is 600 m but in reality it is only 300 m, we underestimate the rain rate R by a factor of two.

In Chapter 9 we will show how we can use a vertical pointing rain radar to get more accurate values for the depth of the rain layer.

6.3.5 Example of TROWARA Measurements for a Rainy Day

Here, we consider measurements made on a rainy day. We selected July 13, 2008. It was almost continuously raining during that day with some rainless periods or periods with very little rain (especially between 11:00 and 17:00).

The lapserate was about 6 K/km and we set the IWL threshold value (ILW_R) to 0.4 mm. As there were no cloud-free periods during that day, the β parameter could not be determined and it was set to a mean value of 0.32.

A collection of measurement results is shown in Figure 6.5.

To begin with the main result, Figure (a) shows the cumulative rain estimated by TROWARA using the 21 (blue) and 31 GHz (red) channel. To verify this estimation the cumulative rain measured at the ground is shown by the green lines (the solid green line represents the tipping sensor and the green dashed line the optical sensor respectively). We see that the beginnings and endings of the rain periods of the TROWARA estimations agree well with the rain periods measured at the ground. The rain intensity is most of the time overestimated leading to a too large amount of rain at the end of the day. Increasing the ILW threshold value ILW_R leads to less rain but also to a shortening of the rain periods. The lapserate was determined by a vertical pointing rain radar but we cannot say if it was constant within the rain layer. And we did not consider the influence of the wet snow in the melting layer.

Figure (b) shows the brightness temperatures measured at 21 (blue) and 31 GHz (red). We see that the brightness temperatures are higher during rain periods.

Figure (c) shows the rainless zenith opacities (again blue for 21 and red for 31 GHz). The rainless opacities are clipped during the rain periods as our algorithm assumes that ILW stays constant within a rain period.

Figure (d) shows the rain opacities. They are zero at rainless periods and have a value larger than zero when the rainless opacities are clipped. The peak rain opacities can be a factor of 3 to 4 times larger than the rainless opacities. To get the total opacity, we have to add the opacities of Figure (c) and (d).

In Figure (e) the IWV (blue) and ILW (red) are shown. Remember that the ILW cannot increase over the ILW threshold value by definition. Thus, it is constant during rain periods. It is surprising how fast it can change during rainless periods.

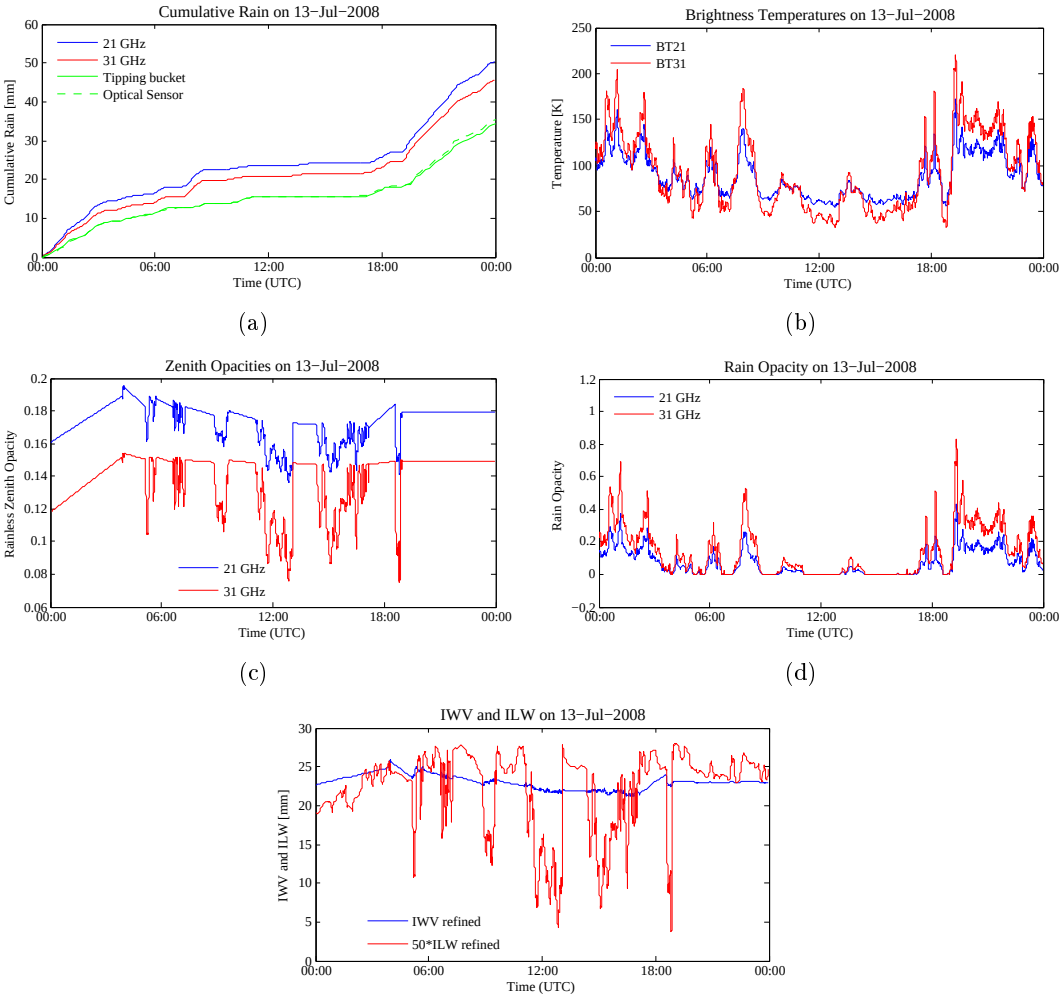

Figure 6.5: TROWARA measurements on July 13, 2008. Figure (a) shows the cumulative rain estimated by 21 (blue) and 31 GHz (red) and by the tipping bucket (green) and by the optical rain sensor (green dashed). Figure (b) shows the brightness temperatures at 21 (blue) and 31 GHz (red). Figure (c) shows the rainless zenith opacities and Figure (d) the rain opacities. IWV (blue) and ILW (red) is shown in Figure (e).

Chapter 7

The Micro Rain Radar (MRR)

7.1 Overview

The Micro Rain Radar (MRR) is a vertical pointing FM-CW Doppler Radar. *Vertical pointing* because it sends electromagnetic (EM) waves only in one direction, namely straight upward. FM-CW stands for Frequency Modulated Continuous-Wave. That means the MRR continuously transmits EM-waves while the frequency varies (modulates). The mean frequency is 24 GHz corresponding to a wavelength of about 1.24 cm.

The transmitted EM-waves are influenced by the matter in the atmosphere, mainly by rain drops, hail, graupel and snowflakes. A part of the EM-waves is reflected towards the ground and can be detected by the receiver of the MRR. The reflected signal gives information about the amount, speed and the size of the drops in the atmosphere. As the drops are falling in direction to the ground, we can use the Doppler effect to determine the fall speed. How this is done is shown in detail later in this chapter (see Section 7.2).

From the fall speed distribution we can derive many other parameters like the drop size distribution, the rain rate and the liquid water content. To see how this is done, see Section 7.3.

The EM-waves need some time to propagate through the atmosphere. Thus, the reflection of droplets close to the MRR reach the receiver earlier than the reflection of far droplets. According to this propagation time we can distinguish between 30 height levels. The resolution distance between two height levels can be configured. We set them to 100 m and later to 50 m.

A summary with all technical details is given in the table at the end of this chapter (Table 7.1).

Our MRR is located on the roof of the ExWi building of the University of Bern (see Figure 7.1). On the same roof the tropospheric water vapor radiometer (TROWARA) is located directly next to the MRR and a weather station is there too. Thus, it is possible to combine or to compare measurement results from all instruments.

In this chapter we look at the signal processing part of the received radar signal and how the atmosphere-relevant parameters are derived. But we do not go into the

Figure 7.1: The Micro Rain Radar on the roof of the ExWi building. The transmitter and receiver are located in the metallic box shown at the upper left corner. The parabolic dish redirects the radiation from the transmitter to the vertical and from the vertical to the receiver, respectively.

details of the radar hardware. The interested reader can find technical information about the radar front-end in the manuals of the manufacturer ([15, 16]).

7.2 Signal Processing

In Figure 7.2 a schematic overview over the digital signal processing part of the MRR is given. Each block shown in this figure is described below. Here, just a short summary is given.

As the MRR works in FM-CW mode, the transmit signal $s(t)$ is a frequency modulated, continuous wave signal. The frequency of this signal changes periodically and during one period, called sweep, the frequency is linearly decreased.

The receive signal $r(t)$ depends on the location, the number and the sizes of the rain drops above the MRR. To interpret its strength we have to consider the radar equation and the scattering of the radiation at the rain drops.

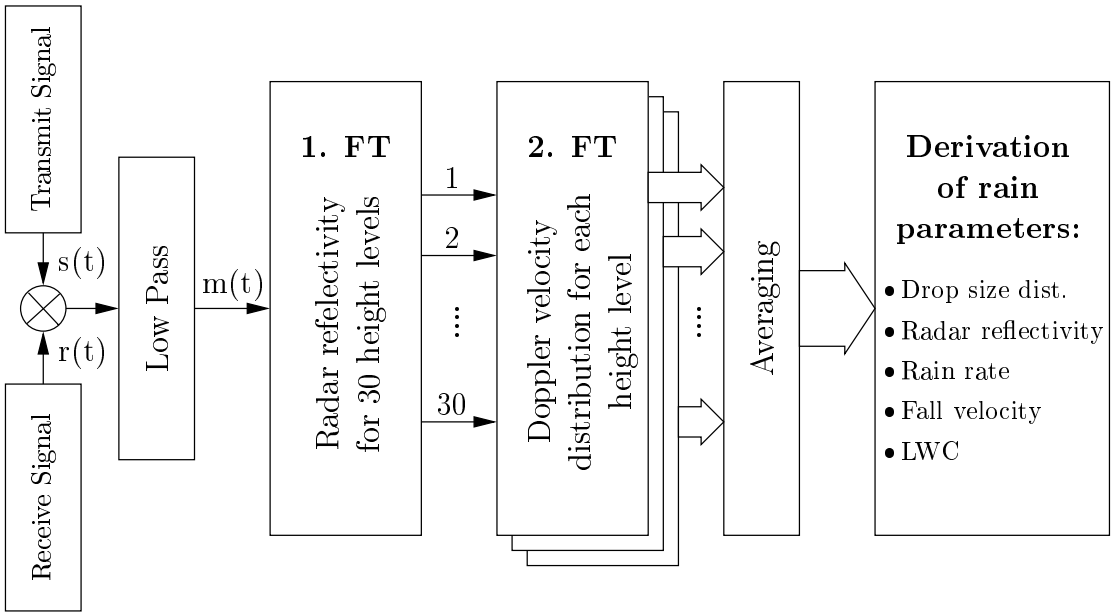

Figure 7.2: Overview of the signal processing in the MRR. First, the transmit and the receive signals are mixed. Then, by a first Fourier Transform (FT) the reflectivity of each of the 30 height levels is calculated. By the second FT the Doppler velocity distribution of each height level is determined. After the averaging the relevant rain parameters are derived. These are the drop size distribution, the radar reflectivity, the fall velocity, the rain rate and the liquid water content.

The transmit signal $s(t)$ and the receive signal $r(t)$ are mixed and the high frequency part is filtered by the low pass. Then the achieved signal $m(t)$ is sampled and a first Fourier Transform (FT) is performed. The Fourier spectrum represents the strength

of the radar reflectivity at different height levels. Such a spectrum is calculated after every sweep. Now, for each height level a series of such Fourier values is taken and a second FT is made. Thus, we get a Doppler velocity distribution for every height level.

As the received signal depends on a large number of rain drops and therefore contains a large stochastic component, a series of the Doppler velocity distributions is averaged. As a result, every 10 seconds an averaged 60 point Doppler velocity spectrum is given for each of the 30 height levels.

From this result many different rain parameters such as the drop size distribution, the radar reflectivity, the fall velocity, the rain rate and the liquid water content are calculated (see Section 7.3).

7.2.1 Frequency Modulated Continuous-Wave (FMCW) Radar

The MRR is a frequency modulated continuous-wave (FMCW) radar. This is a radar system where the transmit frequency is modulated in a triangular sweep around the mean frequency f_0. In contrary to pulsed radar systems the signal is transmitted and received continuously.

The transmit frequency is a function of time t and is given by the following function during one sweep. This sweep is repeated periodically.

$$f(t) = f_0 - \frac{B}{T}t \quad \text{for} - T/2 \leq t \leq T/2 \tag{7.1}$$

where f_0 denotes the mean frequency (24.1 GHz in our case), B is the bandwidth (between 0.75 MHz and 4.3 MHz) and $T = 256\,\mu s$ the period of one sweep (see Figure 7.3). In the following equations the condition $-T/2 \leq t \leq T/2$ must be considered as they describe the behavior of one sweep only.

The phase $\varphi(t)$ of the transmitted signal is given by the integral over the frequency $\varphi(t) = \int_0^t 2\pi f(t')dt' = 2\pi f_0 t - 2\pi B/(2T)\, t^2$. This relation gives the function of the transmitted signal $s(t)$,

$$s(t) = S \sin\left(\varphi(t)\right) = S \sin\left(\omega_0 t - 2\pi \frac{B}{2T} t^2\right) \tag{7.2}$$

with $\omega_0 = 2\pi f_0$ and S is the amplitude of $s(t)$.

If we consider a non-moving object at distance h, the reflected signal is attenuated and delayed by the time t_h

$$r(t) = R \sin\left(\omega_0 (t - t_h) - 2\pi \frac{B}{2T} (t - t_h)^2\right) \tag{7.3}$$

The delay time t_h is equal to $2h/c$, where c denotes the speed of light. Because the frequency is deceasing during one sweep, the frequency of $r(t)$ is higher than the frequency of $s(t)$ at the time t.

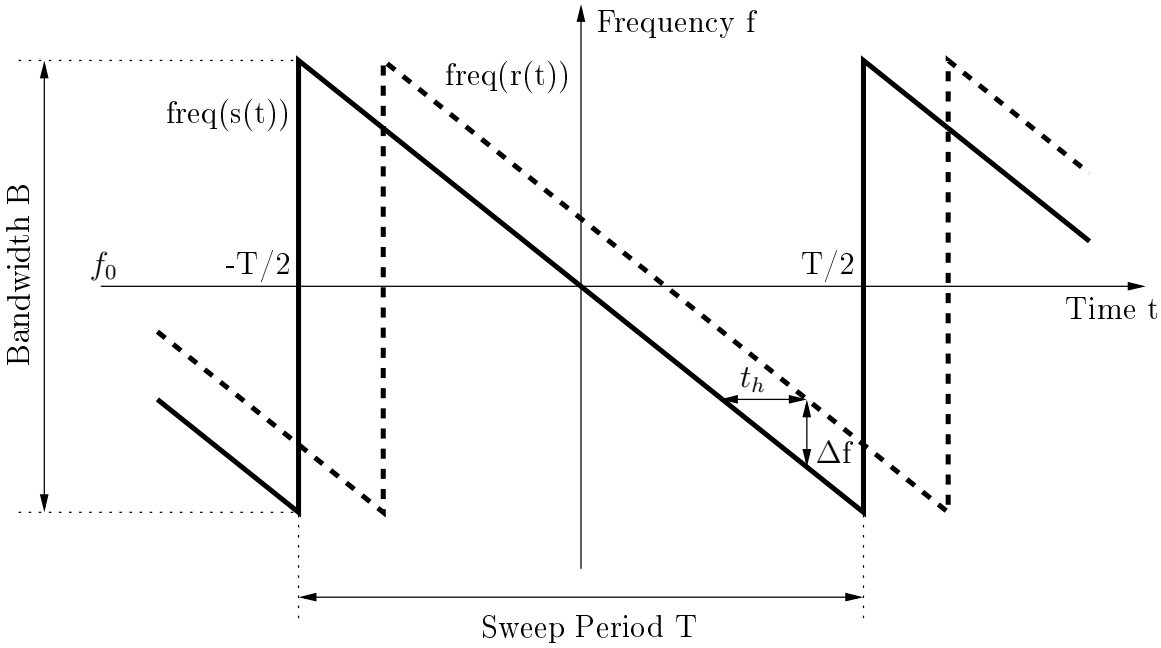

Figure 7.3: Characteristic of the frequency during one sweep. The frequency is linearly decreasing and at the end of the sweep it jumps back. The receive signal is delayed.

The difference Δf of the transmitted and received frequency corresponds to the frequency change the signal $s(t)$ made during the travel time t_h.

$$\Delta f = \frac{B}{T} t_h = \frac{B}{T} \frac{2h}{c} \tag{7.4}$$

7.2.2 Height Resolution

To get the frequency difference Δf, the transmitted signal $s(t)$ is multiplied by the received signal $r(t)$ and the high-frequency part is filtered out. This leads to the mixed signal $m(t)$. The frequency spectrum received by the Fourier Transform of $m(t)$ represents the distances to the reflecting objects. Let us define that this is the 1^{st} Fourier Transform (1^{st} FT). Later we will see that we need a second Fourier Transform to retrieve the Doppler velocity distribution of the rain droplets.

The frequency resolution of the discrete Fourier Transform is related to the inverse of the time period within the signal is measured. For our saw-tooth signal this period must be shorter than the time T. Hence, the maximal frequency resolution cannot be smaller than $1/T$. If we apply Equation (7.4) to this fact, we can replace Δf by $1/T$ and solve now for the height difference Δh. This leads to

$$\Delta h = \frac{1}{2} \frac{c}{B} \quad . \tag{7.5}$$

We notice that the height resolution depends on the bandwidth B. If we set the bandwidth B to 1.5 MHz, the height resolution is 100 m.

The number of height levels depends on the number of samples used for the 1^{st} FT. The MRR calculates 30 height levels.

7.2.3 Doppler Velocity

If we consider a moving object there is an additional frequency shift caused by the Doppler effect. We assume that the object is moving towards the receiver (like a down-falling raindrop). This leads to an increase of the receive frequency. We remember from Equation (3.14) that the frequency shift is given by

$$f_D = \frac{2}{\lambda} v \tag{7.6}$$

where λ is the wavelength of the transmit signal and v is the velocity component of the falling drop towards the receiver.

Note that the Doppler velocity is the absolute velocity related to the MRR. If an object and the surrounding medium are moving, we can determine the velocity of the scatterers only.

7.2.4 Distribution of the Terminal Fall Velocity

The total frequency shift of a falling object is the sum of the frequency shift caused by the height (Eq. (7.4)) and by the Doppler effect (Eq. (7.6)):

$$\Delta f_{total} = \Delta f + f_D = B\frac{2h}{cT} + \frac{2}{\lambda} v \tag{7.7}$$

The frequency resolution of the 1^{st} FT of the received signal is equal to the inverse of the sweep period ($1/T$). The sweep period T is equal to 256 μs, leading to a frequency resolution of about 3.9 kHz. If we consider a fast falling rain drop, then its fall velocity can be about 10 m/s, leading to a Doppler frequency shift f_D of about 1.6 kHz. Thus, the frequency shift caused by the Doppler effect can be almost the half of the frequency resolution of the 1^{st} FT. As the Doppler effect increases the frequency of the received signal, a fast falling rain drop can contribute to the FT frequency line of the next upper height level as a slower rain drop at the same height.

Looking at one Fourier spectrum only, we cannot distinguish between the fraction of the frequency shift caused by the height and the fraction caused by the Doppler effect. To get this information we have to consider a series of consecutive Fourier spectra.

Two consecutive Fourier spectra are calculated in a time interval of 256 μs. A fast rain drop has a fall velocity of about 10 m/s. Thus, between the measurement of two Fourier spectra a fast rain drop falls only about 2.5 mm. This is negligible compared to the height resolution of 50 m or 100 m. And it is a good assumption that every rain

drop contributes to the same height range considering a series of consecutive Fourier spectra.

What is the difference between two consecutive Fourier spectra, if every rain drop contributes to the same height range in both spectra? - It is the phase that changes. Due to the small distance a rain drop covered between the measurement of the two spectra, the phase is shifted. How much the phase changes, depends on the velocity of the rain drop. Considering a time series of a specific height range, we can determine the frequency of the phase changes and hence the fall velocity of the rain drop. In other words, a second Fourier Transform of a time series of a spectral line of the 1. FT corresponds to the Doppler spectrum of the rain drops at the corresponding height level.

The relation between fall velocity and Doppler frequency shift is given in Equation (7.6). The MRR calculates a Doppler frequency spectrum with 64 lines whereas the resolution is $\Delta f_D = 30.52$ Hz corresponding to a resolution in fall speed v of 0.19 m/s. Thus, the MRR can resolve the fall velocity of falling particles from 0.19 m/s up to 12 m/s.

If a rain drop falls faster than the maximal resolvable fall velocity of 12 m/s, it causes an aliasing effect leading to wrong results. The same effect can happen if upward vertical winds lift rain drops. Small upward motion can appear as fast downward velocities in the Doppler spectrum.

7.2.5 Averaging

If the observed rain drops were distributed uniformly, we would not detect any phase shift between two measured spectra. But rain is a stochastic process and is never uniformly distributed. Thus, it is possible to measure the fall velocity distribution by considering the phase shift between two spectra.

But as rain is a stochastic process, a calculated Doppler spectrum gives stochastic information. To solve this problem, we have to calculate a large number of Doppler spectra and average over them. The MRR measures about 150 spectra during 6 seconds. Then it computes the average of these spectra and transmits the result. The transmission takes about 4 seconds and thus, the MRR provides an averaged spectrum every 10 seconds.

7.3 Determining the Rain Parameters

7.3.1 Radar Equation

As result of the 2^{nd} FT we get the received spectral power $dP(h, f_D)$ as a function of height h and of the Doppler frequency f_D. This received power is proportional to the reflectivity of all rain drops in the backscattering volume within the Doppler frequency resolution. We can use the radar equation (see Equation 3.8) to write

$$dP(h, f_D) = C(h)\,\frac{1}{h^2}\,\eta(f_D)\,\Delta h\,\Delta f_D \tag{7.8}$$

where $C(h)$ is a calibration function containing radar specific parameters as the transmit power, the antenna gain, the wavelength and other parameters of the MRR. $\eta(f_D)$ is the backscattering cross section per volume and per unit Doppler frequency (the spectral reflectivity density). h is the height above the MRR and f_D is the Doppler frequency shift.

In Equation (7.8) all parameters are known except $\eta(f_D)$. Thus, we can solve this equation for $\eta(f_D)$.

7.3.2 Drop Size Distribution

From Equation (7.8) we know the spectral reflectivity density $\eta(f_D)$ as function of the Doppler frequency f_D and height h. And from Chapter 5 we know the relation between the drop size and the fall velocity. As given in Equation (5.2).

Note that the fall velocity is equal to the Doppler velocity only if the ambient air has no vertical motion. At precipitation situations this is never the case but at some situation the vertical motion is small and it can be neglected.

The fall velocity must be corrected by a factor according to the environmental pressure. Equation (5.3) already gave a possibility to describe this correction factor. Here we use the correction $\delta v(h)$ as function of height assuming US Standard Atmosphere conditions.

$$\delta v(h) = 1 + 3.68 \cdot 10^{-5}\, h + 1.71 \cdot 10^{-9}\, h^2 \tag{7.9}$$

where h is given in meter above sea level.

To get the spectral reflectivity density as a function of the drop diameter D, we can use the Equation (7.6) and (5.2) to get

$$\eta(D) = \eta(f_D)\, \frac{df_D}{dv}\, \frac{dv}{dD} = \eta(f_D)\, \frac{2}{\lambda}\, 6.18\, e^{-0.6\, D[\mathrm{mm}]})\, \delta v(h) \tag{7.10}$$

Dividing the spectral reflectivity density $\eta(D)$ by the backscattering cross section $\sigma_b(D)$ of a single rain drop yields the drop size distribution $N(D)$, the number of drops per volume and diameter:

$$N(D) = \frac{\eta(D)}{\sigma_b(D)} \tag{7.11}$$

For small drops we can use the Rayleigh approximation to calculate the backscattering cross section $\sigma_b(D)$ (with use of the backscattering efficiency Q_b according to Equation (2.23)).

$$\sigma_{b,R}(D) = \frac{D^2\, \pi}{4}\, Q_b(D) = \frac{\pi^5}{\lambda^4}\, \left|\frac{\varepsilon - 1}{\varepsilon + 2}\right|^2\, D^6 = \frac{\pi^5}{\lambda^4}\, |K|^2\, D^6 \tag{7.12}$$

where ε is the complex dielectric constant of water. $|K|^2$ for water is about 0.92 at 24 GHz (for ice: $|K|^2 = 0.27$).

Unfortunately the Rayleigh approximation is not applicable in our case and we have to use the Mie theory. Thus, as correction factor we use the ratio between the Mie cross section $\sigma_{b,Mie}$ to the Rayleigh cross section $\sigma_{b,R}$ as function of the diameter D as shown in Figure 7.4.

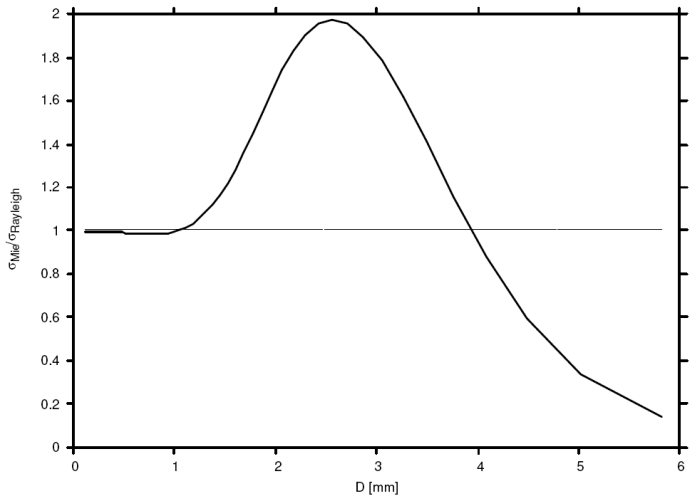

Figure 7.4: Ratio between Mie and Rayleigh backscattering cross section at 24 GHz as a function of the drop size diameter (figure taken from [15]).

7.3.3 Radar Reflectivity Factor

The radar reflectivity factor is defined according to Equation (3.11) as

$$Z = \int_0^\infty N(D)\, D^6\, dD \tag{7.13}$$

where Z is the radar reflectivity factor, D is the drop diameter and $N(D)$ the drop size distribution.

This definition is based on Rayleigh theory and Z is independent of the wavelength and the height. It depends only on the diameter and the drop size distribution.

7.3.4 Rain Rate

The rain rate R is equal to the volume of all rain drops multiplied with their fall velocities $v(D)$.

$$R = \frac{\pi}{6} \int_0^\infty N(D)\, D^3\, v(D)\, dD \tag{7.14}$$

7.3.5 Liquid Water Content (LWC)

The liquid water content LWC is the volume of all rain drops multiplied with the density of water ρ_w per volume.

$$LWC = \rho_w \frac{\pi}{6} \int_0^\infty N(D)\, D^3\, dD \tag{7.15}$$

7.3.6 Characteristic Fall Velocity

The characteristic fall velocity of a drop size distribution is defined according to Equation (5.4).

$$V_m = \frac{\int_0^\infty N(D)\, D^6\, v(D)\, dD}{\int_0^\infty N(D)\, D^6\, dD} \tag{7.16}$$

V_m is the characteristic fall velocity.

7.4 Example of MRR Data

Figure 7.5 shows MRR data measured on September 13, 2008. On this day, it was raining during three main periods. The first rain period was from 3:00 to 5:00 UT, the second from 8:00 to 11:00 UT and the third from 17:00 to 22:00 UT.

Figures (a) and (b) show a time-height plot of the radar reflectivity and the fall velocity, respectively. A rain sequence from the first rain period (from 03:00 to 04:40) is shown. The time is plotted on the horizontal axis and the height is plotted from 0 to 1600 m over the MRR level on the vertical axis.

At the beginning of the plotted sequence, it was not raining. Thus, the small (dark blue) radar reflectivity Z and fall velocity W values. Then, the rain started and intensified until the end of the displayed time period. In Figure (a), we see some vertical streams with intense rain (red). These rain streaks are tilted because the rain signal needs some time to reach the ground. In Figure (b), similar vertical regions with large fall velocity can be seen. Thus, intense rain falls faster than weak rain.

In Figure (c), the cumulative rain over the whole day is shown. The measurement of the MRR (blue) corresponds to the ground-based rain sensors (green). The three main rain periods of that day can be clearly seen. The blue line is drawn by integrating the rain rate of the 100 m height level.

7.5 Technical Summary

Table 7.1 summarizes the technical data of the Micro Rain Radar.

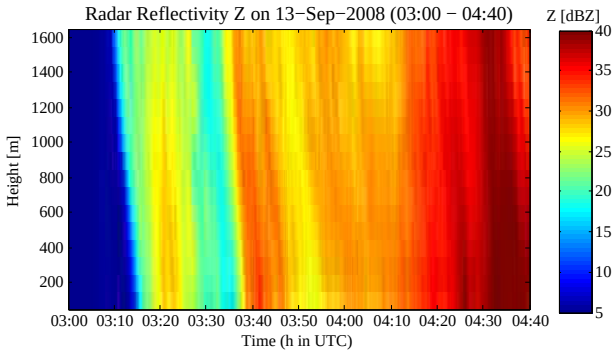

(a)

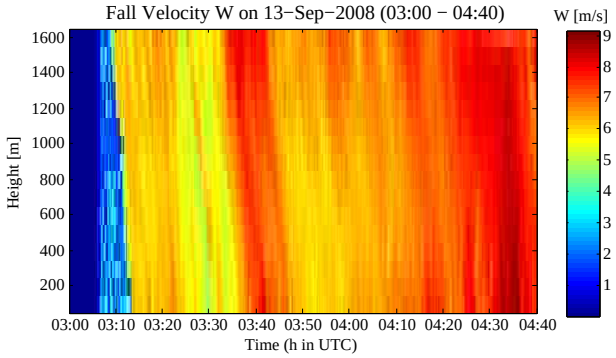

(b)

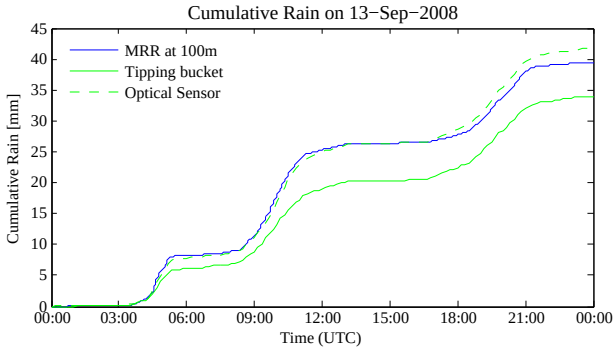

(c)

Figure 7.5: MRR measurements on September 13, 2008. Figure (a) shows a time-height plot of the radar reflectivity from 03:00 to 04:40. In Figure (b) the fall velocity is shown during the same time period. The cumulative rain measured by the MRR (blue) is compared with rain measurements by ground based rain sensors (green solid for the tipping sensor and green dashed for the optical sensor).

Table 7.1: Technical specification. The bold numbers indicate the configured values for the MRR on the roof of the ExWi building.

Property	**Value**
Transmit frequency	24.1 GHz (wavelength $\approx$ 1.24 cm)
Transmit power	50 mW
Antenna (transmit and receive)	parabolic dish (diameter 0.6 m)
Beam width (3 dB)	2°
Modulation	FM-CW
Time resolution	10 s
Height resolution	35 - 200 m (**100/50 m**)
Height range	30 levels, up to 30 $\times$ height resolution (**100 - 3000 m / 50 - 1500 m**)
Fall velocity	0.19 - 12 m/s (64 lines with 0.19 m/s resolution) correspond to a Doppler spectrum with $\Delta f_D = 30.52$ Hz resolution
Bandwidth B	750 KHz - 4.29 MHz (**1.5/3.0 MHz**)
Sweep period T	256 μs
Power supply	24 VDC / 25 W
Weight	12 kg
Dimensions (without socket)	0.6 m $\times$ 0.6 m $\times$ 0.6 m

Chapter 8

Stratiform Precipitation

Vertical motion of the air masses influences the measurement of the fall velocity (as we have already pointed out in Chapter 7). For that reason, we consider events with stratiform precipitation only, where the vertical air motion is small.

8.1 Characteristics of Stratiform Precipitation

Figure 8.1 shows the measured radar reflectivity (a) and the fall velocity (b) on July 13, 2008 between 02:20 and 03:30. The horizontal axis shows the time, and the vertical axis shows the height above the instrument.

Considering the Figure of the radar reflectivity (a), the regions with strong rain are colored from orange to red and the regions with weak rain from yellow to blue. Dark blue means that there is no or almost no rain. The intensity of the rain is changing with time. There are periods with strong rain and periods with weak rain. Considering a region of intense rain, we see that the structure is tilted with height. Thus, a period of intense rain starts in an upper region and needs some time to reach the ground. We can get a rough approximation of the fall velocity by considering this tilt.

A layer with very high radar reflectivity can be identified at about 2000 m height. Due to its high intensity, this layer is called *bright band*. It is the layer where snow melts and transforms to rain. We consider the processes of this melting layer in detail in the next chapter.

Above the bright band, the radar reflectivity is smaller than below. The reason for this is, that the radar reflectivity of snow is small because ice is almost invisible to microwave radiation.

On the right hand side of Figure 8.1, we see the characteristic fall velocity. Orange to red indicate large values of the fall velocities and yellow to blue small values, respectively.

At 2000 m height, we see a border between two regions. Above 2000 m the fall velocity is small (in the range of about 1 to 2 m/s) and below 2000 m it is much larger. The reason for this behavior is obvious, the fall velocity of snow is significantly lower than the fall velocity of rain. This borderline between snow and rain corresponds to

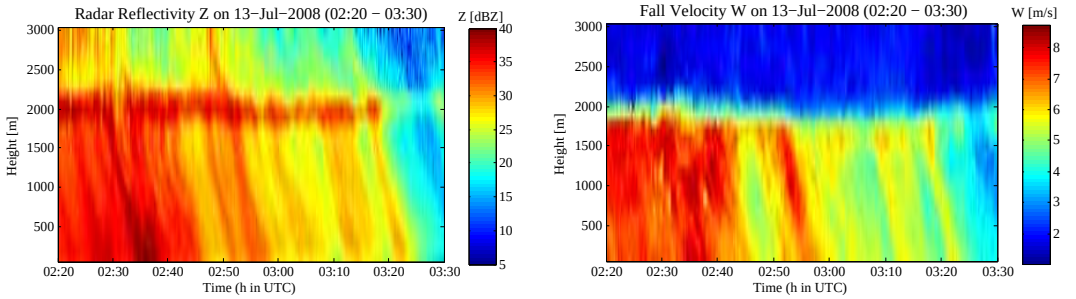

(a) (b)

Figure 8.1: Radar reflectivity and fall velocity on July 13, 2008 starting at 2:20. A rain sequence with duration of 70 minutes is shown. The radar reflectivity is shown in Figure (a), the fall velocity in Figure (b).

the bright band.

Below the bright band height, the structure of the variations of the fall velocity corresponds to the structures seen in the radar reflectivity plot. This confirms the relation that intense rain has a larger fall velocity than weak rain.

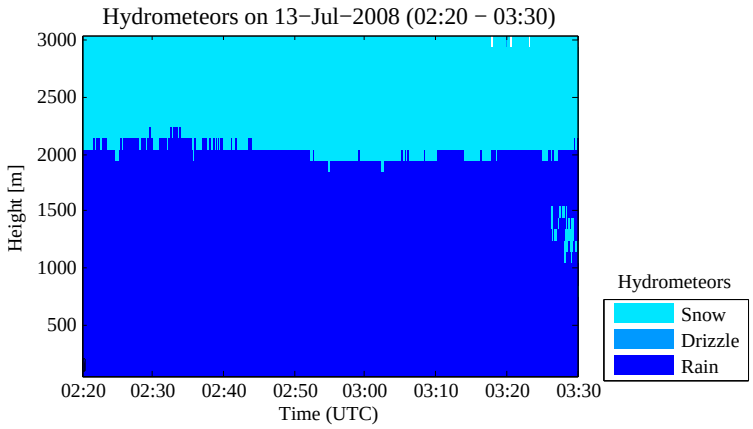

Figure 8.2: Type of hydrometeor of the precipitation on July 13, 2008 (from 2:20 to 3:30).

We know that rain and snow show a specific signature of radar reflectivity and fall velocity values (as summarized in Figure 5.2). Using this information, we can take the details given in Figure 8.1 and we can categorize each data point to a specific type of hydrometeor. The result is shown in Figure 8.2. The result is not surprising, we see the clear line between snow and rain.

8.1.1 Frequency Analysis

Now, we compare the measurements of the MRR and TROWARA. But we have to be aware that the MRR measures straight upward (with a beam angle of 2°) and TROWARA measures with at a zenith angle of 50°. Typically we consider precipitation at levels up to 3000 m. At this height, the distance between the measured volume of the MRR and TROWARA is about 3500 m.

As we have seen, the intensity of a precipitation event is changing with time and thus the horizontal extent of an event is limited. The questions now are: what is a typical extent of a rain structure? and is it feasible to compare the measurements of the two instruments?

We are looking at stratiform precipitation with a typical horizontal extent of a few tens to hundreds of km. We have seen that such an event contains periods with intense and weak rain. Thus, there are substructures within the precipitation event.

To get information about the horizontal extent of the variations in a stratiform precipitation event, we analyze the frequency spectrum of the radar reflectivity at a height level.

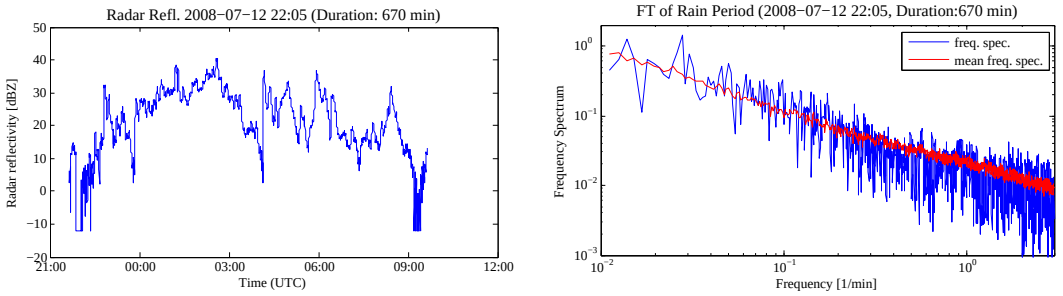

(a) (b)

Figure 8.3: Frequency analysis of the rain event on July 12, 2008 starting at 22:05 with a duration of 670 minutes. On the left side, we see the time series of the radar reflectivity. On the right side, we see the corresponding frequency spectrum (blue). We investigated 30 rain events and averaged the spectra. The averaged spectrum is shown in red.

In Figure 8.3, we see an example of the radar reflectivity of a long rain period (a) as a function of time. On the right side (b), we see the corresponding frequency spectrum (blue). We analyzed the frequency spectrum of 30 rain events (A list of the analyzed rain events is given in Table C.1 in Appendix C). The average spectrum of these events is shown in the same figure by the red line.

We see that the most characteristic frequencies occurring in long rain periods have values smaller than 0.1 min^{-1}. Thus, the most dominating periods during long rain events are in the order of hours.

And as we can see from the time series in Figure 8.3, the change from one rain structure to another can be abrupt (e.g. the strong increase of the radar reflectivity at

about 4:00 occurred within 2 minutes.).

During a stratiform precipitation event, the horizontal wind is slow, on the order of about 1 m/s. Thus, during a time period of 10 minutes the rain structure moves on the order of 0.6 km, and 3.6 km during an hour. Thus, the dominating structures have a horizontal extent in the order of about 3.6 km.

Thus, we can conclude that in general the MRR and TROWARA measure the same rain structure. But structures exists that are smaller than the distance between the observed volumes of the two instruments. And the change from one structure to the other can be abrupt.

8.2 Estimation of the Rain Rate

8.2.1 Rain Estimation by the MRR

To compare the estimated rain from the MRR and TROWARA, we use three ground-based sensors. Two of them are located on the roof of the ExWi building, and one sensor is located at the weather station Bollwerk. The Bollwerk sensor and one of the ExWi sensors are tipping buckets with a time resolution of 10 minutes. The second sensor on the ExWi roof is an optical rain sensor. It is very sensitive to snow and overestimates the precipitation rate during snow periods.

In Figure 8.4 we compare the measurement of the cumulated rain of the MRR (using the rain rate values at the 100 m height level) with the two ground-based sensors on the ExWi roof. The accordance between the three curves is good.

The MRR is able to estimate rain with a high accuracy. During wet snow events the rain rate is overestimated and the cumulative rain is too large.

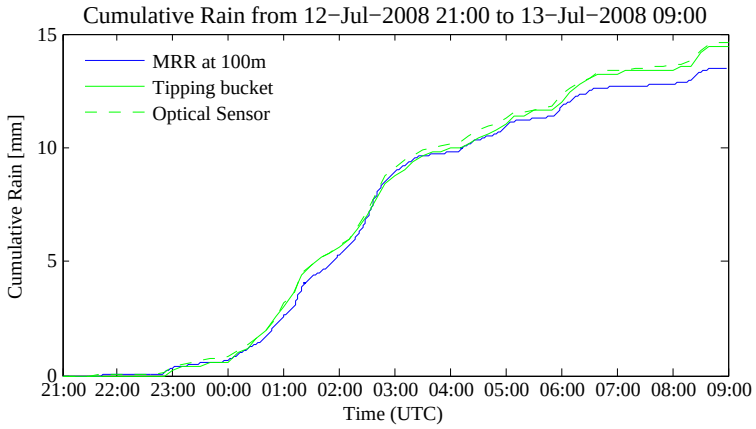

Figure 8.4: Cumulated rain between July 12, 2008 21:00 and July 13, 2008, 9:00. Measured with the MRR (blue), the tipping bucket (green) and the optical sensor (green dashed).

8.2.2 Rain Estimation by the TROWARA

Figure 8.5 shows the rain estimated by the TROWARA algorithm described in Section 6.3.3 compared with the rain measurements of the two ExWi rain sensors. If we compare the results, we see that the rain estimated by TROWARA is overestimated.

The algorithm needs the lapserate to calculate the depth of the rain layer. The lapserate can be determined by analyzing the vertical profiles measured by the MRR. Figure 8.6 shows the height of the melting layer (red line). How this can be done is explained in Chapter 9.5. The green curve shows the height of the melting layer estimated by the surface temperature using a constant lapserate of 6 K/km. We see that the red curve is below the green one, and thus the lapserate is larger than 6 K/km and should be set to an averaged value of 6.5 K/km. At the beginning of the time series the lapserate is smaller (6.25 K/km) and at the end larger (6.7 K/km).

The TROWARA algorithm uses the parameter β, which can be determined only if cloud free periods are found. In the selected time series this was not the case. Thus, β was set to the statistical mean value. The real value for β can be significantly different from the one we used.

Another fact not considered is the influence of the melting layer. Due to the large emittance of the melting layer, the TROWARA algorithm overestimates the opacity of the rain and thus the rain rate. In Chapter 10, we describe a model to calculate the influence of the melting layer. We will see if the rain estimation by the TROWARA algorithm can be improved.

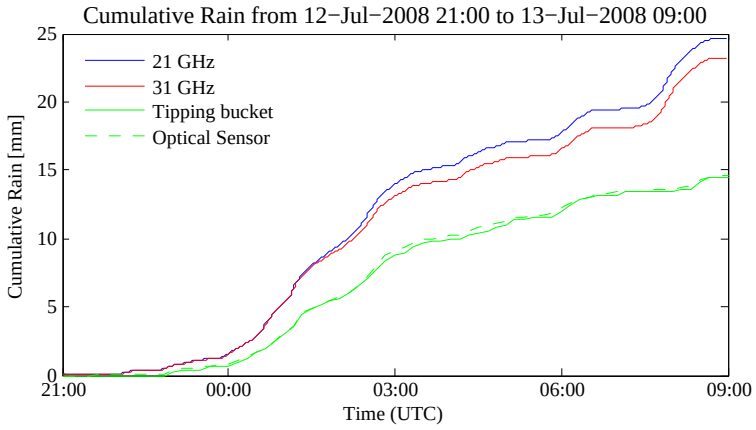

Figure 8.5: TROWARA rain estimation (blue for 21 and red for 31 GHz) compared with the ExWi sensors (green and green dashed). The lapserate was set to 6.5 K/km and the threshold of the ILW level was set to 0.35 mm.

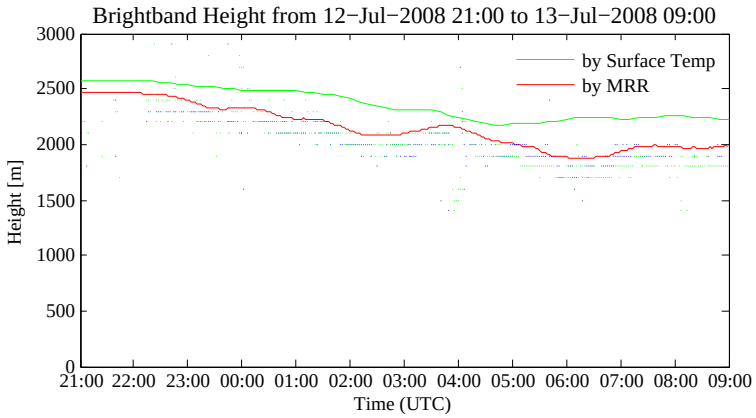

Figure 8.6: Height of the upper boundary of the melting layer. The red curve shows the height of the melting layer estimated from MRR data. The green curve is the estimated height of the melting layer estimated from surface temperature assuming a constant lapserate of 6 K/km. The blue and green dots are an indication of the reliability of the red curve and are explained in the next chapter.

Chapter 9

The Melting Layer

The melting layer has a significant influence to the radiation received at the ground. We analyze the vertical profiles of the radar reflectivity and the fall velocity through the melting layer.

9.1 Radar Reflectivity and Fall Velocity Profiles

Using the data collected by the MRR, various parameters can be extracted from the vertical profiles of the radar reflectivity and the fall velocity. An example of an averaged reflectivity and fall velocity profile is shown in Figure 9.1.

First, we consider the profile of the equivalent radar reflectivity Z_e on the left side of Figure 9.1. The upper region (1500 to 1100 m) is associated with ice and snow particles. They are almost invisible for microwave radiation and therefore the radar reflectivity is small. According to the measurements of F. Fabry [4], the radar reflectivity of snow decreases by 6 to 7 dB km^{-1} in the first kilometer above the melting layer. Our measurements made by MRR show an almost constant reflectivity above the melting layer. The MRR is considering the absorption of the radiation through the rain. The absorption could be overestimated in the melting layer leading to an overestimation of Z_e above.

The increase in the radar reflectivity at level 1100 m and below is associated with melting (see Fabry [4]). A couple of effects may contribute to the enhanced radar reflectivity: the change in the dielectric constant, the change in the fall velocity, precipitation growth, the change in the particle size distribution (aggregation and breakup), the combined effect on echo power of the shape and orientation of melting hydrometeors, and the effect of the distribution of the water within the melting snowflake.

If the amount of the liquid water exceeds a certain level, the snowflake collapses and the diameter gets smaller leading to a smaller backscattering cross section. We can see this effect at levels at about 700 to 800 m. Below 700 m the snow is melted and falls to the ground as rain. It is possible that some ice pieces are still contained in the liquid water. But the aerodynamic and radiative properties are almost the same as for a completely melted rain drop. The radar reflectivity below 700 m is constant

as the rain is constant within this layer.

Considering the plot on the right side of Figure 9.1, we see the characteristic fall velocity. At the top, the fall velocity is low (between 1 and 1.5 m/s). This velocity corresponds to the fall velocity of snow. Within the melting layer, we see an increase of the fall velocity. In the upper region of the melting layer (900 to 1100 m), the fall velocity stays constant because the shape of the snowflakes does not change yet. At lower levels, the shape of the snowflakes becomes different due to the increasing amount of liquid water. The snowflakes speed up and reach their full speed at the bottom of the melting layer, when they are transformed to rain drops. The fall velocity stays constant below the melting layer and the velocity values lie in a range between 5 and 7 m/s.

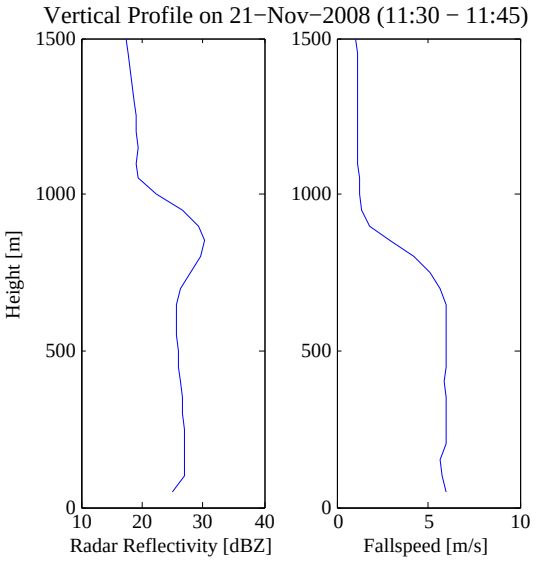

Figure 9.1: Typical vertical profile of the radar reflectivity (plot on the left side) and the fall velocity (right side). The profiles were measured on November 21, 2008.

The shape of the discussed profile is typical for stratiform rain. For situations with convective rain, we cannot define such a clear profile.

9.1.1 Model Function

To analyze the melting layer systematically, we approximated the vertical profiles of the radar reflectivity and the fall velocity by simple empirical model functions. The model function for the radar reflectivity profile is characterized by 6 parameters and the the fall velocity profile by 4 parameters, respectively.

Model for Radar Reflectivity Profile

The model function of the radar reflectivity can be seen in the left plot of Figure 9.2. It is characterized by 6 parameters and can be expressed as

$$Z_e(h) = \begin{cases} Z_s & h \geq H_R + D_Z \\ (Z_{max} - Z_s)\frac{1+\cos(\varphi_2(h))}{2} + Z_s & H_R + D_{Z,1} \leq h < H_R + D_Z \\ (Z_{max} - Z_r)\frac{1-\cos(\varphi_1(h))}{2} + Z_r & H_R < h < H_R + D_{Z,1} \\ Z_r & h \leq H_R \end{cases} . \quad (9.1)$$

The phase functions φ_1 and φ_2 are given as

$$\begin{aligned} \varphi_1(h) &= \frac{(h-H_R)\,\pi}{D_{Z,1}} \\ \varphi_2(h) &= \frac{(h-H_R-D_{Z,1})\,\pi}{D_{Z,2}} \end{aligned} \quad . \quad (9.2)$$

Thus, the modeled radar reflectivity Z_e (expressed in dBZ) is a function of the height h. The shape is determined by six parameters: The reflectivity of the snow Z_s, the reflectivity of rain Z_r and the maximal reflectivity within the melting layer Z_{max}. The lower end of the melting layer is determined by H_R and the depth of the melting layer can be divided into two parts, the lower part below the maximal reflectivity $D_{Z,1}$ and the upper part $D_{Z,2}$ respectively. The total depth of the melting layer is given by $D_Z = D_{Z,1} + D_{Z,2}$. Note that all radar reflectivity values must be inserted in dBZ.

Model for Fall Velocity Profile

The model of the fall velocity is simpler than the model of the radar reflectivity. It is characterized by 4 parameters. The shape of the model function is shown in the right plot in Figure 9.2.

The mathematical expression of this model profile is given by

$$V(h) = \begin{cases} V_s & h \geq H_{FV} + D_{FV} \\ (V_s - V_r)\frac{h-H_{FV}}{D_{FV}} + V_r & H_{FV} < h < H_{FV} + D_{FV} \\ V_r & h \leq H_{FV} \end{cases} . \quad (9.3)$$

Thus, the profile of the fall velocity V is a function of the height h. It is characterized by four parameters: The fall velocity of snow V_s above the melting layer and the fall velocity of the rain V_r below, respectively. The bottom height H_{FV} of the melting layer and the depth D_{FV} of the layer where the particles speed up, are the other parameters defining the profile.

Approximation

The measured profiles are fitted by the model function by minimizing the variance of the difference between the model and the measured profile.

Figure 9.3 shows two examples of measured profiles approximated by their modeled profiles.

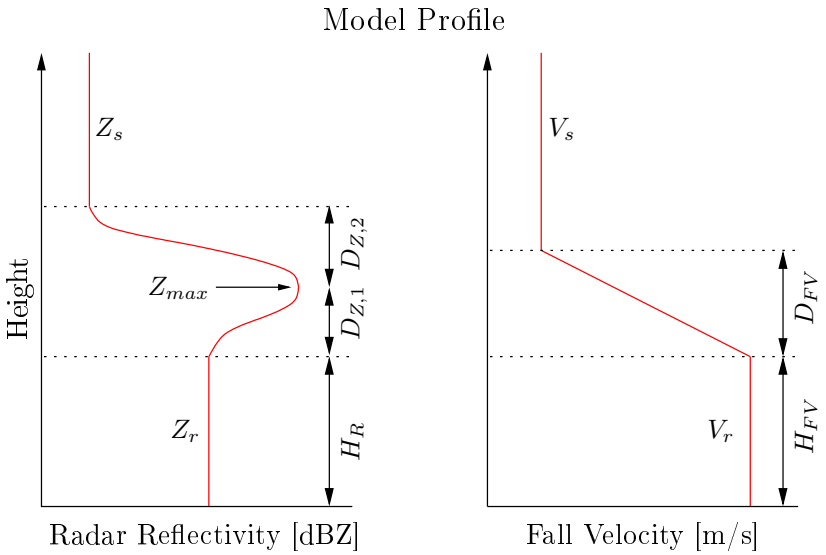

Figure 9.2: Model function of the vertical profile of the radar reflectivity (left) and the fall velocity (right).

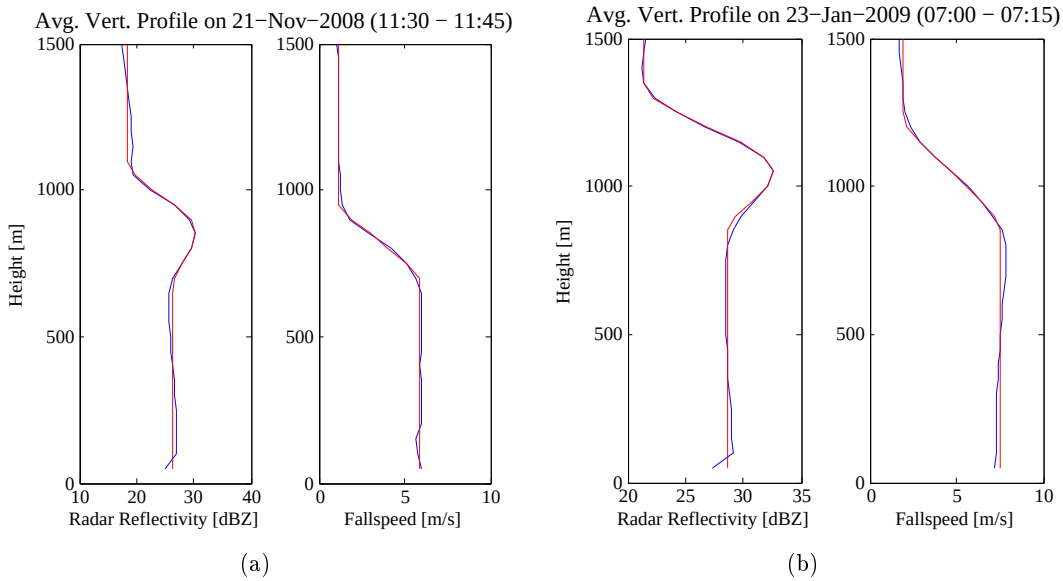

Figure 9.3: Example of the approximation of the vertical profiles by the model function. The blue curve shows the vertical profile of the radar reflectivity and the fall velocity on November 21, 2008 (a) and January 23, 2009 (b). The red curves show the profiles approximated by the model function.

9.2 Estimating the Depth of the Melting Layer

During the observed measurement period, we selected about 90 rain events with a stable melting layer. For every event, the vertical profiles are approximated by the described model function and the parameters are determined. A list of the dates and times of these events is given in Table C.2 in Appendix C.

Using measurements from the ground-based weather station, we tried to find a correlation between the depth of the melting layer and a parameter at the ground.

A couple of such relations is shown in Figure 9.4. Figure (a) shows a scatter plot between the rain rate measured at the ground and the depth of the melting layer (parameter D_Z). The depth D_{FV}, where the fall velocity is increasing, can be measured with higher accuracy than the depth D_Z. Thus, Figure (b) shows the relation between the rain rate and D_{FV}.

The ambient air can influence the depth of the melting layer as well. Thus, Figure (c) and (d) show a scatter plot between the lapserate below the melting layer and the depth D_Z and D_{FV}.

Figure 9.5 shows another scatter plot between the rain rate measured at the ground and the depth of the melting layer (D_{FV}). This time, the rain rate was measured by the optical sensor with a time resolution of one minute.

The results of all the scatter plots are disappointing. No clear relation can be seen. We expected an increasing depth of the melting layer (either D_Z or D_{FV}) with increasing rain rate. The influence of the lapserate was expected as follows: If the lapserate is large, the increase of the temperature difference between the melting snowflake and the ambient air would be large within the same falling distance. Thus, the snowflake melts within a smaller distance. But the scatter plots cannot confirm this behavior.

9.3 Melting Layer Statistics

Figure 9.6 shows correlations of some selected melting layer parameters. In Figure (a), we see that the height of the melting layer estimated by the radar reflectivity profile (H_R) corresponds very well to the height estimated by the fall velocity profile (H_{FV}).

Figure (b) relates the radar reflectivity of rain (Z_r) to the fall velocity of rain (V_r). The radar signature of rain shown in Figure 5.2 can be confirmed.

Figures (c) and (d) show scatter plots of the radar reflectivity of rain (Z_r) to the maximal radar reflectivity (Z_{max}) and to radar reflectivity of snow (Z_s). The maximal radar reflectivity (Z_{max}) is usually between 4 dBZ and 8 dBZ above the radar reflectivity of rain (Z_r). And the radar reflectivity of snow (Z_s) is between 2 dBZ and 10 dBZ below Z_r.

Figure (e) shows a scatter plot of the depth of melting layer estimated by the radar reflectivity profile (parameter D_Z) and by the fall velocity profile (parameter D_{FV}). No clear relation is visible.

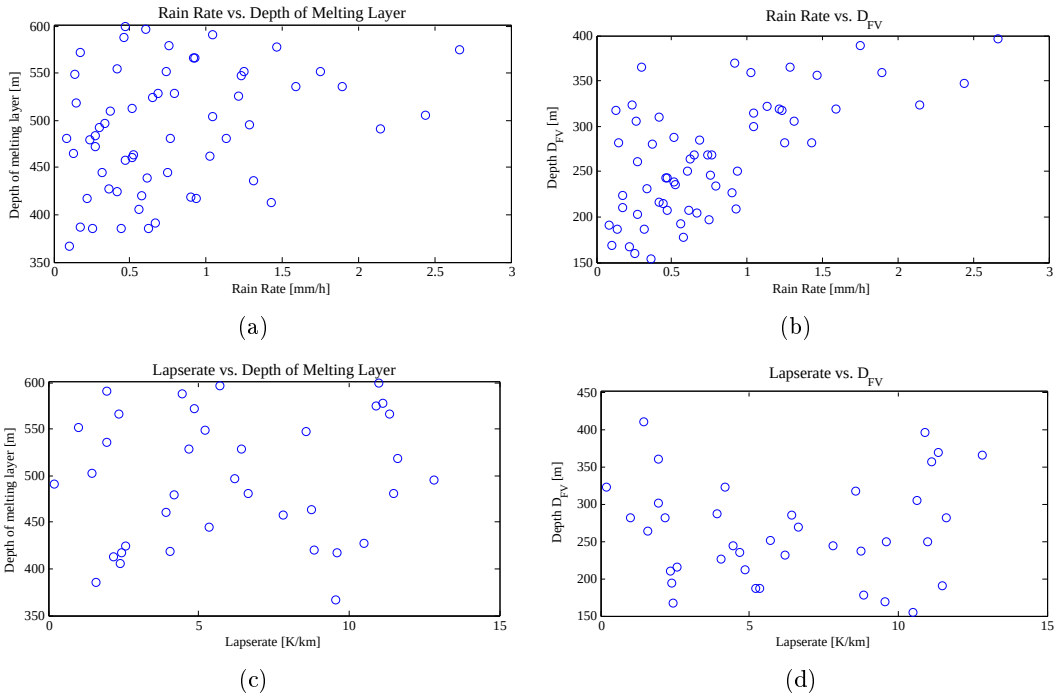

Figure 9.4: Relation between depth of the melting layer and the rain rate or the lapserate, respectively.

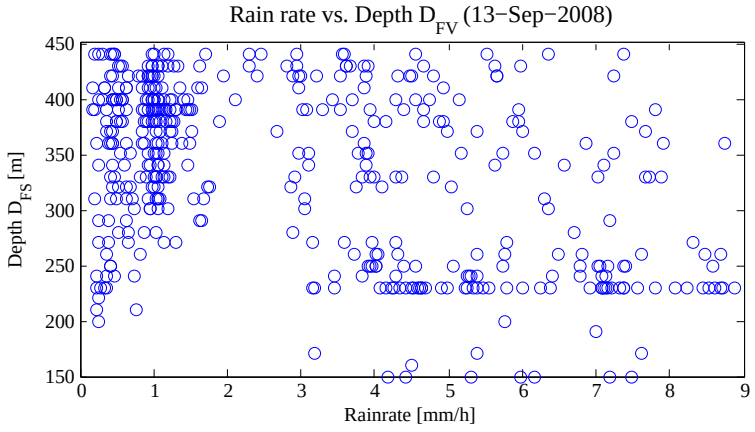

Figure 9.5: Correlation of the rain rate measured at the ground and the depth of the melting layer (D_{FV}). Measured for the 10 hours rain period on September 13, 2008.

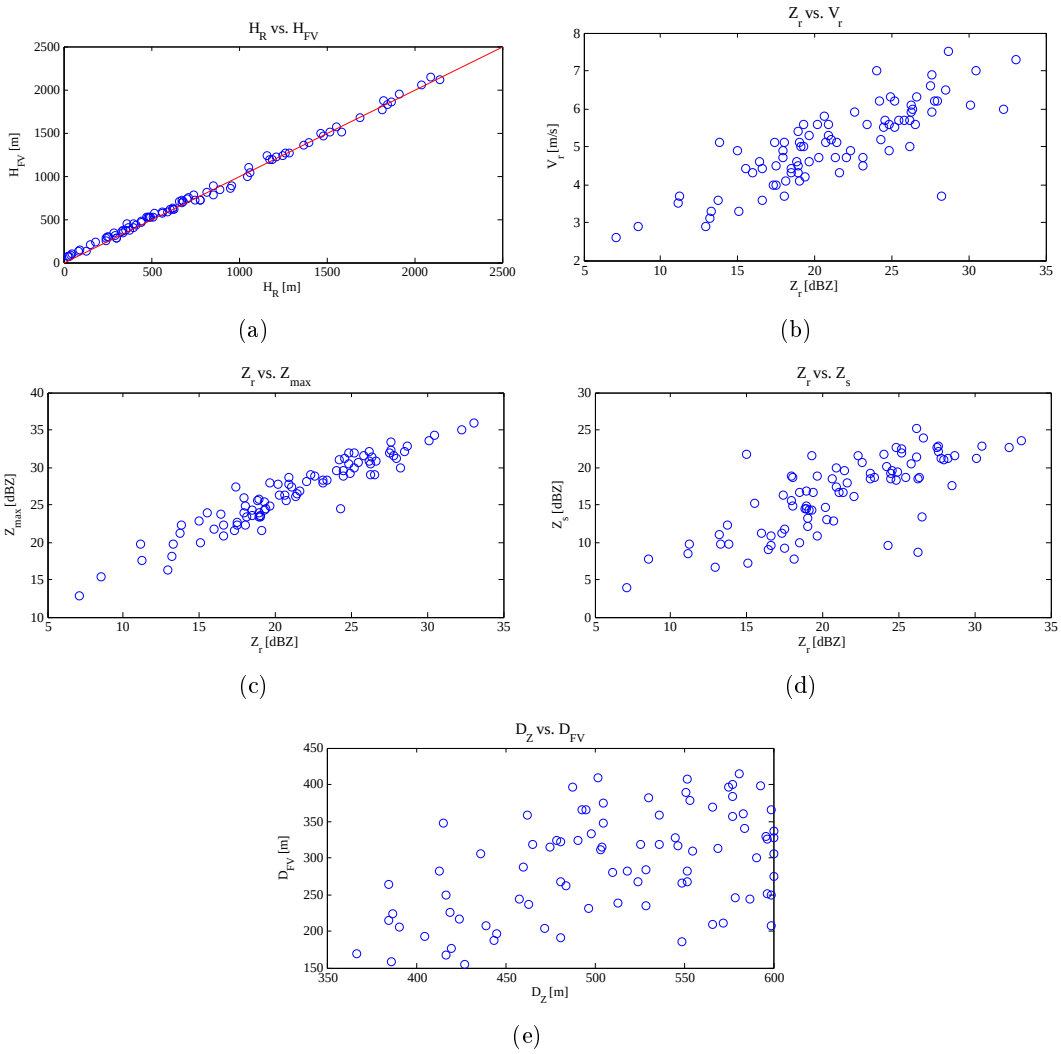

Figure 9.6: Melting layer statistics. Figure (a) shows the correlation between the height of melting layer estimated by the radar reflectivity profile (parameter H_R) and by the fall velocity profile (parameter H_{FV}). Figure (b) correlates the radar reflectivity of rain (Z_r) with the fall velocity of rain (V_r). Figure (c) correlates the radar reflectivity of rain (Z_r) with the maximal radar reflectivity (Z_{max}). Figure (d) compares the radar reflectivity of rain (Z_r) with the radar reflectivity of snow (Z_s). And Figure (e) correlates the depth of the melting layer estimated by the radar reflectivity profile ($D_{Z,1} + D_{Z,2}$) and by the fall velocity profile (D_{FV}).

9.4 Temperature Profile

Another interesting aspect is the temperature profile in the melting layer. The temperature difference between the environmental air and the melting snowflakes (0°) determines the amount of energy that can be used by the melting process.

To analyze the temperature profile in a melting layer, we searched radiosonde profiles raising through rain. The closest radiosondes are launched in Payerne. Figure 9.7 shows a radiosonde profile raised through rain.

The temperature is shown by the blue line and the dew point temperature by the red line. The dashed lines indicate the borders of the melting layer. This information is taken from the rain radar measurement in Bern. Thus, it is possible that there are differences between the precipitation layers of Bern and Payerne.

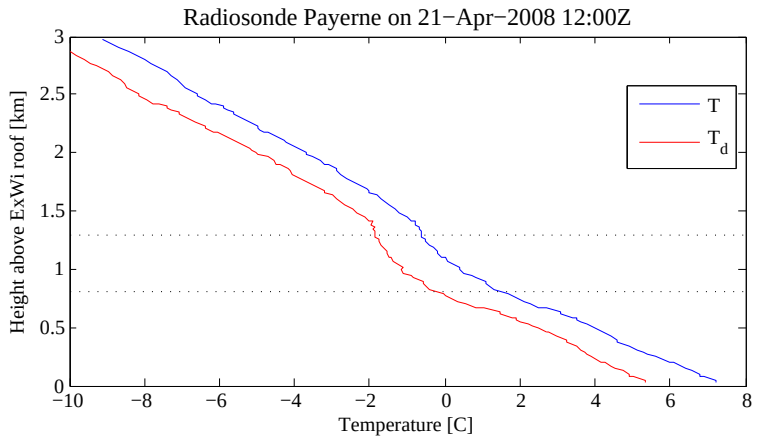

Figure 9.7: Temperature profile measured by a radiosonde launched in Payerne on the April 21, 2008 at about 12:00. The radiosonde raised through rain. The temperature is shown in blue and the dew point in red, respectively. The dotted lines show the upper and lower border of the melting layer.

Considering the temperature curve in Figure 9.7, we see a constant temperature decrease above and below the melting layer. The lapserate above the melting layer is about 5.5 K/km and below about 7.2 K/km.

The lapserate at the top of the melting layer is very small. The air in the upper part of the melting layer spends all the energy to the melting ice.

We note that the 0°C temperature height lies below the upper border of the melting layer. This cannot be true, ice cannot melt at temperatures below 0°C. Other radiosonde profiles through rain show the same behavior. Either the upper limit of the melting layer is not correct or the temperature sensor is influenced by the rain. Thus, we cannot be sure about the accuracy of temperature soundings through rain.

9.5 Estimating the Height of the Melting Layer

The TROWARA algorithm estimating the rain (see Section 6.3.3) needs to know the depth of the rain layer. A constant lapserate is assumed and the 0°C temperature height is estimated by the surface temperature. Using the MRR we have the possibility to determine the 0°C temperature height by analyzing the vertical profiles of the radar reflectivity and the fall velocity.

In the previous considerations we assumed that the vertical profiles correspond to the model function discussed in Section 9.1.1. But unfortunately the reflectivity and fall speed profiles are not always that clear. As an example, we plot a number of vertical radar reflectivity and fall velocity profiles in Figure 9.8. Every curve corresponds to an averaged profile over one minute. In Figure (a), 15 vertical profiles are shown within the time period between 13:00 and 13:15. We see, that all profiles correspond to the expected shape. So we do not have any problem to estimate the height of the melting layer. This is different in the following time period, Figure (b) shows the next 15 profiles (from 13:15 to 13:30). It is obvious that it is more difficult to retrieve the melting layer height.

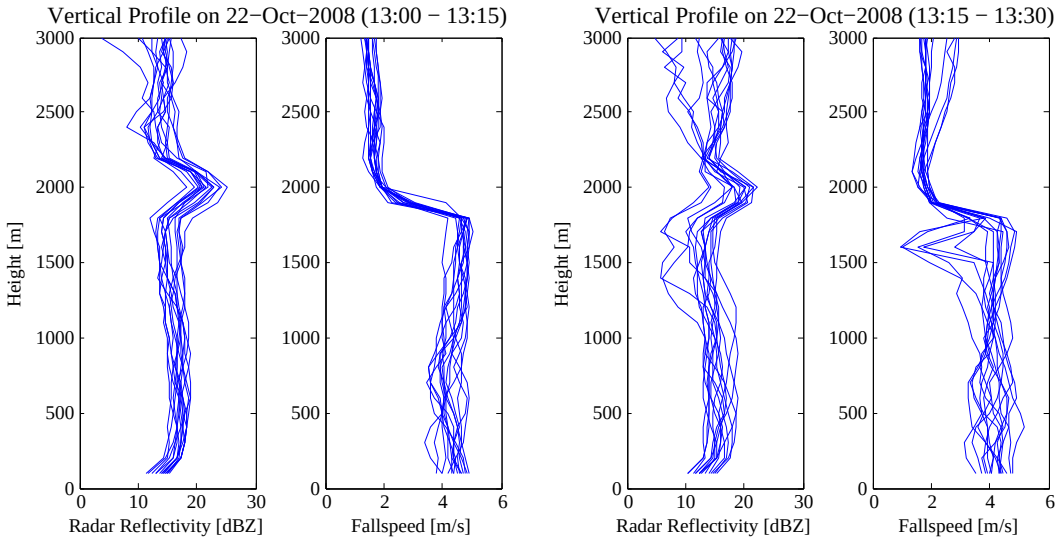

Figure 9.8: Figures (a) shows 15 consecutive profiles of the radar reflectivity (left) and the fall speed (right) as a function of height on October 22, 2008 from 13:00 to 13:15. Figure (b) shows the same but 15 minutes later.

9.5.1 Problems associated with Defining an Algorithm

Here we describe an algorithm developed to determine the height of the melting layer. As example we used the data from October 22, 2008. Figure 9.9 shows the different

types of hydrometeors on that day between 12:00 and 18:00. Using the radar reflectivity and fall velocity measurements of the MRR, each sample can be categorized to a hydrometeor regime (with use of Figure 5.2). The border between snow and rain can be clearly recognized in this figure. But we also can see many non realistic rain to snow transitions (small regions of snow in the rain areas or vice versa). These are caused by noise and outliers in the radar data. It is complicated for the algorithm to filter out the noise and the outliers.

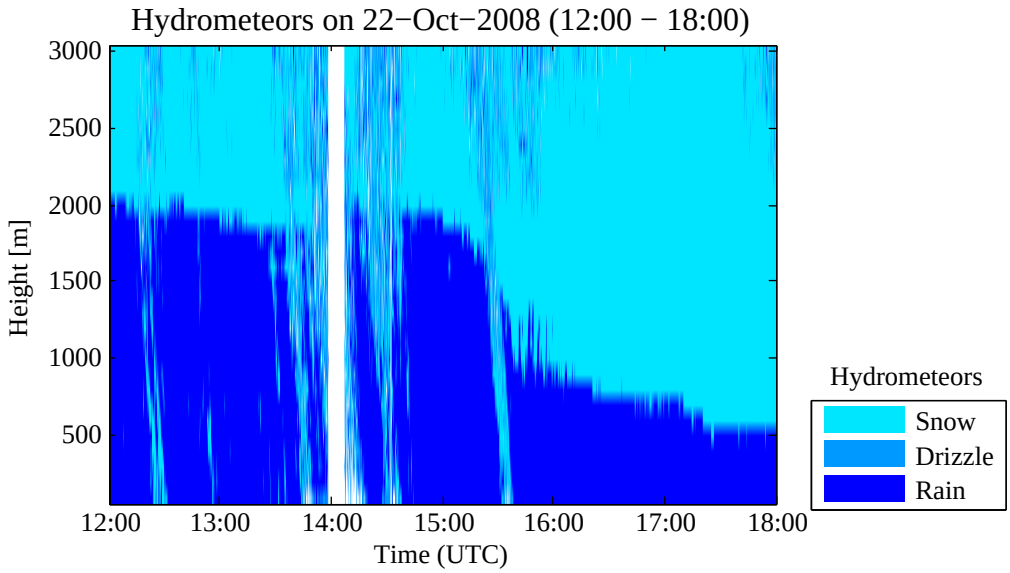

Figure 9.9: Different types of hydrometeors. The border between rain and snow can clearly be seen.

Our algorithm is based on the two main characteristics of the melting layer, the enhanced radar reflectivity and the increase of the fall velocity in the melting layer.

Figure 9.10 shows the result of the algorithm, the red line. The green line shows the estimated height of the melting layer using the surface temperature and assuming a constant lapserate of 6°C /km. We see, that the two curves differ significantly. Comparing the graph of the Figure 9.9 with Figure 9.10, we observe that the red curve is closer to the real height of the melting layer than the green one. And we conclude, that the estimation of the height of the melting layer is not very accurate just using the surface temperature.

The algorithm is based on the heights of the maxima of the radar reflectivity for every averaged vertical profile. In Figure 9.10 each of this maximum is denoted by a small blue dot. The second criterion is the increase of the fall velocity within a certain height for every vertical profile. These events are denoted by small green dots. If we look at these blue and green dots in Figure 9.10, we see that accumulation of these

dots corresponds to the height of the melting layer, but we see many of these dots far from the red line.

To conclude, the difficulty to determine the height of the melting layer was not to find a good criterion but to filter out the outliers. Now, we give the recipe how we designed the algorithm to filter out the outliers.

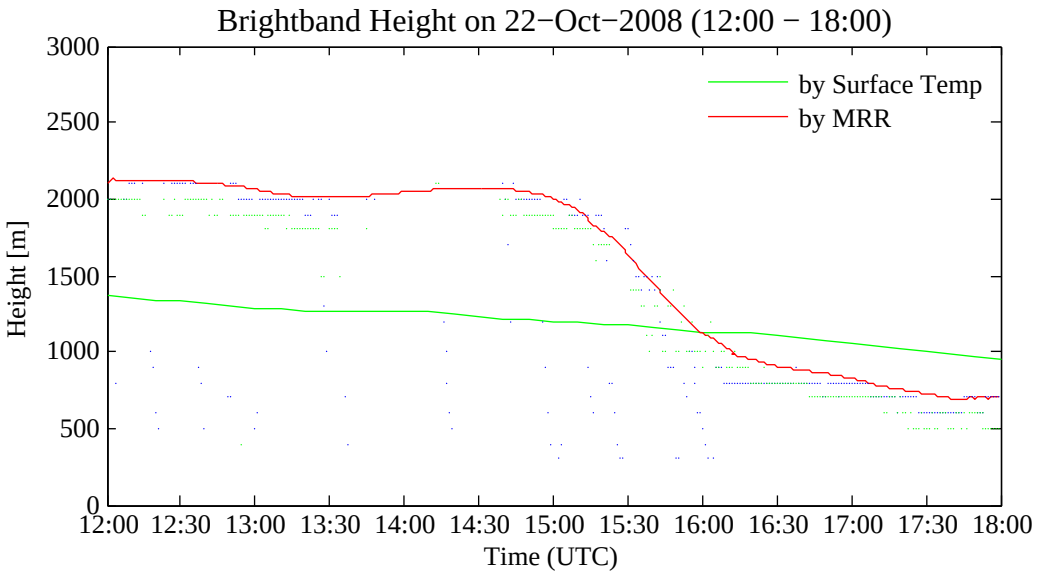

Figure 9.10: The red line shows the estimated melting layer height according to the described algorithm. The green line is the estimation using the surface temperature assuming a constant lapserate (6 K/km).

Recipe to determine the height of the melting layer:

1. Averaging: The time resolution between two vertical profiles is 10 s. To reduce the noise in this data, we calculate the mean value of 6 profiles.

2. Process data only during rain periods. The criteria for rain are the following: First, the radar reflectivity must be at least 5 dBZ at least at one level. Secondly, there must be at least 3 consecutive samples with a radar reflectivity larger than 5 dBZ.

3. Find the maxima of the radar reflectivity: For every profile, the maximum of the radar reflectivity and its height are determined.

4. Increase of the fall velocity: For every profile, the height level where the fall speed rises above 2.5 m/s is determined (starting from the top).

5. The height levels obtained from the reflectivity and the fall speed criteria must lie at about the same height. Thus, samples are rejected, if the difference between the height levels are larger than 300 m.

6. Calculation of the height of the melting layer. The height of the melting layer is calculated as the mean of the heights of the two criteria.

7. Remove outliers: 10 consecutive samples of the melting layer height are taken and the median is determined. All heights must lie within an interval of 200 m to the median height, otherwise the samples are rejected.

8. Smooth. The resulting curve is smoothed.

Chapter 10

Radiative Model of the Melting Layer

To estimate the influence of the melting layer to the received radiation at a radiometer, we introduce a radiative model of the melting layer. The goal of this radiative model is to estimate the emission of the radiation within the microwave frequency range. As measurable output value, the opacity is calculated.

Some simplifications were necessary to describe the model, e.g. aggregation and breakups within the melting layer are not considered and the depth of the melting layer is assumed to be constant (it is set to 500 m).

There are many possibilities to model the melting layer. F. Fabry presented six other approaches (for further details see [3]).

10.1 Model of a Melting Snowflake

10.1.1 Model

A melting snowflake consists of a mixture of water and ice surrounded by air. As the flat shape of a snowflake is difficult to model, we approximate it by a sphere. The snowflake consists of air, ice crystals and water inclusions inside the sphere. We assume that the water inclusions have the shape of ellipsoids as described in the discussion about wet snow (Section 4.10). Figure 10.1 shows a schematic picture of such a snowflake.

The volume of the snowflake ($V_{snowflake}$) is given by the sum of the volumes of each of the three components.

$$V_{snowflake} = V_{air} + V_{ice} + V_{liquid} \tag{10.1}$$

We define the volume fraction f_v as ratio of the volumetric water (liquid and ice) to the total volume.

$$f_v = \frac{V_{ice} + V_{liquid}}{V_{snowflake}} \tag{10.2}$$

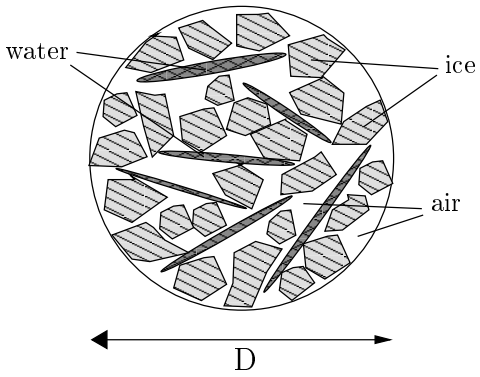

Figure 10.1: Model of a snowflake.

The liquid water content w is defined as ratio between the liquid and total water volume.

$$w = \frac{V_{liquid}}{V_{ice} + V_{liquid}} \tag{10.3}$$

Thus, we can derive the formula for the volume of each component.

$$V_{air} = (1 - f_v)\, V_{snowflake} \tag{10.4}$$

$$V_{ice} = f_v\,(1 - w)\, V_{snowflake} \tag{10.5}$$

$$V_{liquid} = f_v\, w\, V_{snowflake} \tag{10.6}$$

We assume that the total mass of the ice and liquid water in the snowball is conserved. With the assumption that the density of ice and of liquid water are equal ($\rho_{ice} \approx \rho_{liquid}$), the sum of V_{ice} and V_{liquid} is conserved.

We define the diameter D_0 as the diameter of the completely melted snowflake ($f_v = 1$, $w = 1$). Thus,

$$\frac{\pi}{6}\, {D_0}^3 = V_{ice} + V_{liquid} = V_{liquid}(f_v = 1, w = 1) \quad . \tag{10.7}$$

Then, we define the diameter D_{SF} as the diameter of a spherical snowflake with inserted air.

$$D_{SF}(f_v) = D_0\; f_v^{-1/3} \tag{10.8}$$

The dielectric constant of a snowflake can be calculated using the formula of the dielectric constant of wet snow (Equation (4.15)). The amount of the volumetric liquid water content in this formula is equal to the product $w \cdot f_v$. The temperature to calculate the dielectric constant of water and ice is 0°C. We assume that the inclusions of liquid water in the snowflake are prolate ellipsoids (look like small needles). Thus, we set the depolarization factors of the ellipsoids to $A_1 \approx 0.01$ and $A_2 = A_3 = (1 - A_1)/2$.

10.1.2 Simplifications and Assumptions

Now we critically discuss the simplifications and assumptions made in the model above.

Snowflake as a Sphere

It is obvious that the assumption to model a snowflake as a sphere does not represent the reality. We use this assumption to calculate the Mie efficiency for the absorption. The Mie theory can handle spheres only. A more realistic approach would be to model a snowflake as a flat ellipsoid.

Liquid Water in the Snowflake

We assume that the shapes of the liquid water intrusions in the snowflake are thin, long ellipsoids. We took this assumption from observations of wet snow (see [13]) on the ground. It is only valid, if the liquid water content is small.

The shapes of the liquid water inclusions are used to calculate the dielectric constant of the snowflakes. We can say that the dielectric constant of a dry snowflake is close to the one of air. If the snowflake is almost melted, the dielectric constant must be close to the dielectric constant of water. Our model fulfills these conditions.

The shape factor of the ellipsoids play an important role in the model. It determines the relaxation frequency of the wet snow. This property can be used to validate our model.

Dielectric Constant of the Melting Snowflake

We use Equation (4.15) to calculate the dielectric constant of a snowflake. This formula is only valid for small amounts of liquid water. In our model, the amount of liquid water exceeds this limit. When the snowflake is completely melted, it has the dielectric constant of water. But if the amount of liquid water is in between these two ranges, we do not know the correct value.

In the undefined range, we approximate the dielectric constant of wet snow by a polynomial of third order of the parameter $x = w \cdot f_v$. We find the coefficients for this polynomial by the following four conditions. (a) For $x = 0.05$, the dielectric constant of wet snow ε_{WS} is equal to the value given by Equation (4.15). (b) The slope at $x = 0.05$ is equal to the slope at this value in Equation (4.15). (c) For $x = 1$, ε_{WS} is equal to the dielectric constant of pure water and (d) the slope at $x = 1$ is zero. Figure 10.2 shows the result using the polynomial interpolation according to the described conditions.

Density of Water Equal to Density of Ice

We assumed that the density of liquid water ρ_{liquid} is equal to the density of ice ρ_{ice}. This is certainly not true. The density of liquid water is about $1000\,\mathrm{kg/m^3}$ and the density of ice is about $917\,\mathrm{kg/m^3}$. The difference is about 10% but in relation to the uncertainties and assumptions described above, the effect of the wrong density is negligible.

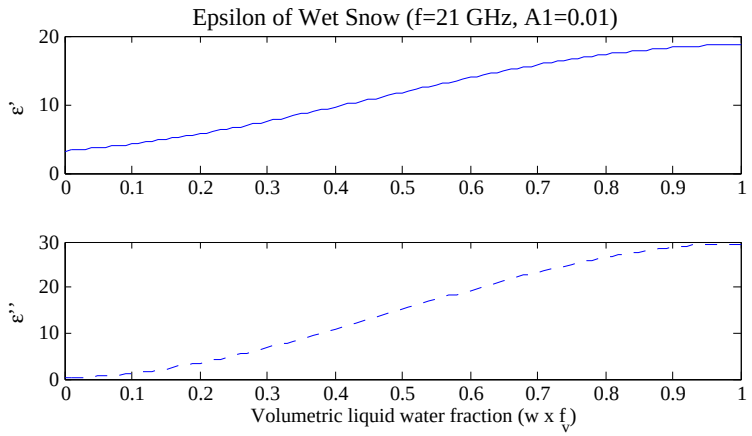

Figure 10.2: Approximation of the dielectric constant of wet snow as function of the volumetric liquid water fraction ($w \cdot f_v$). The depolarization factor A_1 was set to 0.01.

10.2 Emission of the Snowflake Distribution

10.2.1 Emission

Knowing the dielectric constant of every snowflake, we can calculate the emission. We assume, that each snowflake falling in the melting layer at the top comes out as a rain drop at the bottom of the melting layer. Thus, we assume that no aggregation and no breakup takes place in the melting layer.

Below the melting layer, we can assume that the rain drops follow a Marshall-Palmer drop size distribution (see (5.1)). Thus, the distribution of the snowflakes follows a Marshall-Palmer distribution as well. But due to the different fall velocities of snowflakes and rain drops, we have to use a correction factor determined by the fall velocity.

The distribution of the size of snowflakes N_{SF} is given as

$$N_{SF}(D_0, f, R) = N_{SF}(D_{SF}, R) = N_{MP}(D_0, R)\,\frac{v_{rain}(D_0)}{v_{snow}(D_0, f_v)} \tag{10.9}$$

where D_{SF} is the diameter and D_0 the equivalent diameter of the snowflake, f_v is the volume fraction, R the corresponding rain rate and v_{rain} is the fall velocity of rain drop according Equation (5.2). N_{MP} is the Marshall-Palmer drop size distribution. The fall velocity of the snowflakes v_{snow} is assumed to be independent of the drop size, but changes with the amount of liquid water.

Using the dielectric constant of wet snow, we can calculate the Mie efficiency Q_{abs} for the absorption according Equation (2.26). Using the Mie efficiency Q_{abs} and the drop size distribution, we can calculate the absorption coefficient γ_{abs} according to Equation (2.32).

$$\gamma_{abs} = \frac{\pi}{4} \int_0^\infty D_{SF}^2 \, Q_{abs}(D_{SF}) \, N_{SF}(D_{SF}, R) \, dD_{SF} \tag{10.10}$$

Integrating the absorption coefficient over the depth of the melting layer, we get the opacity of the melting layer (see Equation (2.30)). We set the depth of the melting layer to a constant value of 500 m.

10.2.2 Simplifications and Assumptions

As well as for the model of a snowflake, we made some assumptions calculating the emission of melting snow.

No Aggregation and Breakup within the Melting Layer

In the upper region of the melting layer, an enhanced activity of aggregation can be observed (see [2]). Whereas in the lower region breakups of the melting snowflakes occur. But the number of snowflakes at the top and at the bottom of the melting layer is about the same.

All Snowflakes Melt within the Same Distance

A small snowflake is melted before reaching the bottom of the melting layer, while a large snowflake still contains ice particles reaching the bottom of the melting layer. Our model does not account for this effect, but it could be adapted by considering the sizes of the snowflakes.

Snowflakes Follow a Marshall-Palmer Drop Size Distribution

If we assume that no aggregation or breakups occur in the melting layer, it is logical that the drop size distribution stays the same (corrected by a factor depending on the fall velocity). It would also be possible to use another drop size distribution as the Marshall-Palmer distribution.

Fall Velocity of the Snowflakes is Constant

The fall velocity of snowflakes not only depends on the size, but also on the shape. And the shapes of snowflakes are manifold.

Our measurements of the fall velocity of snow show that the variation of the fall velocity is not that pronounced as the variation of the fall velocity of rain drops is.

The Depth of the Melting Layer is Constant

In Section 9.2 we tried to find a possibility to estimate the depth of the melting layer. We did not find a relation to estimate the depth of the melting layer. It turned out, that the depth of the melting layer can be different for a given rain rate. Thus, we

assume that the depth of the melting layer is equal to 500 m independent of the rain rate.

10.3 Characteristics of the Melting Layer

We described the calculation of the opacity of the melting layer but we did not discuss the change of some parameters within the melting layer. The fall velocity of the snowflakes is increasing from top to bottom. The volume fraction changes as the snowflake collapses with increasing liquid water content. And the amount of liquid water is increasing. The consequences for the melting layer emission will be considered here.

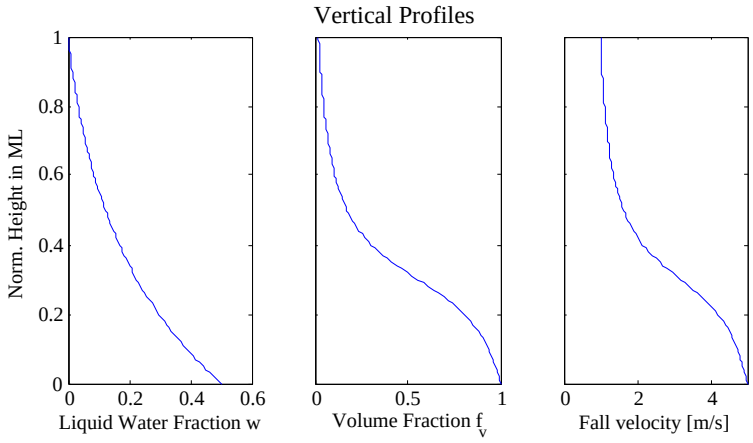

Figure 10.3: Liquid water fraction, volume fraction and fall velocity as function of height within the melting layer. The vertical axis represents the normalized height in the melting layer (0: bottom, 1: top of ML).

10.3.1 Liquid Water Fraction w

The liquid water fraction at the top of the melting layer is zero. At the bottom of the melting layer, the ice skeleton of a snowflake is broken and the amount of liquid water is that large, that the remaining ice pieces "swim" in the liquid water and form a sphere. The shape and the radiative properties of this mixture of water and ice are almost the same as of a sphere consisting of liquid water. Thus, the liquid water fraction at the bottom of the melting layer is smaller than one. We assume that it is in the order of about 0.5.

At the top of the melting layer, the liquid water fraction increases very slowly, because the environmental temperature is just slightly above 0°C. Thus, there is not much energy available to melt the ice. Deeper in the melting layer the temperature difference to 0°C is larger and the ice melts faster. We assume an exponential increase

of the liquid water fraction within the melting layer, as shown in the left plot of Figure 10.3.

10.3.2 Volume fraction f_v

The volume fraction of dry snow is about 0.02 (as shown by measurements of snow packs by [12]). For melted snow, the volume fraction is 1. Thus, we set the volume fraction to 0.02 at the upper and to 1 at the lower end of the melting layer. In between we assumed a S-shape (approximated by an arc-tan function). The plot in the middle of Figure 10.3 shows how we have chosen the characteristics of the volume fraction.

10.3.3 Fall Velocity v_{snow}

At the upper end of the melting layer, the snowflakes consist of dry ice and a large amount of air. Thus, the fall velocity v_{snow} is small. The deeper the snowflakes fall into the melting layer the larger becomes the amount of liquid water. The shape of a flake changes towards a sphere. Like the characteristics of the volume fraction we approximated the fall velocity characteristic by an arc-tan function.

The plot on the right side of Figure 10.3 shows the characteristics of the fall velocity in the melting snow. This shape corresponds to the measurements made by the MRR.

10.4 Model Results

10.4.1 Absorption Coefficient of the Melting Layer

Using Equation (10.10) with the characteristics described in Section 10.3, we calculate the absorption coefficient of the wet snow in the melting layer. The result is shown in Figure 10.4. Considering the plot from top to bottom, we see that the absorption coefficient increases from almost zero up to a maximum in the middle of the melting layer. Then it decreases again to the absorption coefficient of rain. This shape corresponds to the expected shape considering the characteristics of the radar reflectivity.

10.4.2 Opacity of the Melting Layer

Integrating the absorption coefficient over the melting layer, we get the opacity. Figure 10.5 shows the opacity as function of the rain rate. The depth of the melting layer was set to 500 m.

We see that the opacity increases linearly with the rain rate. Thus, the opacity can be written as

$$\tau_{ML,21} = g_{ML,21} \cdot R \tag{10.11}$$

$$\tau_{ML,31} = g_{ML,31} \cdot R \tag{10.12}$$

where $\tau_{ML,21}$ and $\tau_{ML,31}$ represent the opacity of the melting layer at 21 and 31 GHz, respectively. R is the rain rate inserted in mm/h. $g_{ML,21}$ and $g_{ML,31}$ are the proportionality factors. It turns out that $g_{ML,21} = 0.020$ and $g_{ML,31} = 0.0280$. The

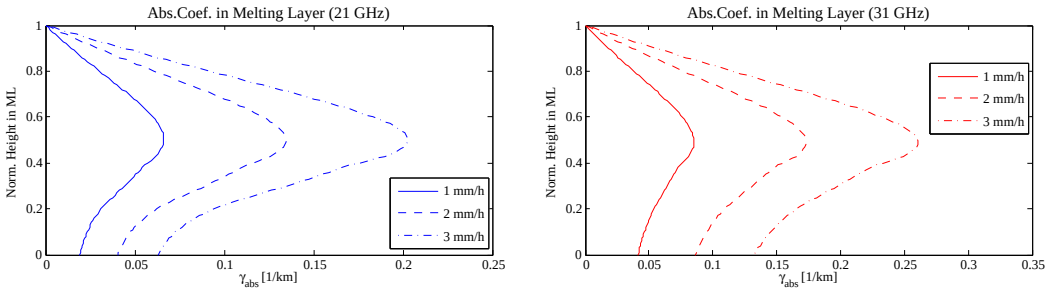

(a) (b)

Figure 10.4: Absorption coefficient within the melting layer. Modeled for 1 (solid), 2 (dashed) and 3 mm/h (dash-dotted) rain. Figure (a) shows the absorption coefficient for 21, Figure (b) for 31 GHz. The vertical axis represents the normalized height in the melting layer (0: bottom, 1: top of ML). The depolarization factor A_1 was set to 0.01.

proportionality factors $g_{ML,21}$ and $g_{ML,31}$ can be denoted as specific opacities of the melting layer, because they represent the opacity normed by the rain rate.

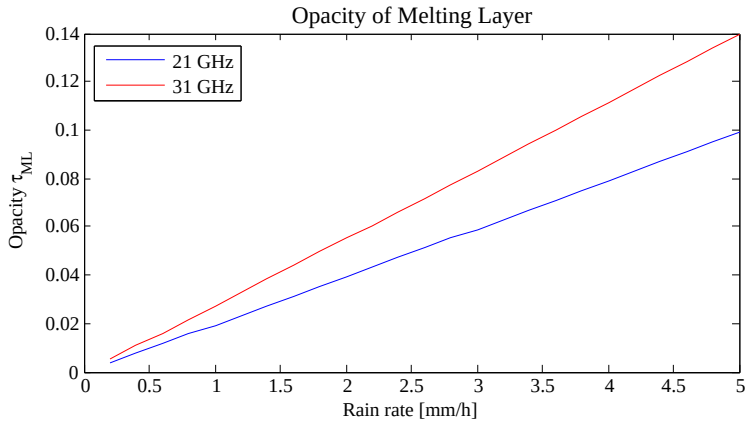

Figure 10.5: The modeled opacity of the melting layer as function of the rain rate. The blue curve shows the opacity for 21.2 GHz and the red for 31.5 GHz. The depth of the melting layer was set to 500 m and the depolarization factor A_1 to 0.01.

10.4.3 Influence of the Depolarization Factor A_1

The depolarization factor of the ellipsoids plays an important factor in the model. Due to this factor the Debye relaxation frequency of wet snow is determined. A larger A_1 leads to a higher relaxation frequency.

A change of the relaxation frequency leads to a change of the dependency of the

two measured frequency. This feature can be used to validate the model.

Figure 10.6 shows the ratio of the two absorption coefficients ($\gamma_{abs,31}/\gamma_{abs,21}$) as function of the location in the melting layer. If the amount of liquid water is large, A_1 has no effect on the absorption coefficients. In the upper part of the melting layer, an increase of A_1 leads to a increase of the ratio $\gamma_{abs,31}/\gamma_{abs,21}$.

Figure 10.7 shows the specific opacities as function of A_1. For both frequencies, the specific opacities are decreasing.

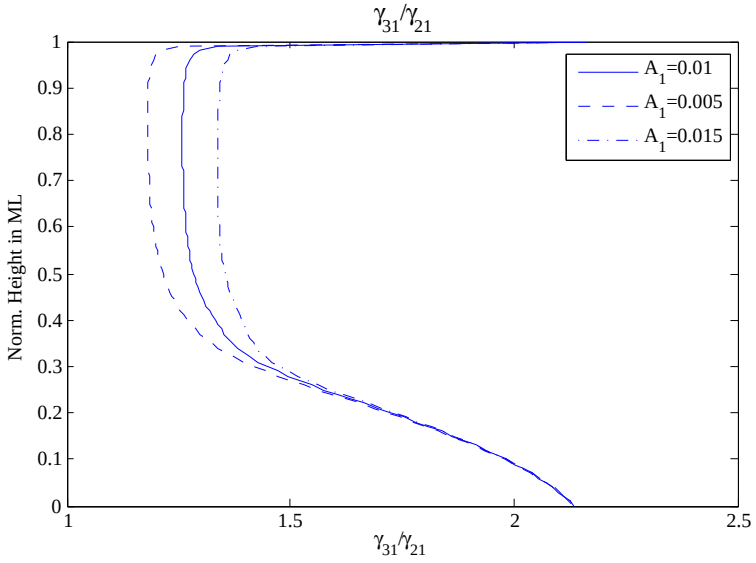

Figure 10.6: The ratio between the absorption coefficients γ_{31} and γ_{21} as function of the normalized height in the melting layer. The vertical axis represents the height in the melting layer (0: bottom, 1: top of ML). The solid line is drawn with a depolarization factor A_1 of 0.01, the dashed line with 0.005 and the dash-dotted line with 0.015.

10.5 Validation of the Model

To validate the radiative model of the melting layer, we compare the results of opacity measurements made by TROWARA for a special rain event by the model results using the rain rate measured at the ground.

10.5.1 Estimation of the Opacity of the Melting Layer

The opacity of the melting layer can be estimated in the same way as the opacity of the rain layer (see Section 6.3.3). But we consider only special cases of precipitation, where the snow is melting just before reaching the ground. Thus, there is no rain layer ($H_R = 0$). The bottom of the melting layer is just at the ground level.

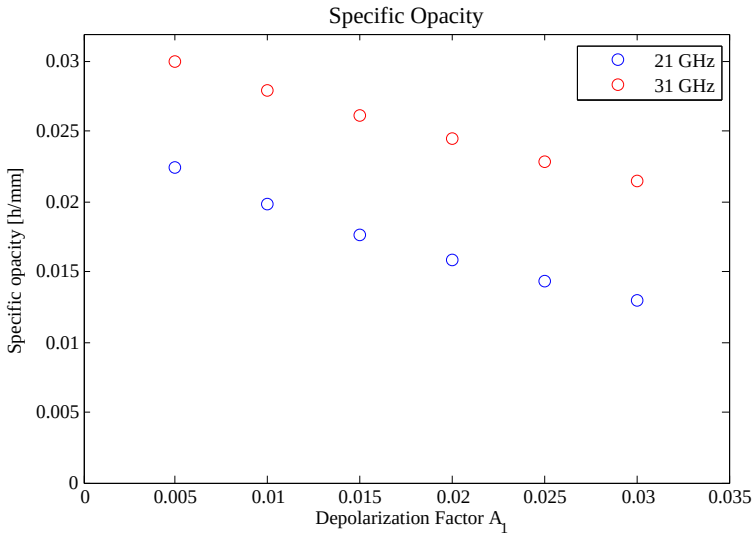

Figure 10.7: The Specific opacities as function of the depolarization factor A_1 (blue for 21 and red for 31 GHz).

In analogy to Equation (6.25) we can formulate the brightness temperature $T_{b,i}$ of the frequency i as

$$T_{b,i} = T_{b,nosnow,i}\, e^{-\tau_{ML,i}/\mu} + T_{m,ML}\,(1 - e^{-\tau_{ML,i}/\mu}) \tag{10.13}$$

where $\tau_{ML,i}$ is the opacity of the melting layer and $T_{m,ML,i}$ is the effective mean temperature of the melting layer. As snow is always melting at 0°C, the effective mean temperature has always the same temperature (independent of height) and is independent of the frequency. Thus,

$$T_{m,ML} = 273\ K \quad . \tag{10.14}$$

The background temperature $T_{b,nosnow,i}$ can be calculated in the same manner as for rain (see Equation (6.26)).

$$T_{b,nosnow,i} = T_c\, e^{-\tau_{R,i}/\mu} + T_{mi}\,(1 - e^{-\tau_{R,i}/\mu}) \tag{10.15}$$

where $\tau_{R,i}$ is the opacity when the ILW exceeds the ILW threshold level (ILW_R) and T_{mi} is the effective mean temperature of the atmosphere.

We can solve Equation (10.13) for the opacity of the melting layer:

$$\tau_{ML,i} = -\mu \ln\left(\frac{T_{m,ML} - T_{b,i}}{T_{m,ML} - T_{b,nosnow,i}}\right) \tag{10.16}$$

10.5.2 Comparison of the Measured and the Modeled Opacity

To validate the radiative model of the melting layer, we selected precipitation events where the melting layer was just above the ground. Such a situation occurred on October 29, 2008 between 0:00 and 12:00. The upper height of the melting layer is shown by the red line in the left plot of Figure 10.8. The upper height of the melting layer was at about 500 m between 0:00 and 02:00 and decreased to about 300 m where it stayed constant.

Another argument that the selected precipitation event fulfills the required conditions is shown in the right plot of Figure 10.8. The cumulative rain measured by the tipping sensor (green), by the optical sensor (green dashed) and by TROWARA (blue and red) is shown. The measurements of the optical and the tipping sensor are close together. The rain estimation of the optical sensor is slightly larger than the estimation of the tipping bucket. Thus, the snow must have been almost melted at the ground. Probably there was a small amount of ice in the larger snowflakes leading to the small overestimation of the rain. The TROWARA estimations overestimate the rain significantly. This is the case if the opacity of the melting layer is large compared to the opacity of the rain layer.

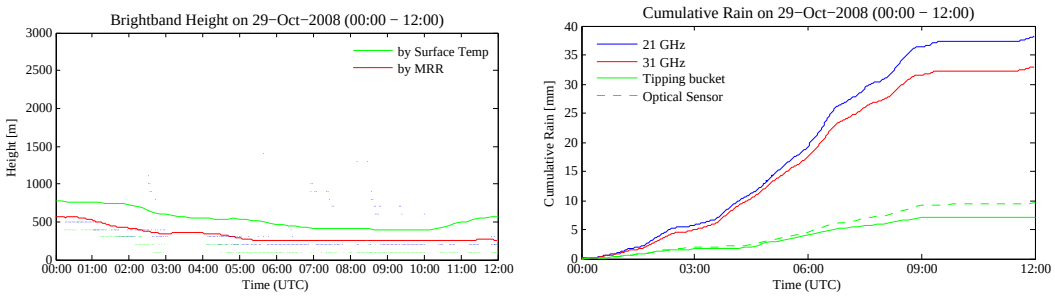

(a) (b)

Figure 10.8: The plot on the left side shows the upper height of the melting layer (red). And the plot on the right side shows the cumulative rain measured by the tipping sensor (green solid), the optical rain sensor (green dashed) and the TROWARA (blue and red).

The upper plot of Figure 10.9 shows the measurements of the melting layer opacity by TROWARA for 21.2 GHZ (blue) and 31.5 GHz (red). The lower plot shows the opacity estimated by the melting layer model. We used the rain rate measured by the optical sensor to calculate the melting layer opacity with use of the linear relation shown in Figure 10.5.

The rain rate is measured at the ground by the optical sensor with a time resolution of one sample per minute.

Comparing the two plots in Figure 10.9, we see that the magnitude of the opacities are in the same order. We recognize the basic characteristics in both plots.

The magnitudes of the changes of the opacity are much stronger for the modeled

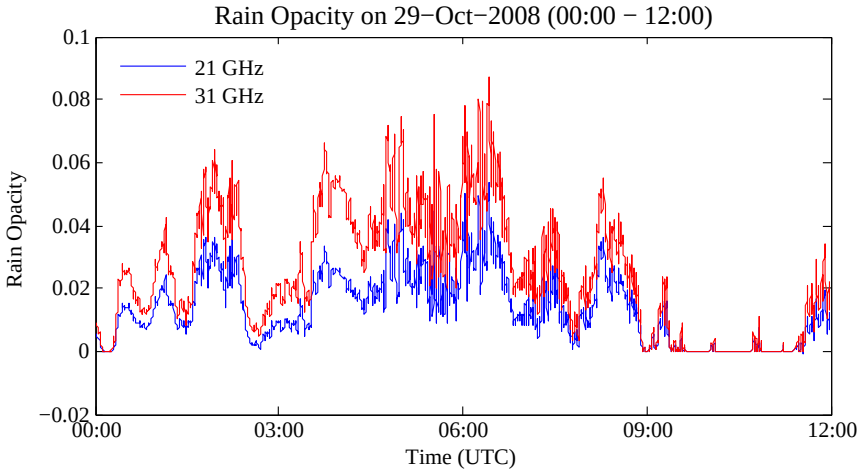

(a)

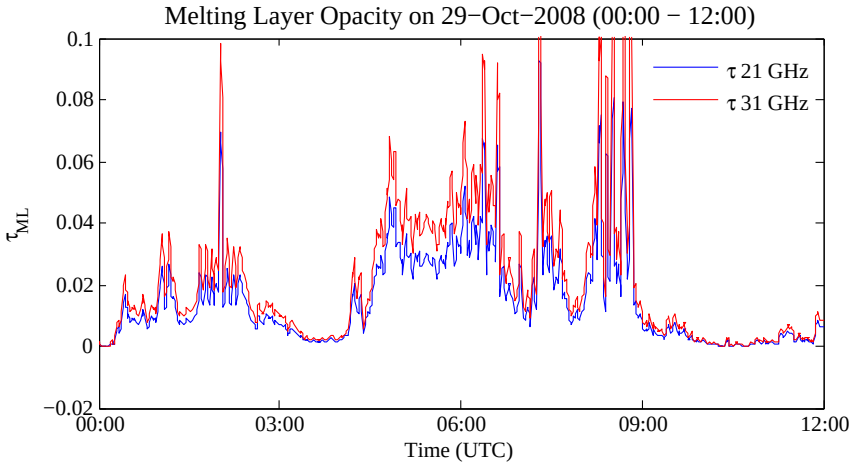

(b)

Figure 10.9: The upper figure shows the opacity measured by TROWARA at 21 (blue) and 31 GHz (red). The lower figure shows the same opacity, estimated by the melting layer model ($A_1 = 0.01$) with use of the rain rate, smoothed over 3 minutes.

opacity and correspond to the changes of the rain rate at the ground. The opacity measurement by TROWARA is influenced by the whole melting layer. Thus, the changes of the opacity values are smaller.

The high peaks of the opacity in the lower plot could be caused by an overestimation of the rain rate. The optical sensor is very sensitive to snow and it is possible that a few not completely melted snowflakes reached the ground.

At about 3:00, the TROWARA opacities increased meanwhile the modeled opacities decreased. A reason for this behavior could be, that the TROWARA instrument did not measure the same rain event as the optical rain sensor due to the displacement of the sensors.

10.6 Estimation of the Rain Rate using the ML Opacity

In Section 6.3.3 we presented a method to estimate the rain rate from the rain opacity without considering the opacity of the melting layer.

Here we present a method to estimate the rain rate including the opacity of the melting layer. We assume that the opacity $\tau_{rain,i}$ calculated by Equation (6.30) corresponds to the sum of the rain and melting layer opacity.

Thus, we can write according to Equation (6.22) with use of Equation (6.21)

$$\tau_{rain,i} = H_R \cdot \gamma_{a,R,i} + \tau_{ML,i} = H_R \cdot R \cdot g_{R,i} + R \cdot g_{ML,i} \tag{10.17}$$

where $\tau_{rain,i}$ is the total opacity of the rain and the melting layer, $\gamma_{a,R,i}$ the absorption coefficient of rain, H_R the thickness of the rain layer and $\tau_{ML,i}$ the opacity of the melting layer. R is the rain rate and $g_{R,i}$ the specific rain absorption. The opacity of the melting layer $\tau_{ML,i}$ is replaced by the term from Equation (10.12).

Note, that we use the same name for the opacity of rain $\tau_{rain,i}$ as in Equation (6.22), even if it represents the opacity of rain and the melting layer.

The depth H_R of the rain layer is calculated in the same way as in Equation (6.23). With the difference that the top of rain layer is located at a temperature height of about 2.5°C. Thus,

$$H_R = \frac{T_S - 275.65}{\Gamma} \tag{10.18}$$

where Γ is the lapserate and T_S the temperature at the surface.

Equation (10.17) can be solved for the rain rate R and we get

$$R = \frac{\tau_{rain,i}}{H_R\, g_{R,i} + g_{ML,i}} \tag{10.19}$$

where $g_{ML,i}$ is the specific opacity of the melting layer opacity.

Figures 10.10 and 10.11 show two examples. On the left side of each figure, the cumulative rain without and on the right side with use of the melting layer opacity is shown.

The estimation of the rain is significantly better considering the influence of the melting layer opacity.

In Appendix D, a collection of further precipitation events showing the cumulative rain considering the influence of the melting layer is given.

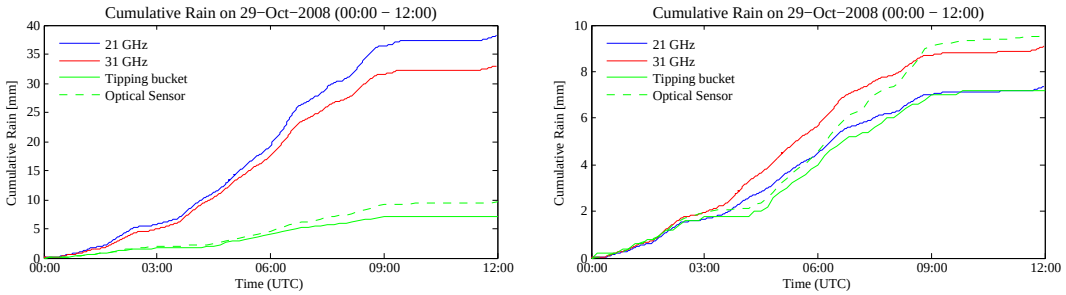

Figure 10.10: Cumulative rain with and without consideration of the melting layer. The rain estimation of TROWARA on October 29, 20087 are shown in blue (21 GHz) and red (31 GHz). The rain measurements at the ground are shown in green. Figure (a) shows the cumulative rain without consideration of the melting layer opacity and Figure (b) with use of the melting layer opacity.

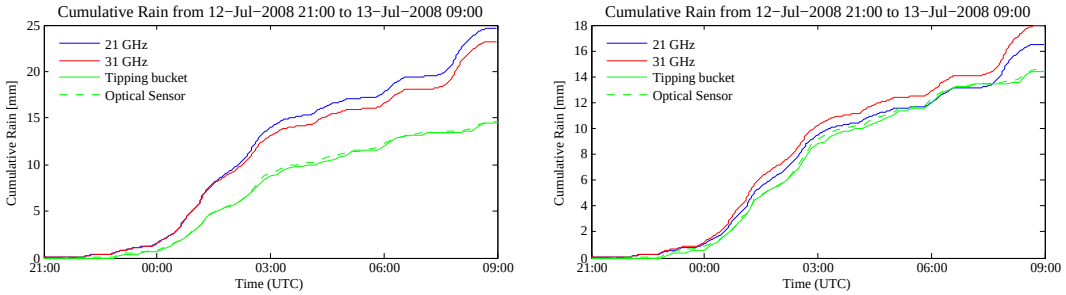

Figure 10.11: Another example of a rain event with and without consideration of the melting layer. The measurements are made on July 12, 2008. For the description see Figure 10.10.

10.7 The Opacity Ratio

Considering Equation (10.17), we can express the ratio between the two measured opacities as follows

$$\frac{\tau_{rain,31}}{\tau_{rain,21}} = \frac{g_{R,31}\, H_R + g_{ML,31}}{g_{R,21}\, H_R + g_{ML,21}} \tag{10.20}$$

If the depth of the rain layer (H_R) is small, the ratio is dominated by the ratio of the specific opacities $g_{ML,31}$ and $g_{ML,21}$. This ratio is about 1.4. On the other hand if the rain layer is thick, the ratio is dominated by the specific absorption coefficients $g_{ML,31}$ and $g_{R,21}$. This ratio is about 2.

If we plot the ratio of the measured opacities as function of the surface temperature, we expect that for temperatures around 2°C the ratio is about 1.4 and for higher temperature the ratio approaches 2, as a higher temperature is corresponding to a larger depth of the rain layer.

Figure 10.12 shows the ratio between the 31 and the 21 GHz melting layer opacity as a function of the surface temperature (for measurements on October 28, 2008). The expected signature cannot be seen. Further efforts have to be made to analyze such precipitation events.

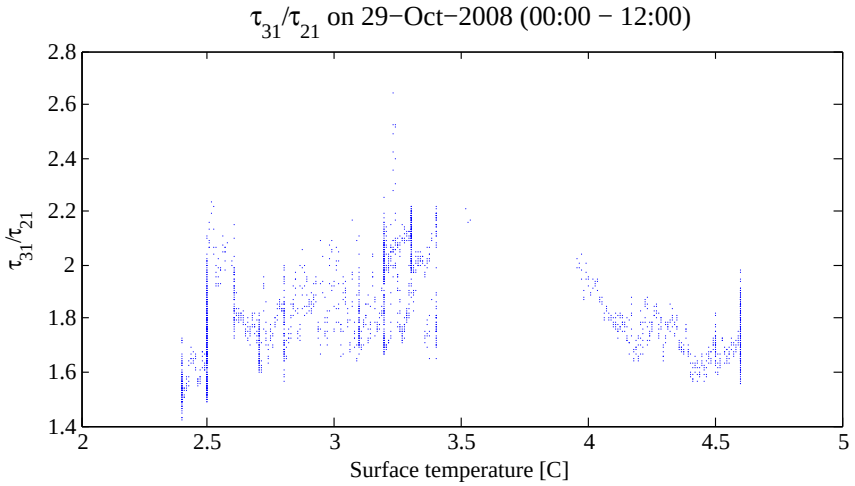

Figure 10.12: $\tau_{R,31}/\tau_{R,21}$ as function of the surface temperature.

10.8 Discussion

We presented a model to calculate the absorption coefficient within the melting layer. For precipitation events where the melting layer was located just above the ground, we compared the modeled opacity with measurements made by TROWARA.

The model is based on many assumptions. Some of them are caused by mathematical limits and others are based on physical considerations. But the degree of freedom is still high. Further studies about the melting layer can improve many assumptions.

The order of magnitude of the modeled opacity agrees with the measurements. Some disagreement can be explained.

The expansion of the TROWARA algorithm estimating the rain rain by the influence of the melting layer improves the results significantly.

The model is tested considering a few stratiform precipitation situations only. To get a better approvement of the model, it is necessary to test the model with more precipitation events.

Chapter 11

Conclusions and Outlook

In this work we focused on the estimation of precipitation by microwave sensors. For that purpose we used two instruments: a ground-based radiometer measuring the radiation at two frequencies (21 and 31 GHz) near the 22 GHz water vapor absorption line and a vertical pointing rain radar measuring at 24 GHz. A ground-based weather station helped to complete and to verify the measurement results.

The method of the rain radar to estimate rain is based on the radar reflectivity and the fall velocities of the rain drops. This method is well known and therefore we focus on the estimation of rain by the radiometer. The method of the radiometer is based on the emission of the rain drops in the microwave range.

The radiative properties of rain drops are understood well but lack in the estimation the emission of melting snow. The contribution of melting snow to the measured radiation cannot be neglected. Thus, a large part of this work deals with the properties of the region of the melting snow, the melting layer. Or from the radar perspective, the bright band.

The rain radar is an adequate instrument to analyze the melting layer; vertical profiles of the radar reflectivity and the fall velocity can be measured. But as strong vertical winds influence the radar measurements, weather situations with stratiform precipitation are analyzed only.

With use of the vertical profile measurements and theoretical considerations, a radiative model of the melting layer is developed. It is based on the dielectrical properties of wet snow. The shape of the melt water of a snow flake plays a key role in the model. As a result, the model is able to estimate the absorption coefficient of the melting snow and hence the opacity of the melting layer.

When the melting layer is just above the ground, it is possible to measure its opacity by the radiometer. Comparing the measured opacity with the model result, we can verify the accuracy of our melting layer model.

Although the model is restricted by mathematical limits (the Mie theory can handle spheres only) and the degree of freedom to tune the model is high, the modeled opacity of the melting layer corresponds well to the measurements.

Further it turns out that the opacity of the melting layer is proportional to the rain

rate. Using this important result we can improve the rain rate estimation algorithm of the radiometer.

To make the model more robust, it is necessary to verify its results by a large number of precipitation events. The cumulative rain estimated by the radiometer algorithm can be compared with measurements from ground-based rain sensors. Precipitation events, when the melting layer is just above the ground, can be used to determine the frequency dependence of the melting layer opacity. This information can help to adjust the shape factor of the liquid water of a snowflake.

A snowflake can be modeled in many different ways. An alternative to the described approach would be to consider the snowflake as a coated sphere with a low-density coating around a denser central part. This model can be used in Mie theory.

Other approaches to model the melting layer are described by F. Fabry (see [3]). The radiative properties of theses approaches could be calculated, and the results could be compared with the described model.

Bibliography

[1] Wiesmann A. and Mätzler C. Microwave emission model of layered snowpacks. *Remote Sensing of Environment*, 70:307–316, 1999.

[2] Eszter Barthazy. *Microphysical Properties of the Melting Layer*. PhD thesis, Swiss Federal Institute of Technologie (ETH), Zürich, Switzerland, 1998.

[3] F. Fabry and Szyrmer W. Modeling of the melting layer. Part II: Electromagnetic. *"J. Atmos. Sci."*, 56:3593–3600, 1999.

[4] F. Fabry and I. Zawadzki. Long-Term Radar Observations of the Melting Layer of Precipitation and Their Interpretation. *"J. Atmos. Sci."*, 52:838–851, 1994.

[5] F. Fabry and I. Zawadzki. Atmospheric Physics as Observed by a Vertically Pointing Doppler RADAR. In *Proceedings, 13th International Conference on Clouds and Precipitation*, pages 310–313, Reno NV, 2000.

[6] Niklaus Kämpfer. *Physik der Atmosphäre*, 2007. Manuscript of the Lecture Course *Introduction to Climate and Environmental Physics*, Fall Semester 2007, University of Bern.

[7] Christian Mätzler. Drop-Size Distributions and Mie Computations for Rain. IAP Research Report 2002-16, Institut für angewandte Physik, Universität Bern, Bern, Switzerland, November 2002.

[8] Christian Mätzler. Effects of Rain on Propagation, Absorption and Scattering of Microwave Radiation Based on the Dielectric Model of Liebe. IAP Research Report 2002-10, Institut für angewandte Physik, Universität Bern, Bern, Switzerland, December 2002.

[9] Christian Mätzler. MATLAB Functions for Mie Scattering and Absorption. IAP Research Report 2002-08, Institut für angewandte Physik, Universität Bern, Bern, Switzerland, June 2002.

[10] Christian Mätzler. MATLAB Functions for Mie Scattering and Absorption, Version 2. IAP Research Report 2002-11, Institut für angewandte Physik, Universität Bern, Bern, Switzerland, December 2002.

[11] Christian Mätzler. *Radarmeteorologie*, 2003. Vorlesung Sommersemester 2003, Universität Bern.

[12] Christian Mätzler. *Thermal Microwave Radiation: Applications for Remote Sensing.* Number 52 in IEE Electromagnetic Wave series. The Institution of Engineering and Technology (IET), 2006.

[13] Christian Mätzler. *Physical Principles of Remote Sensing*, 2007. Manuscript of the Lecture Course, Spring Semester 2007, University of Bern.

[14] Christian Mätzler and June Morland. Advances in Surface-Based Radiometry of Atmospheric Water. IAP Research Report 2008-02-MW, Institut für angewandte Physik, Universität Bern, Bern, Switzerland, February 2008.

[15] METEK. *MRR - Physical Basics*, 2005. Version 1.9.0.

[16] METEK. *MRR-2 - User Manual*, 2005. Version 4.01/4.10.

[17] J. Morland, B. Deuber, D. G. Feist, L. Martin, S. Nyeki, N. Kämpfer, C. Mätzler, P. Jeannet, and L. Vuilleumier. The STARTWAVE atmospheric water vapour database. *Atmospheric Chemistry and Physics*, 6:2039–2056, 2006.

[18] June Morland. TROWARA - Tropospheric Water Vapour Radiometer. Radiometer review and new calibration model. IAP Research Report 2002-15, Institut für angewandte Physik, Universität Bern, Bern, Switzerland, November 2002.

[19] R. Peter and N. Kämpfer. Radiometric determination of water vapor and liquid water and its validation with other techniques. *J. Geophysical Research*, 97:18,173–18,183, 1992.

[20] Hans R. Pruppacher and James D. Klett. *Microphysics of Clouds and Precipitation.* Kluwer Academic Publishers, Dordrecht, The Netherlands, 1997.

[21] Robert A. Houze. *Cloud Dynamics.* Academic Press, San Diego, CA, 1993.

[22] Walter Roedel. *Physik unserer Umwelt: Die Atmosphäre.* Springer-Verlag, 3^{rd} edition, 2000.

[23] R. R. Rogers and M. K. Yau. *A Short Course in Cloud Physics.* Butterworth-Heinemann, 3^{rd} edition, 1989.

[24] Henri Sauvageot. *Radar Meteorology.* Artech House, Boston, MA, 1992.

[25] John H. Seinfeld and Spyros N. Pandis. *Atmospheric Chemisty and Physics: From Air Pollution to Climate Change.* John Wiley and Sons, Inc., 2^{nd} edition, 2006.

[26] Arthur von Hippel. *Dielecrics and Waves.* Artech House, 1^{st} edition, 1954.

Appendix A

Setup of the Micro Rain Radar

In this appendix we describe the setup and the storage of the data of the Micro Rain Radar. First, we give an overview over the physical setup of the equipment. A more detailed description is given in the manual of the manufacturer (see [16]). Secondly, we describe the process converting and storing the measured data in the MySQL database. At last, the structure of the MySQL database, where the data is stored, is explained.

A.1 Setup

An overview of the physical setup of the MRR instrument is shown in Figure A.1. On the left side, we see the radar antenna with the radar module. The MRR is located on the roof of the ExWi building. The radar signal is processed in the radar module and averaging is done there. Every 10 seconds, the raw data are transmitted to the connection box. This box is located inside the ExWi building. The connection box forwards the raw data over a serial connection cable to a converter, where the data are transmitted over the IAP network to the MRR PC.

The MRR PC receives the raw samples and stores them on its hard disc. Additionally, the raw data are processed to second level products as the radar reflectivity, the fall velocity, etc. These processed data are stored on the hard disc of the MRR PC as well.

At about 2:00 at night, the data of the previous day are read from the MRR PC and are inserted into the MySQL database of the IAP microwave institute. Only periods are stored, where precipitation is detected at any height level.

A.2 Data Storage

A.2.1 Copy the Data from the MRR-PC

The processing of the radar signals to the raw data and the processing of the raw data to higher level products is well documented in the manual of the radar ([16]).

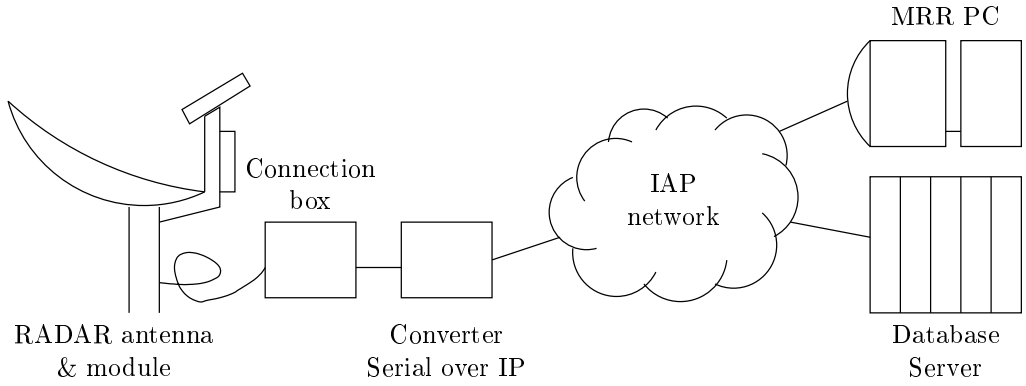

Figure A.1: Setup of the radar equipment.

All data are stored on the MRR PC by the software of the manufacturer. Here we describe the process transferring the data from the MRR PC to the MySQL database.

The data of the previous day is moved from the MRR PC to the MySQL database every night at 2:00. Responsible for this action is the pseudo-user `mrruser`. On the server `juno`, a script owned by and executed with the permissions of the `mrruser` is executed every night (a so called *cron*-job). It copies the data from the MRR-PC to the home directory of the `mrruser` (`/home/mrruser`). This script is written in the language *perl*. The source code is stored at `/home/mrruser/perl/mrr_save.pl`.

The directory structure stays the same as on the MRR-PC. The instantaneous, the averaged and the raw data are stored in three main directories, as listed below

`~/mrr/metek/Instdata`	Instantaneous data
`~/mrr/metek/Data`	Averaged data
`~/mrr/metek/Rawdata`	Raw data

The directory structure is the same in each of this three directories. The sub-directories are named according to the year and month of the stored data. Each data-file contains the data of one day and is named after the month and the day of stored data. For example, the instantaneous data of the January 14, 2009 stored in `~/mrr/metek/Instdata/200901/0114.MRR`.

Note, that all data are compressed in the `mrruser` home directory and all files have the additional extension `.gz`.

If the data are successfully copied they are removed on the MRR-PC.

A.2.2 Insert the Data to the MySQL Database

The *perl*-script `/home/mrruser/perl/mrr_add2mysql.pl` extracts the values from the day files and inserts then into the MySQL data base. The format of the day files is described in [16]. It is different for instantaneous, averaged and raw data.

The structure of the MRR database is described in the next section.

A.3 Structure of the Database

The database on the MySQL server is called `MRR`. It contains three tables `data`, `avgdata` and `rawdata`, where `data` contains the instantaneous, `avgdata` the averaged and `rawdata` the raw data.

Every data sample is specified by the time and the location. The column name for the time specification is `datetime` and the one dimensional specification for the location is the `height`. The `datetime` is given in UTC and the `height` is the height in m above the MRR.

Example: Here an example is shown to read all values of the radar reflectivity (`Z`) from the instantaneous table (`data`) at height 100 m in the time interval from March 3, 2009 12:00 and 12:10.

```
mysql> SELECT Z FROM data WHERE height=100 AND datetime BETWEEN
       '2009-03-05 12:00' AND '2009-03-05 12:10';
```

The columns in each of the three table correspond to a parameter measured by the MRR (except the time (`datetime`) and the height (`height`), we already discussed).

The following parameters are stored in the tables `data` and `avgdata`:

`Z`	Radar reflectivity (in dBZ)
`W`	Fall velocity (in m/s)
`RR`	Rain rate (in mm/h)
`LWC`	Liquid water content (in g/m3)
`Fnn`	Spectral reflectivity (in dB where $(0 \leq nn \leq 63)$
`Nnn`	Number of drops per volume and drop size (where $4 \leq nn \leq 49$)

Appendix B

MATLAB Functions

In this appendix a short summary of the most important MATLAB functions is given. Four tables are listed. The first table lists the MATLAB functions used to analyze the data from the MRR. The second table lists the functions to analyze the TROWARA data. The third table summarizes the functions used for the radiative model of the melting layer. And the fourth table lists additional help functions. Most of them can be used to read data from the databases.

Note, that just a short description is given for each function. For more details about the usage of the functions, type `help <functionname>` at the MATLAB prompt. Most of the functions include a help text, explaining the functionality of the parameters.

Table B.1: MRR MATLAB functions. A list of functions used to visualize and analyze the MRR data.

MATLAB Functions
mrrreflectivity *mrrreflectivity(year,month,day,[hour,minute,duration])* Make a time-height colorplot of the radar reflectivity for the selected time period. Reflectivity values below 5 dBZ and above 40 dBZ are clipped.
mrrfallspeed *mrrfallspeed(year,month,day,[hour,minute,duration])* Make a time-height colorplot of the fall speed for the selected time period. Values below 0 m/s and above 20 m/s are clipped.
mrrhydrometeors *mrrhydrometeors(year,month,day,[hour,minute,duration])* Make a colorplot of the different types of hydrometeors for the selected time period. From the MRR database the radar reflectivity and the fall speed is read. According to the combination of reflectivity and fall speed, the region is quantified as rain, snow or drizzle.
Continued on next page

Table B.1 – continued from previous page
mrrrainrate *mrrrainrate(year,month,day,[hour,minute,duration])* Make a time-height colorplot of the radar rain rate for the selected time period. Values below 0 mm/h and above 30 mm/h are clipped.
mrrlwc *mrrlwc(year,month,day,[hour,minute,duration])* Make a time-height colorplot of the liquid water content (LWC) for the selected time period. Values below 0 g/m^3 and above 10 g/m^3 are clipped.
mrrbbh *mrrbbh(year,month,day,[hour,minute,duration])* Plot the brightband height within a given time period.
mrrselect *mrrselect(year,month,day,[hour,minute,duration])* Plot the cumulative rain measured by the MRR together with rain measurements from the ground.
mrrprofile *mrrbbh(year,month,day,[hour,minute,duration,average])* Plot vertical profiles of the radar reflectivity and the fall velocity at a given time. If average=1, plot the averaged profile only.
mlanalyze *mlanalyze(year,month,day,[hour,minute,duration])* Analyze ML within a given time period (just use for short time intervals in the order of 15 minutes). The sample profiles of the fall velocity and the radar reflectivity are approximated by a model profile. This model profile is determined in two steps. A first approximation by a cross-correlation method. And then the fine tuning is made with a time-consuming brute-force method. As result, this 'mlanalyze' return the parameters of the model profile.

Table B.2: TROWARA functions. A list of functions used to process the TROWARA data.

MATLAB Functions
trowaraIWV *trowaraIWV(year,month,day,[hour,minute,duration])* Analyze water vapor, cloud liquid water, rain and snow within a given time period. This function uses radiometer data from TROWARA (21, 22 and 31 GHz), ground-based measurement from the Exwi meteostation and data from the vertical pointing rain radar (MRR) located at the roof of the Exwi building.

Table B.3: Radiative model of the melting layer. A list of functions used to calculate the melting layer absorption coefficient and the opacity.

MATLAB Functions
snowplot *snowplot* Main function of radiative model of the melting layer. Using the dielectric constants of dry and wet snow, the absorption coefficient is calculated as a function of the height in the melting layer.
epsdrysnow *eps = epsdrysnow(rho, fGHz, TK)* Dielectric constant of dry snow.
epswetsnow *eps = epswetsnow(w, A1, rho, fGHz, TK)* Dielectric constant of wet snow.
getFallVelocity *v=getFallVelocity(h,H,vsnow,vrain)* Get the characteristic of fall velocity in the melting layer. H is the depth of the melting layer and h is position in the melting layer.
getVolumeFraction *fv=getVolumeFraction(h,H)* Get characteristic of volume fraction. The volume fraction is the ratio between the volume of water (liquid and frozen) to the total volume of a snow flake. H is the depth of the melting layer and h is position in the melting layer.
getLiquidWaterFraction *w=getLiquidWaterFraction(h,H)* Get the liquid water fraction in the melting layer. The liquid water fraction is the ratio between the amount of liquid water to the total amount of water (liquid and ice). H is the depth of the melting layer and h is position in the melting layer.

Table B.4: Database access functions. List of MATLAB functions used to get data from the MYSQL data bases.

MATLAB Functions
getExwiMeteoData *result=getExwiMeteoData(year,month,day,hour,minute,duration,params)* Get data from the ExWi meteo station. Select the time, the duration and one or more parameters. Possible parameters are: temperature, rel_humidity, pressure, wind_speed, wind_dirn, max_gust, visibility, global_rad, precipitation, rain_sensor, weather_code.
Continued on next page

Table B.4 – continued from previous page
getBollwerkMeteoData *result=getBollwerkMeteoData(year,month,day,hour,minute,duration,params)* Get data from the Bollwerk meteo station. Select the time, the duration and one or more parameters. Possible parameters are: wind_speed, wind_dirn, max_gust, temperature, grass_temp_5cm, rel_humidity, pressure, precipitation, distant_lightning, near_lightning, global_rad, sky_brightness, sunshine_duration, sky_brightness_avg, net_radiation.
getZimmerwaldMeteoData *result=getZimmerwaldMeteoData(year,month,day,hour,minute,duration,params)* Get data from the Zimmerwald meteo station. Select the time, the duration and one or more parameters. Possible parameters are: temperature, rel_humidity, pressure, wind_speed, wind_dirn, max_gust, visibility, global_rad, precipitation, rain_sensor.
getRadiosondeData *result=getRadiosondeData(year,month,day,hour,minute,duration,station,params,h)* Get data from the radiosondes. Select the time, the duration, the parameters and the height range. Possible stations are: Payerne, Thun, Nancy, Lyon, Stuttgart, Muenchen, Innsbruck, Udine, Milano, S. Pietro Capofiume. Possible parameters are: stationid, pressure, temperature, dew_point, wind_dirn, wind_speed, rel_humidity, height
getMRRData *result=getMRRData(year,month,day,hour,minute,duration,param,levels)* Get data from the MRR database. Select the time, the duration, the parameter and the height levels. Possible parameters are: TF, Z, RR, W, LWC, Fnn, Nnn.
getTROWARAData *result=getTROWARAData(year,month,day,hour,minute,duration,params)* Get data from the TROWARA database. Select the time, the duration and one or more parameters. Possible parameters are: lev1bt21, lev1bt22, lev1bt31, irbt, iwv_newfit, ilw_newfit, iwv_newfit_22, ilw_newfit_22, iwv_wu, ilw_wu
radiosonde *radiosonde(year, month, day, lanch, [hmin, hmax], [tmin, tmax])* Plot radiosonde temperature and dew point profile of a radiosonde launched in Payerne.

Appendix C

The Observed Time Series

In this chapter, we give some additional information about the observed time series. First, we give some general information about the time series and the settings of the MRR. Then a table with long precipitation periods is given. Another table with precipitation events showing a characteristic melting layer profile is listed at the end.

C.1 General Information

The duration of the investigated time series was mainly determined by the Micro Rain Radar. The MRR was setup in spring 2007. Thus, there are data available between March and June 2007. This data are not synchronized to UTC time and there are some data leaks. Thus, we did not use the data in this time period for our studies.

In June 2007, the hard-disc of the MRR measurement computer was completely full. The MRR could not store more data. Thus, no MRR data are available between June and September 2007.

The automated processing of the data and the synchronization with UTC time was done in September 2007. The considered time series started on September 24, 2007. We analyzed the measurement data until the end of March 2009. During this time period, data were lost twice. The Ethernet switch connecting the MRR with the measurement computer failed on August 13, 2008. The MRR software of the MRR PC processing the MRR raw data, terminated for unknown reason on November 13, 2008. Thus, we lost the data of two days within the observed time series.

The height resolution of the MRR was set to 100 m of the beginning and was changed to 50 m on November 19, 2008.

Figure C.1 shows the number of precipitation days within the observed time series. Within the observed time series of 555 days, the tipping rain sensor detected 235 days with cumulative precipitation larger than 0.1 mm (in 2008 159 precipitation days are found). Using the MRR, we find 262 days of precipitation within the same time period.

Figure C.2 shows the monthly precipitation measured by the tipping rain sensor on top of the ExWi building. The red curve shows the monthly precipitation measured at the MeteoSwiss weather station in Zollikofen and averaged over the 30 years period

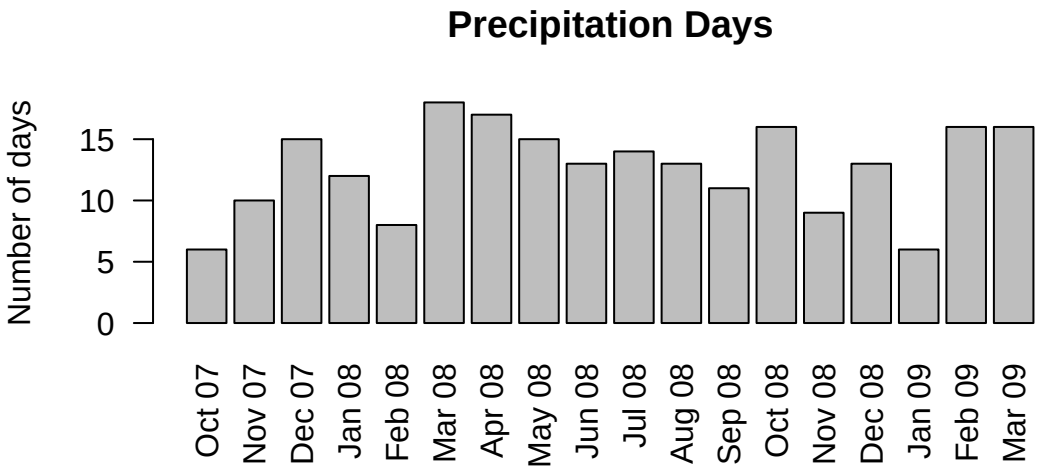

Figure C.1: Number of precipitation days per month.

from 1971 to 2000.

In total we measured 1260 mm of precipitation by the tipping rain sensor, 905 mm in the year 2008. The total 30 year averaged precipitation of the Zollikofen weather station is 1043 mm. Thus, there was a little less precipitation in the year 2008 as for the averaged reference time period.

C.2 Long Precipitation Periods

Table C.1 gives a list with the longest precipitation periods within the observed time period.

Table C.1: Long precipitation periods. Sorted by duration. The column *interrupts* indicates how many times the precipitation period was interrupted by a non-raining period shorter than 5 minutes.

Start Date & Time	**Duration [min]**	**Interrupts**
2009-03-04 22:30	2954	5
2008-04-21 07:23	1766	4
2009-02-07 14:34	1498	10
2009-03-28 07:06	1440	0
2009-02-17 01:59	1314	6

Continued on next page

Table C.1 – continued from previous page

Start Date & Time	Duration [min]	Interrupts
2008-10-28 07:09	1213	3
2008-03-20 23:47	1145	14
2009-01-19 09:25	1046	1
2008-01-05 11:30	1032	0
2008-04-28 09:49	991	0
2008-12-09 16:55	959	2
2008-10-29 14:59	909	2
2007-11-23 10:50	821	2
2008-01-12 00:43	802	5
2009-02-06 22:35	777	1
2009-03-02 04:17	751	1
2008-07-13 18:53	747	0
2008-09-06 10:33	738	3
2009-03-02 17:40	698	14
2008-01-15 23:22	671	0
2008-07-12 22:05	670	1
2008-06-15 20:07	658	0
2008-12-10 15:32	647	10
2008-12-31 11:06	630	1
2007-10-30 05:53	627	1
2008-09-13 03:06	620	0
2008-04-10 04:17	618	1
2008-11-21 05:03	599	3
2008-12-17 00:24	587	3
2008-03-17 11:42	585	14

C.3 Events with Characteristic ML Profile

To analyze the characteristics of the melting layer, we have chosen events where the precipitation was stable and the profiles of the radar reflectivity and the fall velocity show the expected shape. The duration of all these events is 15 minutes. The table below shows the date and time of the selected events.

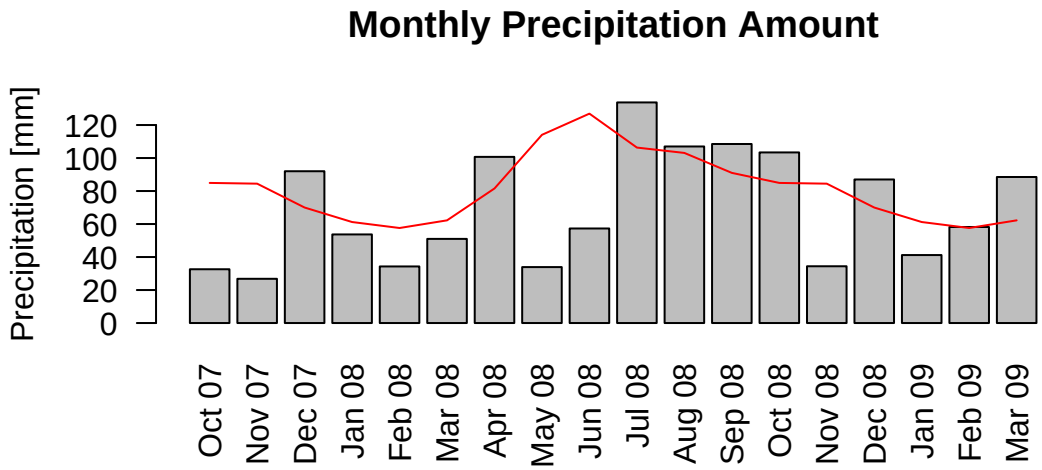

Figure C.2: Monthly precipitation. Precipitation measurements taken from the ExWi weather station. The red curve shows the 30 year mean values.

Table C.2: Precipitation events with a characteristic melting layer profile. within 15 minutes. The starting time of the 15 minutes period is given.

Date & Time	Date & Time	Date & Time
2007-09-26 22:00	2007-09-28 16:45	2007-09-29 22:15
2007-11-22 21:30	2007-11-23 13:00	2007-12-01 12:45
2007-12-02 19:00	2007-12-10 16:00	2008-01-05 20:00
2008-01-06 03:15	2008-01-07 05:15	2008-01-16 06:15
2008-01-24 23:30	2008-02-26 19:15	2008-03-15 23:30
2008-04-09 12:15	2008-04-10 05:00	2008-04-19 06:15
2008-04-21 12:00	2008-04-22 07:00	2008-04-28 14:00
2008-04-29 01:00	2008-06-04 09:00	2008-06-06 08:00
2008-06-07 07:00	2008-06-12 20:45	2008-06-15 19:00
2008-06-16 05:00	2008-07-13 07:00	2008-07-14 04:45
2008-09-04 08:15	2008-09-05 00:15	2008-09-06 19:45
2008-09-13 12:00	2008-09-13 18:00	2008-09-14 03:30
2008-10-16 09:30	2008-10-22 12:00	2008-10-28 01:15
2008-10-28 05:00	2008-10-28 14:00	2008-11-11 16:00
2008-11-12 03:15	2008-11-21 11:30	2008-12-04 20:45
2008-12-05 21:45	2008-12-06 10:00	2008-12-19 11:50
2008-12-31 11:45	2009-01-18 12:30	2009-01-19 21:00

Continued on next page

Table C.2 – continued from previous page

Date & Time	Date & Time	Date & Time
2009-01-20 00:45	2009-01-23 07:00	2009-02-06 23:00
2009-02-07 00:45	2009-02-09 20:00	2009-02-10 07:30
2009-03-01 21:00	2009-03-02 05:15	2009-03-02 06:15
2009-03-02 08:00	2009-03-02 09:30	2009-03-02 10:15
2009-03-02 11:30	2009-03-02 13:00	2009-03-02 13:30
2009-03-02 14:45	2009-03-02 15:45	2009-03-02 16:30
2009-03-02 18:00	2009-03-02 18:30	2009-03-02 19:30
2009-03-02 20:30	2009-03-02 21:30	2009-03-02 22:30
2009-03-03 03:15	2009-03-04 23:00	2009-03-05 00:15
2009-03-08 18:45	2009-03-10 18:15	2009-03-11 02:00
2009-03-25 19:00	2009-03-26 19:00	2009-03-27 03:00
2009-03-28 09:45	2009-03-28 12:15	2009-03-28 15:30

Appendix D

Cumulative Precipitation Examples

In this chapter, a collection of selected precipitation events is shown. For each precipitation event, the cumulative precipitation considering the influence of the melting layer is calculated.

With help of the MRR, the height of the 0°C temperature is determined. Together with the surface temperature, the lapserate Γ is calculated.

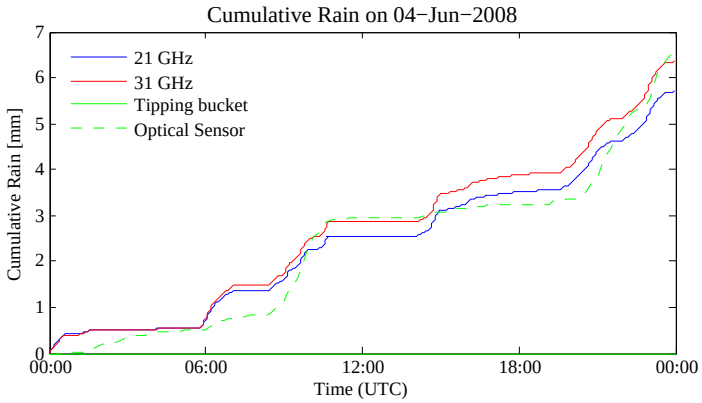

Figure D.1: Cumulative precipitation on June 4, 2008 ($\Gamma = 6$ K/km, $ILW_R = 0.4$ mm) (Tipping-bucket sensor out of order).

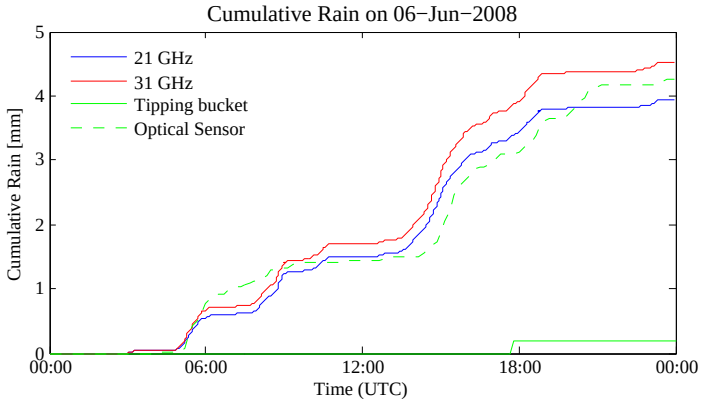

Figure D.2: Cumulative precipitation on June 6, 2008 ($\Gamma = 5.5$ K/km, $ILW_R = 0.35$ mm) (Tipping-bucket sensor out of order).

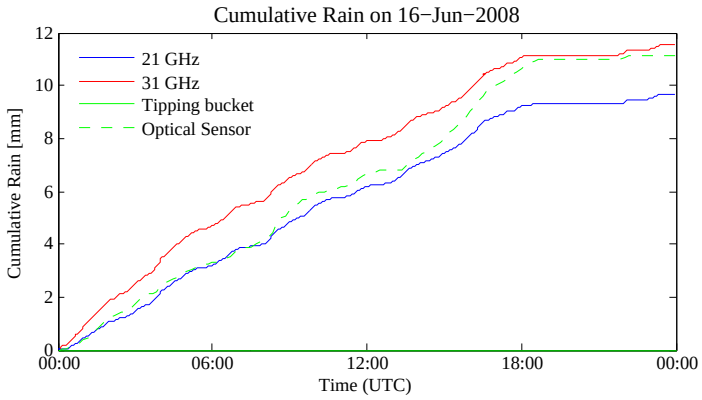

Figure D.3: Cumulative precipitation on June 16, 2008 ($\Gamma = 6$ K/km, $ILW_R = 0.2$ mm) (Tipping-bucket sensor out of order).

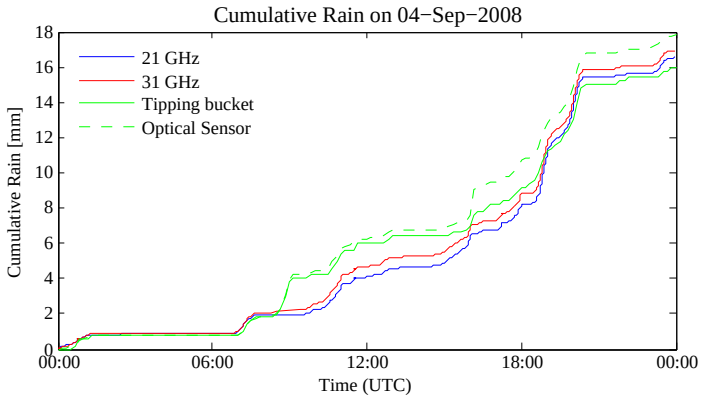

Figure D.4: Cumulative precipitation on September 4, 2008 ($\Gamma = 5.8$ K/km, $ILW_R = 0.2$ mm).

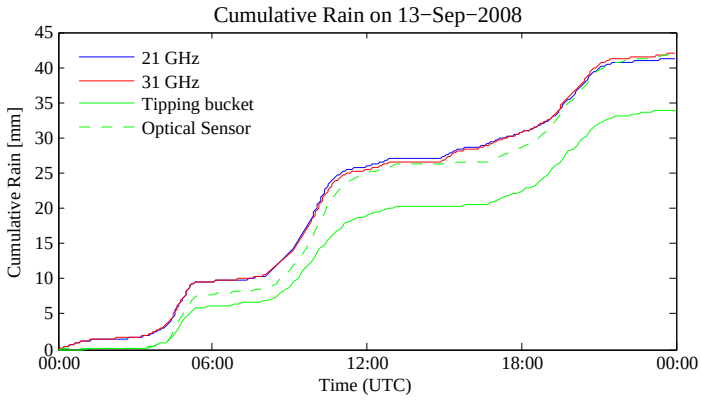

Figure D.5: Cumulative precipitation on September 13, 2008 ($\Gamma = 6$ K/km, $ILW_R = 0.25$ mm).

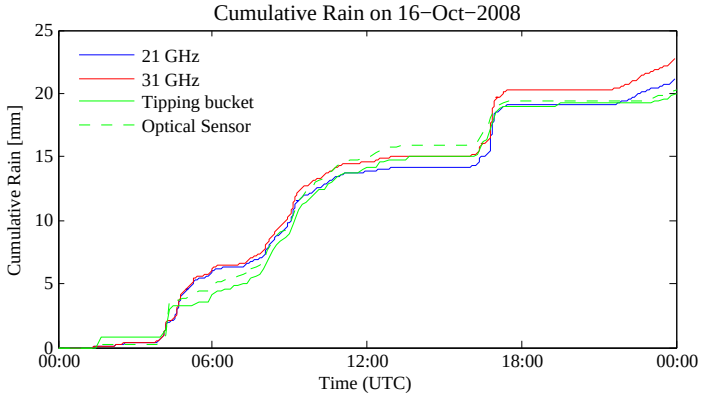

Figure D.6: Cumulative precipitation on October 16, 2008 ($\Gamma = 6.5$ K/km, $ILW_R = 0.3$ mm).

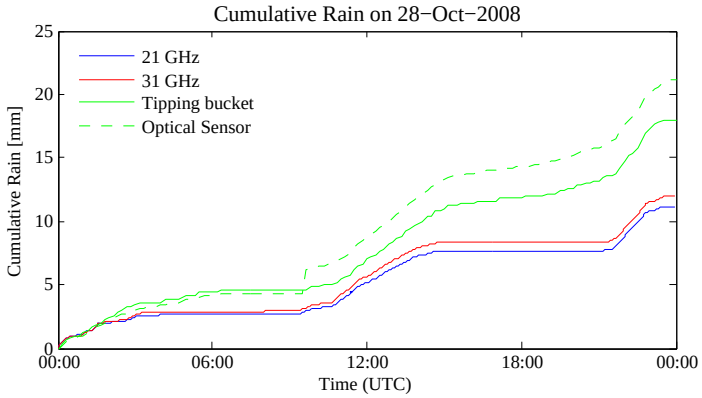

Figure D.7: Cumulative precipitation on October 28, 2008 ($\Gamma = 7$ K/km, $ILW_R = 0.2$ mm).

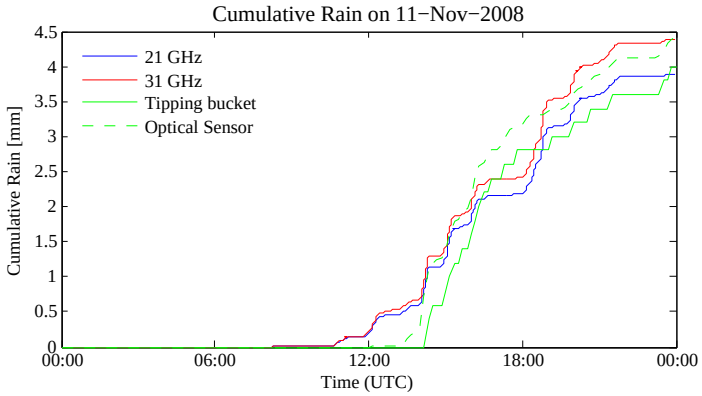

Figure D.8: Cumulative precipitation on November 11, 2008 ($\Gamma = 7$ K/km, $ILW_R = 0.2$ mm).

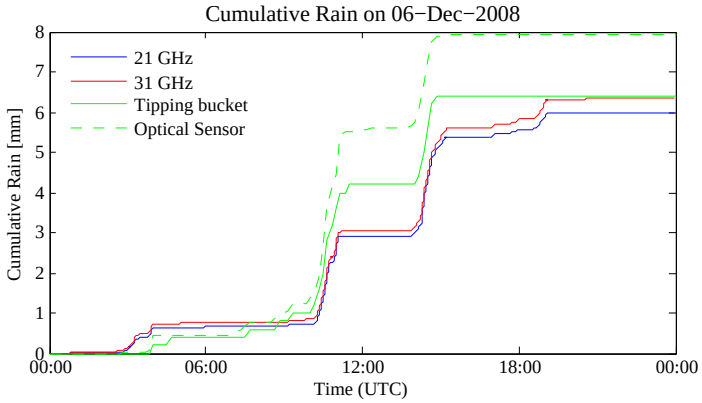

Figure D.9: Cumulative precipitation on December 6, 2008 ($\Gamma = 8$ K/km, $ILW_R = 0.15$ mm).

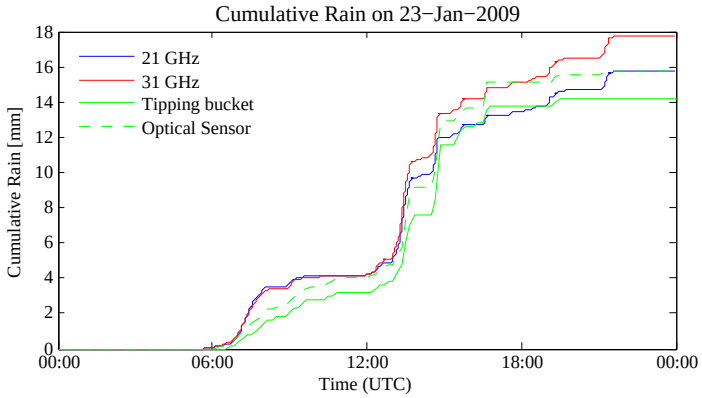

Figure D.10: Cumulative precipitation on January 23, 2009 ($\Gamma = 6$ K/km, $ILW_R = 0.3$ mm).

Acknowledgement

I am appreciative to the following people who made this work possible:

- Christian Mätzler for supervising my work and for having always time to answer my questions.
- Niklaus Kämpfer for giving my the opportunity of joining the Institute of Applied Physics.
- Eddy Graham for being my room mate and sharing his enthusiasm about clouds and weather phenomena.
- Stefan Müller and Lorenz Martin for the introduction to the system administration and the good collaboration.
- All the colleagues of the microwave department for the good colleagueship.
- Jürg Stettbacher for giving me the opportunity to work occasionally. My studies would not have been possible without this side job.
- My friends for distracting me from work.
- Sonja for her interest in my work and me.

Erklärung

gemäss Art. 28 Abs. 2 RSL 05

Name/Vorname:	Leuenberger Andreas
Matrikelnummer:	92-903-756
Studiengang:	Climate Sciences Bachelor ☐ Master ☒ Dissertation ☐
Titel der Arbeit:	Precipitation Measurements with Microwave Sensors
Leiter der Arbeit:	Prof. Dr. Christian Mätzler

Ich erkläre hiermit, dass ich diese Arbeit selbständig verfasst und keine anderen als die angegebenen Quellen benutzt habe. Alle Stellen, die wörtlich oder sinngemäss aus Quellen entnommen wurden, habe ich als solche gekennzeichnet. Mir ist bekannt, dass andernfalls der Senat gemäss Artikel 36 Absatz 1 Buchstabe o des Gesetzes vom 5. September 1996 über die Universität zum Entzug des auf Grund dieser Arbeit verliehenen Titels berechtigt ist.

Bern, den 26. Mai 2009

Unterschrift